In Situ Raman Spectroscopy of the Type Selective Etching of Carbon Nanotubes and their Growth from C_{60} Seeds

Andrew Li-Pook-Than

Thesis submitted to the
Faculty of Graduate and Postdoctoral Studies
In partial fulfillment of the requirements for the degree of
Doctor of Philosophy in Physics

Department of Physics
Faculty of Science
University of Ottawa

ABSTRACT

In situ Raman spectroscopy was used to explore etching of carbon nanotubes as well as their growth from C_{60}. The thesis is in three parts: (1) C_{60} seed particles were partially oxidized in air and were used to grow carbon nanotubes and other nanocarbon structures. Seed oxidization was characterized by monitoring the evolution of the Raman $A_g(2)$ peak and the D band, and oxidation temperature was found to be critical to nanotube growth. (2) To further explore oxidation, carbon nanotubes were thermally oxidized in air at different temperatures, while the evolution of different Raman bands was tracked. Etching dynamics and band intensity evolution were tracked *in situ*. Notably, metallic species were found to etch much more rapidly than semiconducting species of similar diameter. (3) To confirm and expand on this, a novel, simultaneous two-laser Raman spectroscopy setup was used to track the thermal oxidation of carbon nanotubes in O_2 and CO_2 gases at different temperatures. Metallic species were resonant with one laser line, while semiconducting species were resonant with the other, so changes to sample metallicity could be tracked unambiguously in two separate spectra. Again, metals were found to etch more rapidly. *In situ* Raman spectroscopy can track the evolution of nanotubes in real time and provide insight into processing. In general, detailed process monitoring like this can help in the development of selective synthesis and processing.

STATEMENT OF ORIGINALITY AND COLLABORATIONS:

The author (Andrew Li-Pook-Than) declares that this thesis constitutes original research and that I have used no other sources except as noted by citations.

- All experimental work and analysis was carried out by the author.
- Work and analysis were performed under the supervision of Paul Finnie of the Security and Disruptive Technologies Research Portfolio formerly the Institute for Microstructural Studies, National Research Council in Ottawa.
- Almost all the data was obtained by the author except:
    - Photoluminescence images for Chapter 2 were taken by Paul Finnie, as were *ex situ* multi-wavelength Raman spectra in Chapters 3 and 4
    - In Chapter 3, TEM data was provided by Xiaohua Wu, HRTEM data was provided by Martin Couillard, and XPS data was provided by Oltion Kodra
- Also in Chapter 3, substrates were prepared by Hue Tran. The author is grateful for assistance for sample growth given by Phillip Vinten. The author also benefited from the development of equipment and processes by Paul Finnie, Paul Marshall, Kate Kaminska, and Jeffery Bond.

ACKNOWLEDGEMENTS

Special thanks to my supervisor Paul Finnie and to all collaborators and co-authors in this work, in particular Paul Marshall, Jacques Lefebvre, and Phillip Vinten. I am grateful for financial support from the University of Ottawa, Natural Sciences and Engineering Research Council of Canada (NSERC) and a grant from Le Fonds de Recherche du Québéc_Nature et Technologies (FRQNT). Thanks to the National Research Council of Canada (NRC) for hosting me and to the thesis committee for their time. Additional thanks to family and friends for their support.

TABLE OF CONTENTS

LIST OF FIGURES

Chapter 1

Chapter 2

Chapter 3

Chapter 4

1. INTRODUCTION

1.1 Motivation

Carbon nanotubes (CNTs) are quasi-one dimensional nanostructures that have been the subject of intense research over the past two decades.[1,2] They are allotropes of carbon that take the form of nanometer-wide cylinders with one or more concentric layers. Originating from their sp^2-hybridized bonds and the large disparity between their width-to-length ratios, they exhibit extreme physical properties including, but not limited to, high electric current capacities and carrier mobilities, high thermal conductivities, and high tensile strengths and stiffnesses.[3-8] Conceptually, they can be thought of as rolled up 2D sheets of graphene, another heavily-researched nanocarbon, which are closed either at one or both ends with a half-fullerene cap. CNT structures are defined by how tightly and at what angle these sheets are rolled (i.e. their "chirality"), with the resulting pristine CNTs being either metallic or direct band gap semiconductors with variable band gaps sizes.[3]

Therefore, CNTs have been studied for a wide variety of material applications, whether they are separated individually or used in bulk.[8,9] Some of these more heavily researched usages include flexible electronics, transparent and conductive films, supercapacitors, conductive wires, field emission displays, thermoacoustic devices, high strength composite materials, actuators, blackbody absorption, dry adhesion, energy storage, chemical sensors, and scanning probe tips.[8-11] Furthermore, pristine CNTs may be doped, chemically functionalized, or "unzipped" to form graphene sheets. In all these roles, chirality has a direct impact on how the CNTs behave.

Over time, CNT material costs have gradually decreased as different high yield growth methods have been developed, but as of yet, facile, commercially viable, chirality-specific CNT growth has not yet been fully achieved.[12-14] Currently, post-growth, solution based CNT separation techniques have been particularly successful as a means of separating metallic and semiconducting CNTs, but these techniques require multiple processing steps and can introduce impurities in to the final product.[9,15-17] Therefore, there is considerable interest in studying chirality-selective CNT growth and

destruction reactions. The kinetics and basic mechanisms involved in such reactions are generally still not fully understood, but might be monitored by analytical tools in order to determine the cause of their selectivity.

In particular, the role of oxygen in different nanocarbon growth and destruction reactions is also an important topic that is a central theme in this work. The presence of various oxygen chemical species, for example, is essential in certain synthesis processes that produce high yields of CNTs, and is known to play a role in both the removal of defects in graphitic materials, and different types of doping.[18-21] Furthermore, metallic CNTs in transistor-like devices can be resistively heated and preferentially burned away in atmosphere.[22-24] It follows that it is important to control and analyze the presence of air and water vapor when dealing with nanocarbon chemistry. A miniature CVD reactor system was adapted so that the gas phase oxidation of different nanocarbons in air, O_2, and CO_2 can be reliably performed while being monitored *in situ*.

In situ Raman spectroscopy, a powerful optical characterization technique, is the primary characterization method that we use to directly track nucleation and oxidation reactions as they occur. In Raman spectroscopy, essentially, when incoming laser light is directed at a material with distinct vibrational states, most photons are scattered elastically, but a small fraction will interact and scatter from these states at shifted frequencies. If these scattered photons are collected and analyzed, they produce a unique spectrum that identifies the material and by the chemical bonds the frequencies represent. Furthermore, different peaks within this spectrum will be enhanced if the laser frequency is resonant with different electronic states within the material system. In the case of nanotubes, CNTs of different chiralities, diameters, metallicity, and defect levels will produce distinct Raman spectra. [25-29] By monitoring materials *in situ* and tracking changes to spectra as they evolve we get direct information about changes in the populations of CNTs and other nanocarbons.[30-34]

This thesis reports three separate, but related studies.

In our first study (Chapter 2), we analyze the nucleation and growth of CNTs from C_{60} "seed" molecules within a chemical vapor deposition (CVD) reactor. This is a potential technique for chirality and type specific synthesis. It differs from the more established CVD synthesis of CNTs using catalytic nanoparticles, which often consist of

metals or metal oxides, encompasses a well-established family of techniques. However, the resultant grown CNTs are typically a mixture of metallic and semiconducting CNTs, with a range of different diameters. By instead using partially air-oxidized, fullerene molecules of uniform diameter as catalyst particles, we expect grown CNTs to be more structurally similar to each other and to fall in to a smaller set of chiralities. Cloning of seed particles has long been a part of nanotube synthesis work. Our work on C_{60} seeds was stimulated by progress in this area reported in 2010.[35] In short, better control over seed particles should lead to better chirality control.

Consistent with Yu *et al*.,[35] we observed that oxidation was critical to this procedure, and that *in situ* Raman was well adapted to investigate it. We were able to characterize the partial oxidation of the seed particles quite well, and distinguish different temperature regimes at which different nanocarbons were preferably grown. Ultimately, CNT yield was extremely low and it was difficult to obtain Raman spectra for individual growing CNTs. An in-depth analysis would require a more mature process with higher yields. However, we recognized oxidative etching as a critical step for C_{60} seed growth and became interested in exploring this process on CNT ensembles. The *in situ* Raman technique that we applied was found to be an effective way to track changes during the etching process. The nanocarbon dispersion techniques that were developed and the good gas flow control method we established during the air oxidation step allowed us to pursue subsequent oxidation experiments.

In the second study (Chapter 3, published in the Journal ACS Nano), we investigated the oxidation process for single-walled CNTs (i.e. SWCNTs) themselves. Thin films of SWCNTs were prepared via CVD, loaded in to our gas flow apparatus and controllably oxidized in air at different temperatures, while being probed with *in situ* Raman spectroscopy. Interestingly, across all runs, we found spectral evidence that metallic CNTs etched faster than smaller diameter semiconducting CNTs. This is an important result because many technological applications require CNTs of only one type (i.e. either semiconducting or metallic), and the type selective etching that we observed could be tracked in real time. Furthermore, we found that the graphitic population declined biexponentially during combustion, across all temperatures. Also, while etch rates of different CNT species was found to vary, the activation energies associated with

these rates was actually found to be similar, likely indicating that the overall chemical steps responsible for etching were similar for these different species.

In our third study (Chapter 4, just published in the Journal Carbon), we were interested in obtaining improved Raman spectra that could more clearly distinguish the difference in etching rates of metallic and semiconducting CNTs observed in the previous chapter. Therefore, the optical setup was modified. While the first two studies only used a single incoming green laser line at 532 nm, a second red laser at 633 nm was added to our system. In this novel *in situ* Raman setup, two distinct Raman spectra could be obtained simultaneously for each laser. This was highly advantageous since a particular set of CNT samples, here produced by laser ablation, could be chosen such that it had metallic and semiconducting CNTs of similar diameter, which were nearly exclusively resonant to the red and green laser lines, respectively. This meant that when both lasers were used, one spectral range would show a population of metallic CNTs, while another spectral range would simultaneous show a population of semiconducting CNTs.

Therefore, in this work, etching was performed on this sample type, primarily using O_2 (diluted in Ar) as the etching gas. O_2 etching proceeded at a rate comparable to air etching. We also examined CO_2 etching, which was similar in many ways, and almost as fast. For both gases, and across all tested temperatures, the metallic CNT populations were again shown to etch more rapidly than the semiconductors, this time by directly comparing one kinetic spectra with the other, we again observed biexponential decay for all resonant graphitic populations. Despite the very different source materials, and the different analysis techniques the evolution was largely similar between the second (Chapter 3) and third studies (Chapter 4), though we did find some differences in the details. Activation energies between different Raman bands were found to be comparable, though not identical.

In summary, we present three distinct etching studies that are thematically linked. In each study, *in situ* Raman spectroscopy is used to track the evolution of nanocarbons. In Chapter 2, we use *in situ* Raman to study the seeded growth of carbon nanotubes. While our resulting yield was very low, we confirmed that oxidation plays a critical role in the growth process, and that *in situ* Raman is an effective tool for tracking the oxidation step. Since nanotubes themselves are useable as precursor seeds for cloning, it

follows that the oxidation of nanotubes should play a similarly important role in cloned growth. More generally, the etching process can be viewed as growth proceeding backwards in time, so the study of etching informs our understanding of nanotube growth and reactivity. Indeed, in Chapter 3, nanotube oxidation was tracked clearly with *in situ* Raman and we found that nanotube population was biased by the oxidation process. In Chapter 4, we used a novel Raman setup to explore this population selectivity more explicitly and in greater detail.

1.2 C_{60} and CNT Structure

1.2.1 C_{60} Structure

Fullerenes are a family of cage-like, nano-sized, carbon allotropes whose theoretical development and experimental study were a direct historical precursor to more recent work with carbon nanotubes.[36] The archetypal, stable fullerene molecule, C_{60}, resembles a soccer ball, which has a polyhedral lattice containing of 20 hexagons and 12 pentagons that are formed by sp^2-like bonds between carbon atoms, as shown in Figure 1.1.[37] Due to energy constraints, no two pentagons directly neighbor each other. Of course the molecule is not planar and its curvature relates to the actual degree of hybridization being $sp^{2.278}$.[38,39] Conceptually, this means that after exciting a 2s electron in a carbon atom to an empty $2p_z$ orbital, we hybridize slightly more than two (but less than three) 2p electrons to the remaining 2s electron to form the skeletal σ orbitals. The particular radial arrangement of the delocalized π orbitals help to stabilize the molecule.[37] Since fullerenes are highly electronegative, they can be reacted with a wide variety of electron-donor molecules and dissolve well in organic solvents such as toluene or, as in the present study, ethanol. In terms of interactions with carbon nanotubes, it is well-known that C_{60} molecules can be trapped within the interior of carbon nanotubes to produce so-called peapod structures.[40,41]

In our work, C_{60} was used as a seed molecule in order to catalyze the growth of single walled nanotubes and to study this growth with our *in situ* Raman system. As originally described in ref [35], it was necessary to partially oxidize the dispersed C_{60} in air in order to open up the molecular cages, which allow would then act as nanotube caps

of specific diameter and chirality.[35,42,43] In principle, by closely controlling the amount and the temperature of oxidation, the structure of seeds could also be engineered, resulting in the growth of nanotubes of controlled chirality or chirality distribution. For reference, the full diameter of a pristine C_{60} molecule is 0.702 nm, which is comparable to the diameters of (9,0), (5,5) nanotubes (see Section 1.2.2 for CNT notation).[37,44]

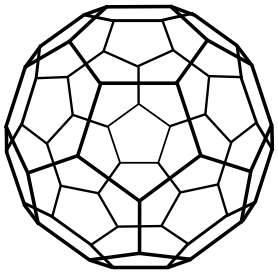

Figure 1.1: Three-dimensional crystal structure of C_{60}. The solid lines represent molecular bonds of hybridized electrons.

C_{60} is meta-stable at room temperature, but due to strain caused by the curvature of the lattice, in terms of enthalpy, C_{60} is less thermodynamically stable than carbon nanotubes, which are in turn less stable than graphite.[37,45] In our work, consistent with prior works,[35,43,46] C_{60} was found to etch at lower temperatures compared to carbon nanotubes, and it was difficult to clearly determine whether C_{60} polymerization occurred during heating or laser exposure.

C_{60} itself can be typically synthesized via methods like pyrolysis of aromatic hydrocarbons or arc-discharge.[37] These methods produce soot with different mixtures of fullerenes, so the species are often separated using differences in solubility. In our work, we use solid C_{60} in black powder form, and it was important to consider whether metal impurities that could catalyze growth were present and active.

1.2.2 Basic CNT Notation and Structure

In this section we give a brief overview of basic CNT structure and terminology. These concepts are already very well developed, and more detailed information can be obtained from the following references: [3,44,47-49]

The molecular structure of an archetypical SWCNT can be conceptually described by taking a one atom thick sheet of graphene, and rolling it in to a seamless cylinder with some diameter, d_t, close to 1 nm. The ends may be left open or closed off with fullerene-like caps. Multiple CNTs of differing diameters may be concentrically placed in to each other, resulting in multiwalled CNTs. Large numbers of SWCNTs may bundle together, twist, or assume any number of configurations. Here, we focus on the basic structure of an infinitely long, straight, pristine SWCNT.

Starting with an undoped graphene sheet, the electronic and optical properties of the SWCNT are largely determined by its diameter and the angle at which the sheet is rolled (i.e. θ, the chiral angle). These uniquely define each CNT, and can be equivalently described by the CNT's chiral vector C_h,

$$C_h = na_1 + ma_2 \equiv (n,m), \tag{1}$$

where a_1 and a_2 are unit vectors shown in Figure 1.2, and n and m are positive integers.

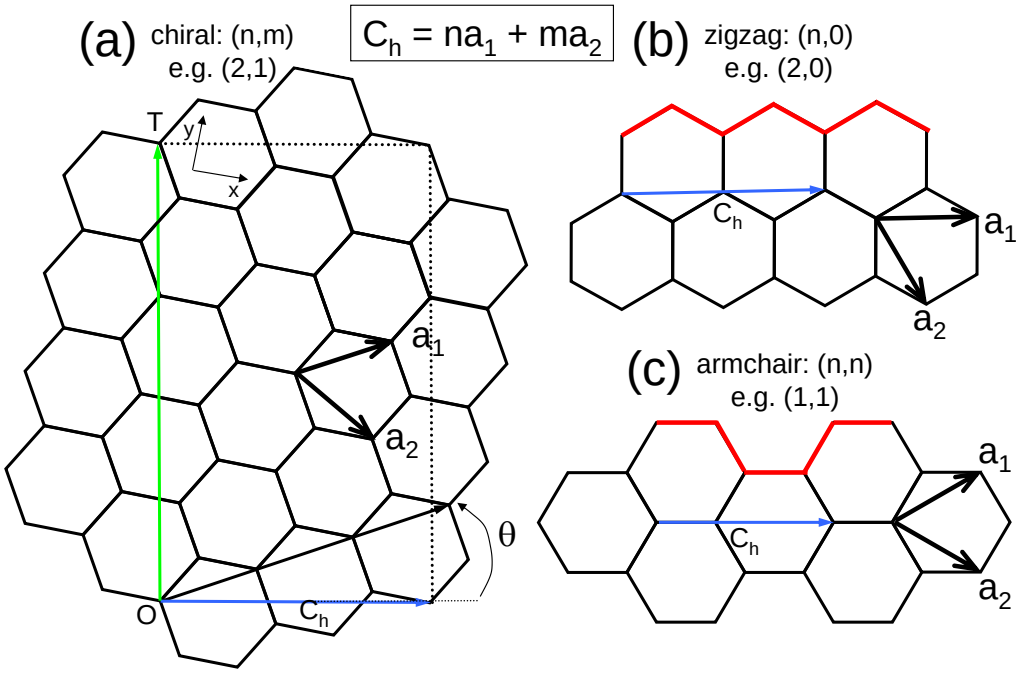

Figure 1.2: Different chiral vectors for basic (a) chiral, (b) zigzag, and (c) armchair nanotube structures. In (a) the area defined by C_h and T define the unit cell of the particular nanotube. Note that the n and m values shown in the above examples would result in nanotubes with diameters too low to actually be stable. Figures adapted from References [3] **and** [47]**.**

Figure 1.2(a) shows the chiral vector for a general chiral CNT. As shown, θ is simply the angle between the C_h and the axis of the unit vector a_1. Because of the symmetry of the honeycomb lattice, the chiral angle can range from $0 \leq \theta \leq 30°$. Geometrically, the chiral angle is simply:

$$\theta = \tan^{-1}\left[\sqrt{3}m/(m+2n)\right]. \tag{2}$$

Similarly, since the magnitude of C_h corresponds to the CNT's circumference, d_t is:

$$d_t = C_h/\pi = \left(\sqrt{3}\right)\left(1.421\text{Å}\right)\left(m^2+mn+n^2\right)^{1/2}/\pi, \tag{3}$$

where the 1.421 Å factor corresponds to the distance between neighboring carbon atoms. Figures 1.2(b) and (c) illustrate the C_h for two special values of θ. In Figure 1.2(b), where $\theta = 0°$ or, equivalently, $m = 0$, the resulting CNT is of zigzag-type. In Figure 1.2(c), where $\theta = 30°$ or, equivalently, $n = m$, the resulting CNT is armchair-type. As we will shortly describe, these two configurations have a direct effect on CNT metallicity.

The lattice vector T, shown in Figure 1.2(a), is orthogonal with C_h and parallel with the nanotube axis, such that:

$$\vec{T} = \left(\frac{2m+n}{d_R}\right)\hat{a}_1 + \left(\frac{2m+n}{d_R}\right)\hat{a}_2 \tag{4}$$

where d_R is the greatest common divisor of $(2m + n)$ and $(2n + m)$. The rectangle outlined by C_h and T defines the unit cell for the CNT.

As shown in Figure 1.3, the reciprocal space of planar graphite and cylindrical CNT can be described in similar terms.

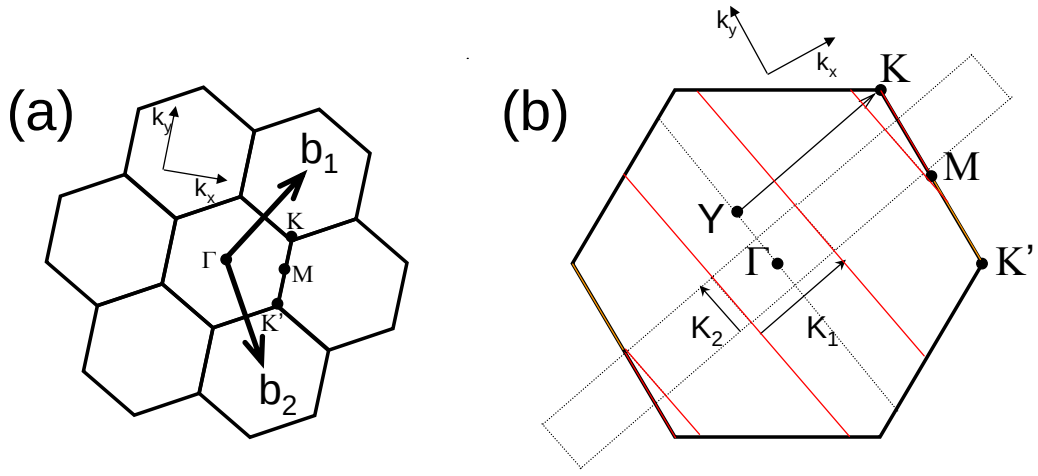

Figure 1.3: (a) The reciprocal lattice of 2D graphite, with high symmetry points shown. (b) The Brillouin zones of a CNT, as represented by the dotted rectangles outlined by $|K_1|$ and $|K_2|$. Cutting lines are shown in red. Figures adapted from references [3] **and** [47]**.**

The reciprocal lattice vectors for 2D graphite can be calculated as:

$$\vec{b}_1 = \left(\frac{2\pi}{(3)(1.421\text{Å})}, \frac{2\pi}{(\sqrt{3})(1.421\text{Å})} \right), \vec{b}_2 = \left(\frac{2\pi}{(3)(1.421\text{Å})}, -\frac{2\pi}{(\sqrt{3})(1.421\text{Å})} \right), \quad (5)$$

with respect to the k_x and k_y axes shown in Figure 1.3(a). For an (n,m) CNT, however, the reciprocal lattice vectors correspond to C_h and T and are therefore dependent on N, the number of hexagons contained in the unit cell for that specific CNT. The corresponding expressions are:

$$\vec{K}_1 = \frac{1}{N}\left(\left(\frac{2n+m}{d_R} \right)\vec{b}_1 + \left(\frac{2m+n}{d_R} \right)\vec{b}_2 \right), \vec{K}_2 = \frac{1}{N}\left(n\vec{b}_1 - m\vec{b}_2 \right), \quad (6)$$

and these vectors are illustrated in Figure 1.3(b) for a hypothetical (2,1) nanotube.

The first Brillouin zones of the CNT correspond to the dotted line segments that run parallel to K_2, with length $2\pi/|T|$. Since the real-space unit cell of graphene is much smaller than that of a CNT (i.e. the area of a single hexagon versus that of numerous hexagons), it follows that the 1D CNT Brillouin zones are much smaller than those of 2D graphene Brillouin zones.

If we assume that the CNT is infinitely long, then the associated wavevectors in that can run along this direction are continuous. In the circumferential direction, however, C_h imposes periodic boundary conditions that restricts wavevector length. We obtain N unique, discrete wavevectors k that run along the K_1 direction. These are also represented by dotted lines in Figure 1.3(b).

It is this quantization that determines the unique electronic structure for each CNT. Since NK_1 corresponds to the reciprocal lattice vector of 2D graphene cut in to N pieces, the electronic energy band structure of a CNT consists of the set of N energy dispersion relations that are simply cross-sectional slices taken from the band structure of 2D graphene.

Undoped 2D graphene is a zero-gap semiconductor, and this vanishing bandgap occurs at the K and K' high symmetry points in the reciprocal space of graphene, shown in Figure 1.3. It follows that if one of the cutting lines (shown in red in Figure 1.3(b)), passes through any K point, then the CNT will have a zero energy gap. More specifically, because the density of electronic states at the Fermi energy is non-zero for CNTs,[3] this CNT will be metallic. Otherwise, if no cutting lines pass through any K point, then the CNT is has a non-zero bandgap and is semiconducting.

This requirement can be expressed in terms of the $\overrightarrow{YK}$ vector in Figure 1.3. If the $\overrightarrow{YK}$ is an integer multiple of K_1 than the CNT is metallic. Geometrically, $\overrightarrow{YK}$ is equal to

$$\overrightarrow{YK} = \frac{2n+m}{3}\vec{K}_1, \tag{7}$$

so for the CNT to be metallic, (2n + m), or equivalently (n-m), must be a multiple of 3. As a result, at room temperature, approximately 1/3 of all possible CNTs are metallic, while the remaining 2/3 are semiconducting. Furthermore, all armchair CNTs (n,n) are metallic, while zigzag CNTs (n,0) are only metallic of n is a multiple of 3. A more indirect implication is that semiconducting CNTs with larger band gaps (~1 eV) have gaps that scale approximately with $1/d_t$.

1.3. CNT Etching

The oxidation of carbon nanotubes, nanocarbons, and catalyst particles required for nanocarbon synthesis occur in large number of studies. For context, we briefly list a few of types of these experiments, with emphasis placed on studies relating to the formation and destruction of pristine carbon nanotubes. The addition of functional, chemical groups (i.e. functionalization) to nanotube sidewalls is itself a wide topic and is not addressed here.

Different wet and gas phase oxidation reactions have been used to selectively remove amorphous and non-graphitic carbon from nanotube samples.[50-53] Depending on the reactions, metal catalyst particles and catalyst support particles may also be removed. Corresponding purification oxidants include a variety of acidic and basic agents, and gas oxides such as O_2 and CO. Notably, the addition of water has been found to play an important role in the high yield, "super growth" studies, in which oxygen is thought to prolong metal catalyst particle activity by removing unwanted amorphous carbon.[54-58]

In a similar vein, smaller diameter nanotubes may also be preferentially eliminated through targeting oxidation, as they are less stable than larger diameter ones.[52,53,59,60] Likewise, single-walled carbon nanotubes are more readily oxidized than multiwalled nanotubes.[61]

Chirality specific etching has also been studied by a number of groups.[62,63] Of particular relevance to the results discussed in this work, the preferential oxidation of metallic nanotube species over semiconducting species has been observed in different studies, as has the preferential growth of semiconducting species in oxidant-assisted synthesis work.[64-69] Less commonly, greater selectivity towards semiconductor destruction has also been observed, as studies using H_2O_2 as an etchant.[70,71]

Experimental methods have progressed to a point where even portions of nanocarbons can be controllably etched. For example, solution based oxidative methods have been used to longitudinally cut or "unzip" carbon nanotubes into graphene nanoribbons.[72-74] These techniques can therefore produce macroscopic amounts of graphene nanoribbons in specific orientations suitable for device fabrication. Another example, is the controlled oxidation of fullerene molecules, which can result in their

cages being partially "opened". The molecules are precursor seeds, which can be used to grow entire carbon nanotubes during synthesis by chemical vapor deposition.[35,42,43]

For the direct study of the kinetics of nanotube oxidation, *in situ* techniques are particularly useful. The thermogravimetric analysis (TGA) of carbon nanotubes is a common way to track and characterize the weight loss that occurs when nanotubes are heated in the presence of oxidants at different temperatures, as they are being destroyed or modified.[75,76] Relevant to the current work, Raman spectroscopy and other nanotube sensitive optical techniques can also been used to track physical changes that occur to nanotubes during oxidation processes.[52,53,77,78].

To conclude this section, for the sake of context, it is worth briefly describing some of the particular metallicity-sensitive oxidation studies mentioned above and the kinds of basic differences that exist between these studies and our own work on nanotube oxidation.

Lukaszczuk *et al.* reported the selective oxidation of metallic nanotubes in air, using TGA, UV-VIS-NIR spectroscopy, and *ex situ* Raman spectroscopy for sample characterization. Selective metal-etching in this study was found to occur optimally at a temperature of 400°C, at very slow etch rates.[64] In our work, changes to Raman spectra were recorded during the etching process itself. We observed greater contrast in the G band lineshapes (see Section 1.4.2.2) produced by resonant metallic and semiconducting species. In neither of our studies did we clearly observe a strong change in selectivity with etching temperatures.

Although ours is an etching study, etching can be part of the growth process. In the CVD growth studies of Yu *et al.* and Zhou *et al.*, enriched semiconducting SWCNTs growth was observed in both studies, using O_2 and water vapor as oxidants, respectively.[67,68] The amount of selectivity in both studies was found to be related to oxidant concentration, although the former work also used sulfur catalyst particles to stimulate large diameter semiconductor growth. Our work, focuses only on the etching of already-grown samples, using fixed oxidant concentrations. However, both growth studies reveal that growing nanotubes are much more easily etched at lower flow rates and with weaker oxidants than already-grown samples.

Selective etching has also been shown under solid oxides in the work of Li *et al.*, in which metallic nanotubes were preferentially etched under solid patterned NiO films.[65]

Overall, our study adds to the picture that metallic SWCNTs are often more reactive than semiconducting SWCNTs. Proposed mechanisms include their lack of bandgap and the availability of electrons near the Fermi level needed to stabilize transition state during bond formation, [64,79,80] as well as the smaller ionization potential of metallic SWCNTs.[67,68,81]

1.4. Raman Spectroscopy

1.4.1 Basics of Raman Spectroscopy

Raman spectroscopy refers to a family of optical techniques that use Raman scattering to directly probe atomic or molecular bonds in materials (i.e. solids, liquids, or gases).[82] Different types of bonds and their arrangements generate distinct vibrational states, which in turn results in unique spectral features at particular frequencies in the Raman spectrum. These spectral lines can then be used to characterize/'fingerprint' the given material.

Raman scattering can occur when a light source is incident on a material. Most of the photons will undergo elastic (i.e. Rayleigh) scattering, such that the outgoing photons will leave with the same frequency as the incident photons. However, a small fraction of the incident photons (e.g. ~0.0001 %) can scatter with optical phonons associated with excited vibrational modes present within the material.[82] The departing photons are said to be Raman scattered and the process is inelastic, such that the scattered and incident photons differ in frequency. If the scattered photon frequency is lesser/greater than the incident photon frequency, we refer to this as Stokes/anti-Stokes scattering.[82]

The simplest kinds of Raman scattering events involve one incident photon scattered with one optical phonon. These general cases are depicted schematically as energy diagrams in Figure 1.4.

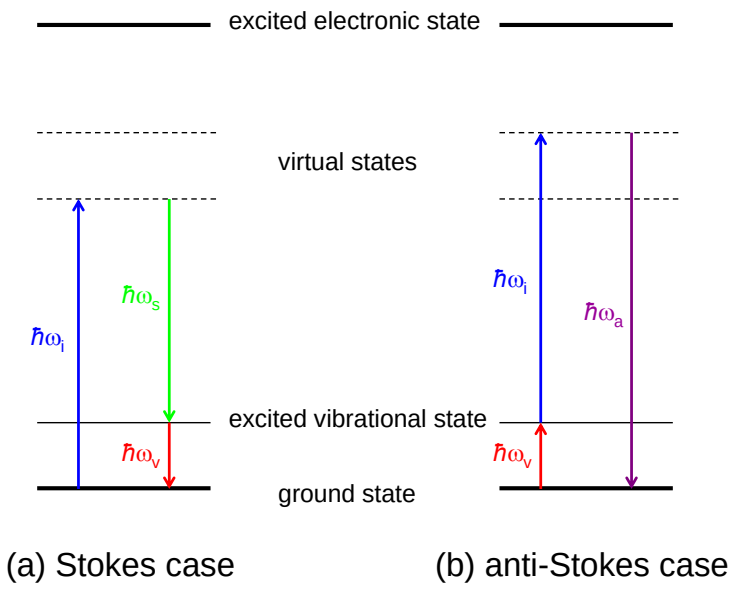

Figure 1.4: Energy level diagrams showing one phonon (a) Stokes and (b) anti-Stokes spontaneous Raman scattering.

Consider a Raman scattering event where an incident photon of energy $E_i = \hbar\omega_i$ interacts with a molecule, where ω is frequency and $\hbar$ is the reduced Planck constant. In the case of Raman Stokes scattering, as shown in Figure 1.4(a), the incident photon can excite an electron from the ground state of the medium to some short-lived virtual state, as represented by the dotted lines. This virtual state can be at an energy below the first real excited electronic state of the system. The excited electron can give up energy and provoke the generation of a phonon of energy $E_v = \hbar\omega_v$.. The electron then relaxes to the ground state as it emits a scattered photon. By conservation of energy, the energy of this outgoing photon is simply $E_s = E_i - E_v = \hbar\omega_i - \hbar\omega_v = \hbar\omega_s$.

In anti-Stokes Raman scattering, existing phonons scatter off the incident light. Depending on the temperature T of the medium, excited phonons have a chance of already being present. Specifically, at thermal equilibrium, compared to the ground state population of phonons, the fraction of photons present with energy $\hbar\omega_v$ is given by the Boltzmann factor $\exp(-\hbar\omega_v/kT)$. Therefore, as shown in Figure 1.4(b), when scattering between the incident photon and pre-existing phonon occurs, the phonon is absorbed, and the scattered photon instead leaves with a higher energy than the incident photon, namely

$E_a = E_i + E_v = \hbar\omega_i + \hbar\omega_v = \hbar\omega_a$. It follows that the intensity of the anti-Stokes scattered light with increase at higher temperature.[82]

In addition to phonons, other excitations (e.g. magnons and plasmons) may also produce Raman scattering.[82] The Raman scattering events discussed in this work are due to optical phonons and in the case of a particular peak of metallic nanotubes, what is described as a plasmon mode.

So long as conservation of momentum is respected, multi-photon and multi-phonon Raman scattering events are also possible. Evidently, the probability for scattering is reduced as the number of scattering events increases. This work is concerned with only a few single-phonon and double-phonon scattering processes.

Essentially all the Raman spectra of SWCNTs shown in this work are obtained through *resonant* Raman scattering. Resonant scattering occurs when the optical absorption or emission process occurs from a real state, instead of from the virtual states depicted in Figure 1.4. One of the most important practical effects of resonant scattering is that scattered light becomes ~10^3 to 10^6 times more intense than in the non-resonant case. For the particular nanocarbons being studied, the optical transitions correspond to transitions of energy difference ΔE between the valence and conduction bands of the different molecules.

For an incident laser light source of energy E_L, two types of resonance processes are possible. Incoming resonance occurs if the optical transition energy matches exactly with the incoming laser energy; that is, $\Delta E = E_L$. Alternatively, resonance can be achieved when the transition energy matches with the energy of the scattered light; corresponding to $\Delta E + \hbar\omega_v = E_L$ for Stokes scattering. This difference in incoming and outgoing resonance energies is large enough that different transitions due to different phonons under the same laser may be easily detectable due to the same incoming resonance condition, but not due to outgoing resonance. Since Raman scattering is weak, the resonant enhancement effect is very important. Evidently, the choice of laser wavelength has a direct effect on which transitions are detectable and which are not. Likewise, increasing the temperature of the medium will increase phonon energies and effect the resonance condition.[82]

1.4.2 Raman Spectra

1.4.2.1 Resonance Enhancement in SWNCTs

As stated, the body of a single walled carbon nanotube (SWCNT) can be visualized as a planar sheet of graphene that has been rolled up to form a seamless cylinder. The angle at which the sheet is rolled and the diameter of the cylinder determines the chirality of the nanotube. Chirality has a direct influence on the electronic properties of a SWCNT, and can be equivalently characterized by a pair of lattice vectors in the index (n,m). As mentioned previously, due to their different chirality, 2/3 of all possible SWCNTs species can be classified as semiconductors, while the remaining 1/3 are metals. [48,49]

Raman resonant enhancement in sp^2 carbon nanostructures differs depending on the molecule. Undoped, planar graphene is a zero-band gap semiconductor and resonance enhancement of Raman scattering can be obtained for any incoming laser wavelength.[25] In contrast, resonance enhancement in SWCNTs can only be achieved at certain wavelengths, although the enhancement is much stronger. This is due to the presence of distinct peaks called van Hove singularities in the quasi-1D density of states (DOS) present in all SWCNT structures. The difference in energies between pairs of peaks above and below the Fermi level can be matched to laser energies.

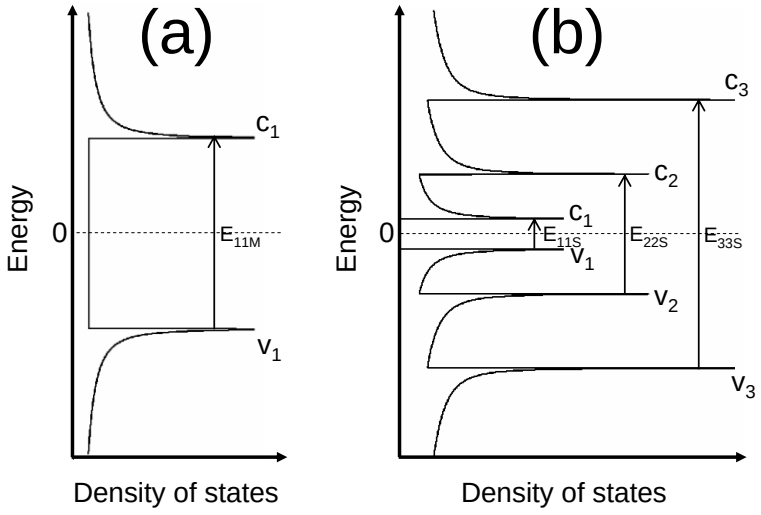

Figure 1.5: Schematic of electronic density of states for (a) a metallic carbon nanotube and (b) a semiconducting carbon nanotube. Conduction and valence bands are labeled, as are possible optical transitions between bands. Figures adapted from Reference [83]**.**

A schematic of the electronic DOS for a metallic and semiconducting carbon nanotube are illustrated in Figure 1.5. Here, optical transitions from valence band *i* to conduction band *i* are labeled E_{ii}. For example, the transition between the second highest valence band (v_2) to the second lower conduction band (c_2) is the semiconductor is called the E_{22S} transition. Therefore, incoming or outgoing photons with energies E_{ii} are required to produced resonantly enhanced spectra. Note that sharp van Hove singularities are also present in the phonon DOS (not shown).

The following section will discuss relevant Raman peaks that were analyzed from SWCNT and C_{60} spectra. Other peaks are identifiable, but were not used for characterization in our work.

1.4.2.2 Experimental CNT Spectra

Figure 1.6 shows a typical SWCNT Raman spectrum at low frequency on a Si/SiO_2 substrate. Different Raman bands are described in detail below.

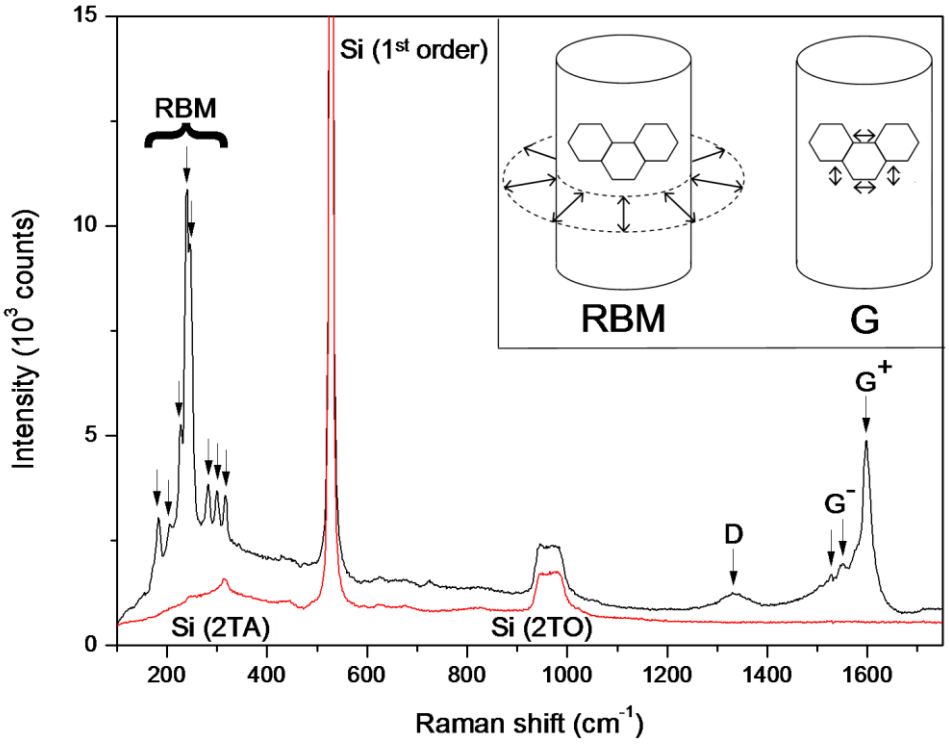

Figure 1.6: Raman bands for a typical SWCNT sample we have synthesized by chemical vapor deposition (black) and its accompanying silicon background (red). The CNT sensitive RBM, D, and G bands are indicated.

G BAND:

All graphitic sp^2 materials experience C-C bond stretching, which produces an intense first-order peak known to as the G band. In other words, the G band intensity is proportional to the amount of sp^2 carbon that is present, so long as the G band is non-resonant, or if equally resonant spectral features are being compared. The phonon modes responsible for this peak are the longitudinal optical (LO) phonon mode and in-plane transverse optical (iTO) phonon modes. In planar graphene, these modes are degenerate, resulting in a single peak.[25,26] In SWCNTs, these modes are not degenerate, with the LO phonons corresponding to vibrations along the length of the nanotube axis, and iTO phonons corresponding to vibrations around the circumference of the nanotube.

As a result, the G band from a carbon nanotube is split in two peaks, a high frequency G+ (at ~1590 cm^{-1}) and a lower frequency G-.[25] The G- peak frequency is sensitive to metallicity and doping, and increases with larger nanotube diameters. In contrast, the G+ position remains roughly fixed for different nanotube types, even if the phonons responsible for each peak differs for metallic and semiconducting species.[27,84,85] Multiple G- peaks in a spectrum indicate the presence of multiple resonant nanotube species, and in some cases these peaks can be used to assign SWCNT chirality.

Of fundamental importance to our studies is finding that the spectral lineshape of the G- peak is highly dependent on whether the corresponding resonant SWCNT species is semiconducting or metallic. For a semiconducting species, both the G+ and G- peaks can be fit to narrow, symmetric Lorentzian lineshapes. For a metallic species, in contrast, the G- peak takes the form of a broad and asymmetric shoulder that can be fitted by a Breit-Wigner-Fano (BWF) function.[25,26] Metallic SWCNTs are susceptible to the Kohn-anomaly effect, such the corresponding phonon energies will fall to zero at certain frequencies. Since this has an influence on G band spectral width and frequency, performing eletrochemical doping experiments, while tracking the G band, is one possible way to determine the Fermi energy (E_F) of the nanotube, and therefore nanotube chirality.[86]

D band:

The D band is a two-peak structure associated with a one-phonon scattering process at ~1300-1350 cm^{-1}.[25,26] Its intensity is enhanced due to a double resonance process (i.e. here involving one electron and one phonon). The D band intensity is proportional to the density of defects in graphitic samples, regardless of the cause (i.e. disorder-induced Raman modes). It is common to characterize sample purity by taking the ratios of the D and G bands intensities (i.e. D/G ratio). D band width and frequency is sensitive to what species of nanocarbons are present and are sensitive to CNT diameter.[47,87,88]

2D BAND:

Graphitic sp^2 materials also possess a strong second order band known as the 2D or G' band. In the associated two phonon scattering processes, two of the intermediate states correspond to real electronic states, and this double-resonance effect causes the band to have an intensity comparable to that of the G band if the material is relatively defect free.[25] The 2D peak intensity is proportional to the amount of sp^2 carbon present for non-resonant or equally resonant species, but is also affected by the presence of defects. For SWCNTs, the 2D band occurs as an overlapping two-peak structure at roughly ~2650 cm^{-1}. The 2D band frequency is also sensitive to the amount of bundling and doping present in the nanotube sample.[25,26]

Radial Breathing Modes (RBMs):

Radial Breathing Modes (RBMs) are lower frequency Lorentzian peaks (~100-~400 cm^{-1}) that are unique to the Raman spectra of carbon nanotubes. They are created by the radial vibrations of carbon atoms in the cylindrical nanotube sidewalls. The nanotube expands and contracts radially. The frequency of a given RBM (ω_{RBM}) is inversely proportional to the diameter (d_t) of the corresponding resonant nanotube. This relationship can generally be described by the equation:

$$\omega_{RBM} = \frac{227}{d_t}\sqrt{1 + C_e * d_t^2}$$

where C_e is a environmentally dependent fitting parameter relating to van der Waals interactions with the medium, ω_{RBM} is given in cm^{-1}, and d_t is given in nm.[26] Therefore, if an accurate C_e value is chosen, a SWCNT diameter can be assigned to a given RBM peak.

Note that the RBM intensity for large diameter nanotubes (> 2 nm) is usually very weak.[26] Furthermore, multi-walled nanotubes will often not produce well-defined RBMs due to spectral broadening.[26]

1.4.2.2 The Kataura Plot:

Importantly, the optical transition energy (E_{ii}) values for different SWCNT chiralities can be determined either theoretically or experimentally, and plotted as a function of SWCNT diameter. These E_{ii} versus d_t (or ω from the RBM) plots are known as Kataura plots. For a known laser transition energy $E_{LASER} = E_{ii}$ with resonance window ΔE_{ii}, it is therefore possible to match a known diameter d_t with a particular nanotube chirality (n,m), or at a range of possible chiralities.

A possible Kataura plot using optical transition energy data from the work of Saito *et al.*[89,90] is shown in Figure 1.7. Note that the value of the transition energies also depend on environmental effects, which are sensitive to how the nanotubes were synthesized and any postprocessing. In the Figure, we show result for an idealized "supergrowth" sample, whereas in practice we would shift the energies based on the equation $E_{ii} = E_{ii}^{SG} - \check{C}_\kappa [A + B(p/d_t) + C(p/d_t)^2]$, in which p relates to the cutting line index for each E_{ii} transition energy, whereas A, B, and C are sample dependent fitting parameters, and $\check{C}_\kappa$ depends on the surrounding material system.[89,90,90,91]. These fitting parameters model the effects of the environment changing the electronic structure such as by changing the dielectric constant.

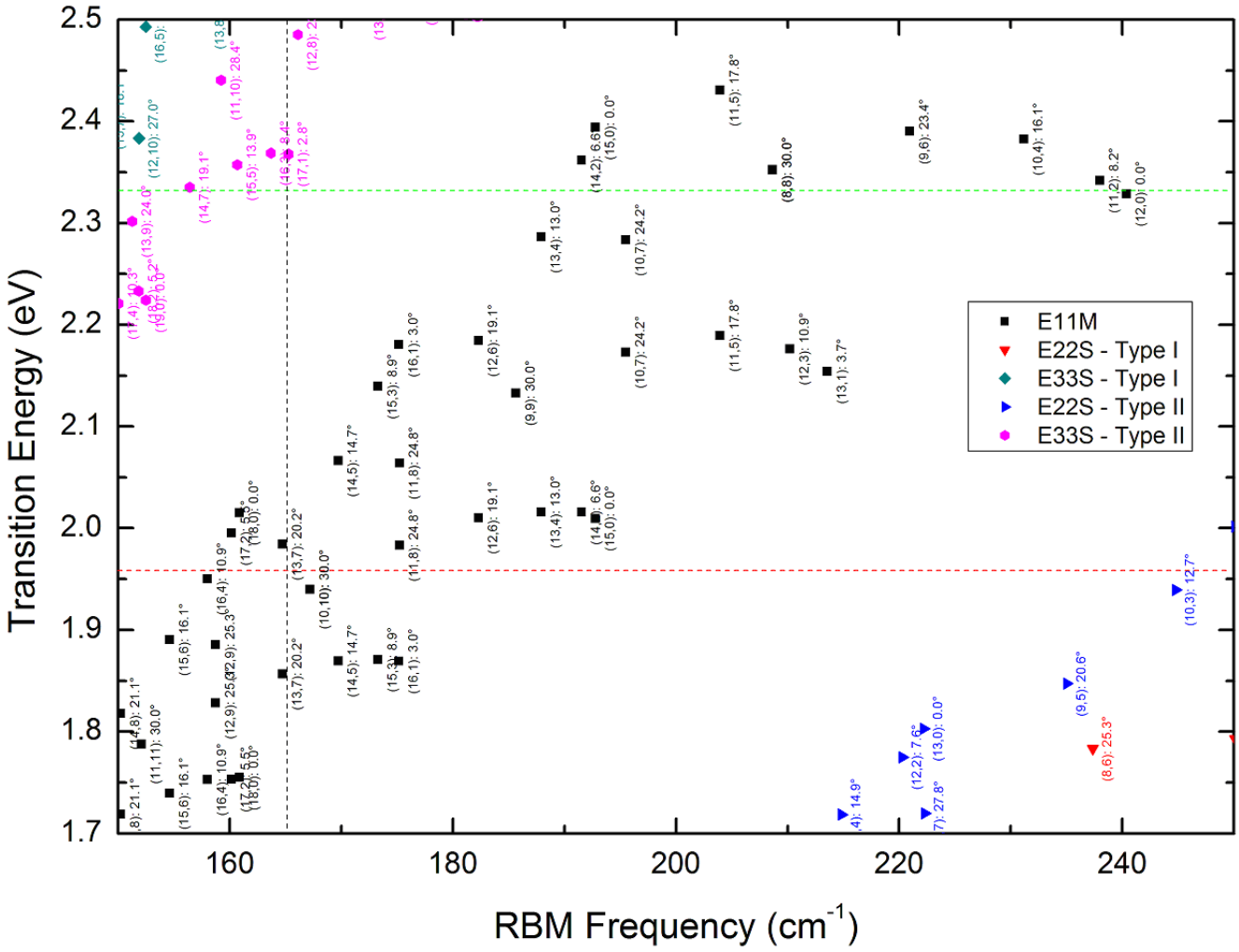

Figure 1.7: Example of a Kataura plot. This plot is generated with optical data obtained from Saito *et al.* [89,90] **Different colored points correspond to the different optical transitions of particular nanotube species/chiral angles which are labeled by (n,m) and chiral angle beneath. Notice the gap between the metallic E_{11}^{M} species and other semiconducting species. See text for more information.**

In Figure 1.7, two lasers lines, namely a green laser (532 nm) and red laser (633 nm), like the ones used in our experiments are displayed as dotted green and red lines, respectively. In principle, a visible RBM frequency (e.g. at 165 cm^{-1}), can be assigned to given resonant nanotube species, but if multiple resonant species are in proximity to the intersecting lines, assignment to a specific species can be difficult. This is further complicated by the fact that even if correct C_e and A, B, and C factors are chosen for the frequency assignment and energy assignment respectively, the optical energies also have inherent uncertainties associated with the differences between experimental data and

theoretical calculations.[89,90] In other words, unambiguous assignment of different RBM species is not always possible depending on the resonant laser line values and RBM frequencies. In practice it is possible to assign (n,m) for the smallest diameter nanotubes (<1 nm) but for large diameter nanotubes it may only be possible to assign them to a particular band.

One other point is that there can be other ways of deducing the diameter of nanotubes within the resonant Raman spectra, such as by the G- frequency for semiconducting nanotube.[92] This information can be used to construct different Kataura plots, which can then be contrasted with RBM data. Here, other factors, such as the resonance window widths for different Raman structures, may influence assignment.

1.4.2.3 C_{60} Spectra

A typical Raman spectrum for a C_{60} single crystal will have over 30 low intensity spectral modes, however the $A_g(2)$ peak is by far the most intense mode and was found to be a useful indicator of relative C_{60} concentration during our etching experiments.[93-95]

$A_g(2)$:

The $A_g(2)$ mode corresponds to one of the two A_g modes, which are both Raman active. It corresponds to a pinch mode, somewhat analogous to a G band, and represents C-C bond stretching on the surface of the C_{60} molecule.[93-95] In air, it occurs at 1468 cm^{-1} as a sharp peak with a long high frequency tail. The other A_g mode, $A_g(1)$, is a breathing mode at 496 cm^{-1}, but is considerably less intense than the $A_g(2)$ mode.[93-95] Experimental $A_g(2)$ peaks are shown in Figure 2.2.

1.4.2.4 Background spectra from the substrate:

All analyzed nanotube and C_{60} samples were deposited on crystalline silicon substrates with SiO_2 present. Therefore a sharp first-order Lorentzian peak from Si at 520 cm^{-1} is present across all Raman spectra.[96] This background peak was useful in helping to calibrate the spectral setup and in helping to correct for sample movement in many experiments.

As shown in Figure 1.6, second order transverse acoustic phonon overtones produced an uneven background from 200-500 cm^{-1} and overlapped with the presence of RBMs in SWCNTs.[96] This made it more difficult to track the intensity and spectral evolution of individual RBMs in this region. Second order transverse optical bands are also present at around ~950 cm^{-1}.[97,98]

1.4.3 Raman Apparatus

The *in situ* Raman spectroscopy apparatus used for our two laser work is described and displayed schematically in the Appendix of Chapter 4. Previous incarnations of the same setup only included a 532 nm laser and associated optics, but were otherwise very similar to the two laser setup.

A basic Raman setup consists of an incoming laser, cleaned through a bandpass filter, that is passed through some system of lenses and focused on to a Raman-active sample. The scattered light is collected and passed through an edge or notch filter in order to remove the strong Rayleigh signal arising from unscattered laser light, and is directed in to a spectrometer to produce a spectrum that is collected on a CCD. Components like slits are useful for optimizing signal resolution, at the cost of limiting signal intensity.

Global Raman Imaging (GRI), a variant of this setup, was used throughout this work to image and monitor nanocarbon presence and beam focusing conditions, while concurrently collecting spectral data. In our C_{60} work, GRI was actively used to monitor nanocarbon growth on oxidized C_{60} structures. Our GRI setup was developed by Kaminska *et al.* and used for CNT research.[30-32] Here, the laser is passed through a defocusing lens to produce a relatively large spot on the sample. The Raman signal is

passed through a filter in order to track a limit the signal to a certain Raman shift range of interest. Then the resultant Raman signal is projected on to a CCD and can be monitored as live changes occur on the sample. In the case of CNTs, filters can be chosen so that the Raman image contains signal from the spectral range containing the G band, allowing one to visually monitor the status of graphitic carbon on the sample,

2 SEEDED GROWTH WITH C_{60} AND C_{60} OXIDATION

2.1 Overview

The use of fullerenes as a seed material for the chemical vapor deposition (CVD) growth of carbon nanotubes (CNTs) has been reported, instead of commonly used metal catalysts.[35,99,100] Since C_{60} molecules are identical, they have a uniform size distribution and might be used to grow CNTs with improved diameter and type control when compared to metal nanoparticles. In this study, the hot-walled CVD growth of graphitic carbon, carbon nanofibers, and CNTs is obtained from C_{60} using ethanol as the precursor. Samples are characterized by *in situ* and *ex situ* Raman spectroscopy, global Raman imaging, and *ex situ* scanning electron microscopy. *In situ* Raman, in particular, was applied as a means of gathering kinetic data of the etching process. The different stages of etching, nucleation, and nanotube growth using C_{60} have not been explicitly studied using kinetic techniques, and we are interested in learning how to better control this processes precisely.

We confirm that, as reported by Yu *et al*.,[35] a pre-growth oxidation step performed at a minimum temperature yields small quantities of single-walled or thin multi-walled CNTs. By varying sample preparation, oxidation, and CVD conditions, we observe substantial changes to nanocarbon yield and relative abundance.

2.2 Introduction

The chemical vapor deposition (CVD) growth of carbon nanotubes is commonly performed using metal catalysts, which are important for high yield growth required for most applications of CNTs. However, non-metal catalysts such as SiC and different oxides are also well known, and in recent years pure carbon catalysts have been explored in self-assembly growth studies.[42]

For example, SWCNT growth from nanosized diamond particles has been achieved, and growth from carbon nanoring templates or various end-cap molecules have been proposed.[100-103] Similarly, nanotube cloning has been achieved by groups such as Yao *et al.* and Liu *et al.* , which involves producing short SWCNT segments and growing new SWCNTs directly from these "seeds", either by CVD or vapour-phase epitaxy.[14,104] Importantly, in these studies, the chirality of the cloned SWCNTs remains the same as the original seeds. In a similar vein, Sanchez-Valencia *et al.* were able to use $C_{96}H_{54}$ precursor molecules to achieve the chirality controlled growth of (6,6) SWCNTs.[105] Since the production of high yields of diameter-controlled, single-chirality SWCNTs that are viable for industrial applications still has not been fully realized, there is significant motivation to continue developing seeding methods.

Our study used C_{60} as a seed material for SWCNT growth, closely following the method established by Yu *et al.*, with the ultimate goal of tracking SWCNT growth using *in situ* Raman spectroscopy.[35] Currently, carbon nanotube growth from fullerene seeds has been successfully achieved by a number of groups, although no kinetic data during growth was collected by these groups.[35,43,106] Using ethanol vapor, we obtained not only carbon nanotubes, but also graphitic carbon and carbon nanofibers. Generally, SWCNT growth was difficult to track due to extremely low overall SWCNT yield.

2.3 Method

The procedure was based on that of Yu *et al.*.[35] A C_{60} solution was prepared by diluting ~10 mg of powdered C_{60} into a vial containing 20 mL of anhydrous ethanol, and ultrasonicating for 20 minutes. For each prepared sample, ~50 µl of the solution was collected and drop-casted on to individual pieces of 0.5 mm thick Si substrate with a 1µm thermal SiO_2 layer. These samples were heated in air to 150°C to vaporize the ethanol and cooled to room temperature.

The sample oxidation and CVD growth steps are depicted schematically in Figure 2.1.

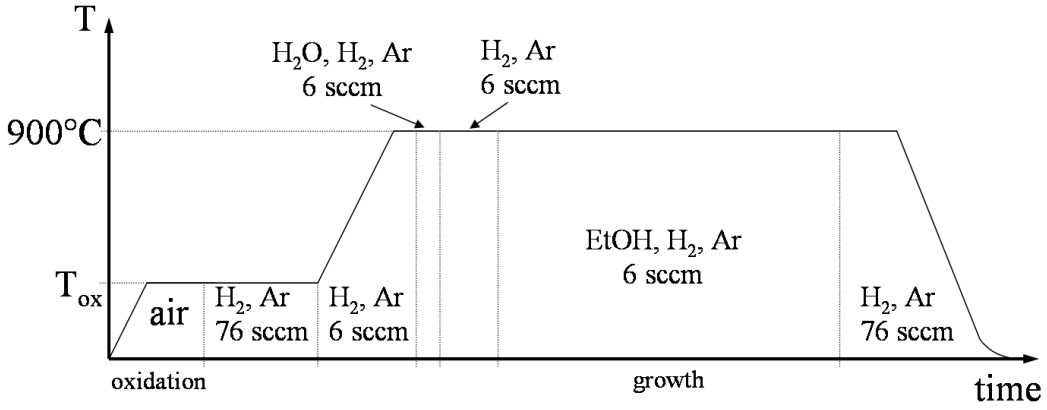

Figure 2.1: Oxidation and CVD growth steps applied to each C_{60} sample.

After being loaded in the CVD reactor, each C_{60} sample was heated in ambient air to a fixed oxidation temperature, which was varied between 25-800°C at a rate of 100°C/min. Oxidation and was performed to partially open and activate the C_{60} seed particles. The Raman spectral evolution of the sample is tracked and air oxidation is terminated after the Ag(2) peak, an indicator of C_{60} concentration, vanishes or stops changing. The reactor is then purged with a 2% H_2:98% Ar mix flowed in at 76 sccm. Once the reactor is flushed out, the gas flow is reduced to 6 sccm and the sample is heated to 900°C. At 900°C, water is introduced by bubbler in to the reactor for 10 minutes, and the reactor is again flushed out with H_2:Ar at 6 sccm. Water is introduced in

order to re-oxidize and activate the opened seed particles. Ethanol vapor is flowed in to the reactor by reactor as a source gas to stimulate SWCNT growth for > 1 hour, and growth is terminated by purging out the reactor with H_2:Ar at 76 sccm and cooling the sample back to room temperature.

2.4 Results and Discussion

Oxidation of the C_{60} samples was tracked with *in situ* Raman spectroscopy and imaging, using the previously described single-line 532 nm Raman setup. Figure 2.2 depicts typical Raman spectra of a sample in ambient air, as the temperature is gradually raised from room temperature to 800°C at a rate of 100°C/min.

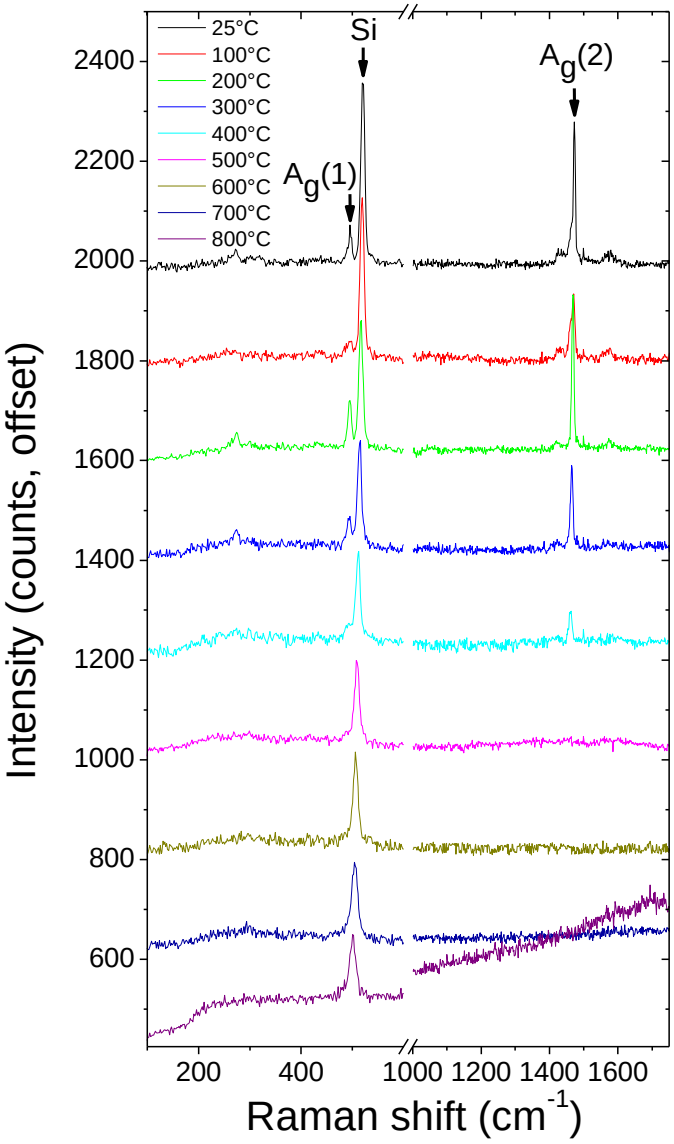

Figure 2.2: Raman spectra of C_{60} pre-growth sample undergoing air oxidation from T=25°C to 800°C, as sample is heated at 100°C/min

The $A_g(2)$ peak at ~1470 cm^{-1} is relatively intense and a good indicator for the amount of C_{60} remaining on the sample at any one time. Importantly, etching causes rearrangement and movement of C60 particles on sample surface, and a temporary dip in $A_g(2)$ peak intensity at around 100°C. As temperature is increased, the sample is

progressively oxidized away and flushed in to the exhaust. Note that increasing temperature causes a gradual peak down shift of a few cm^{-1} by 400°C and an increase in spectral blackbody, especially above 700°C. The integrated intensity of the $A_g(2)$ peak can be extracted and background subtracted as shown in Figure 2.3.

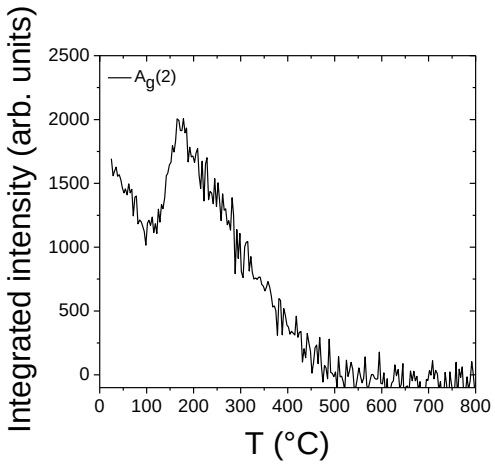

Figure 2.3: Decay of background-corrected integrated intensity of $A_g(2)$ from Figure 2.2.

Initially, as the sample is heated prior to ~250°C and tracked via global Raman imaging, the C_{60} clusters on the samples appear to be unstable in size and undergo rearrangement on the substrate surface. Although the actual reactions occurring are unclear, this can result in an initial drop or rise in $A_g(2)$ band peak intensity.

However, after 350°C, there is a clear and rapid loss in $A_g(2)$ intensity. At around 500°C, the $A_g(2)$ peak cannot be seen above the spectral background, indicating that only low levels of C_{60} are left on the sample.

The temperature at which the oxidation step was performed was found to have a clear effect on what was grown following ethanol input at 900°C. Figure 2.4 shows SEM images of samples taken without oxidation, both with and without ethanol input.

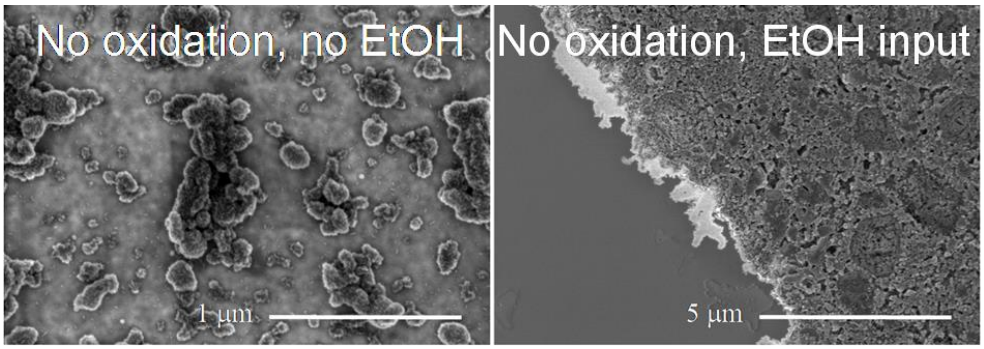

Figure 2.4: SEM micrographs showing sample material without performing air oxidation, both with and without ethanol input. In either case, no nanotube growth occurs.

Evidently, in both cases, no SWCNT growth is observed. Without ethanol input, from the image, there is no clear change to the clustered C_{60} material, both before and after heating, With ethanol input, there is a some buildup of amorphous carbon over the large C_{60} agglomerations following growth.

When the oxidation step is performed, the kinds of growth obtained varied significantly on the oxidation temperature that the samples were exposed to. Figure 2.5 shows SEM micrographs of post-growth samples that were oxidized at different temperatures.

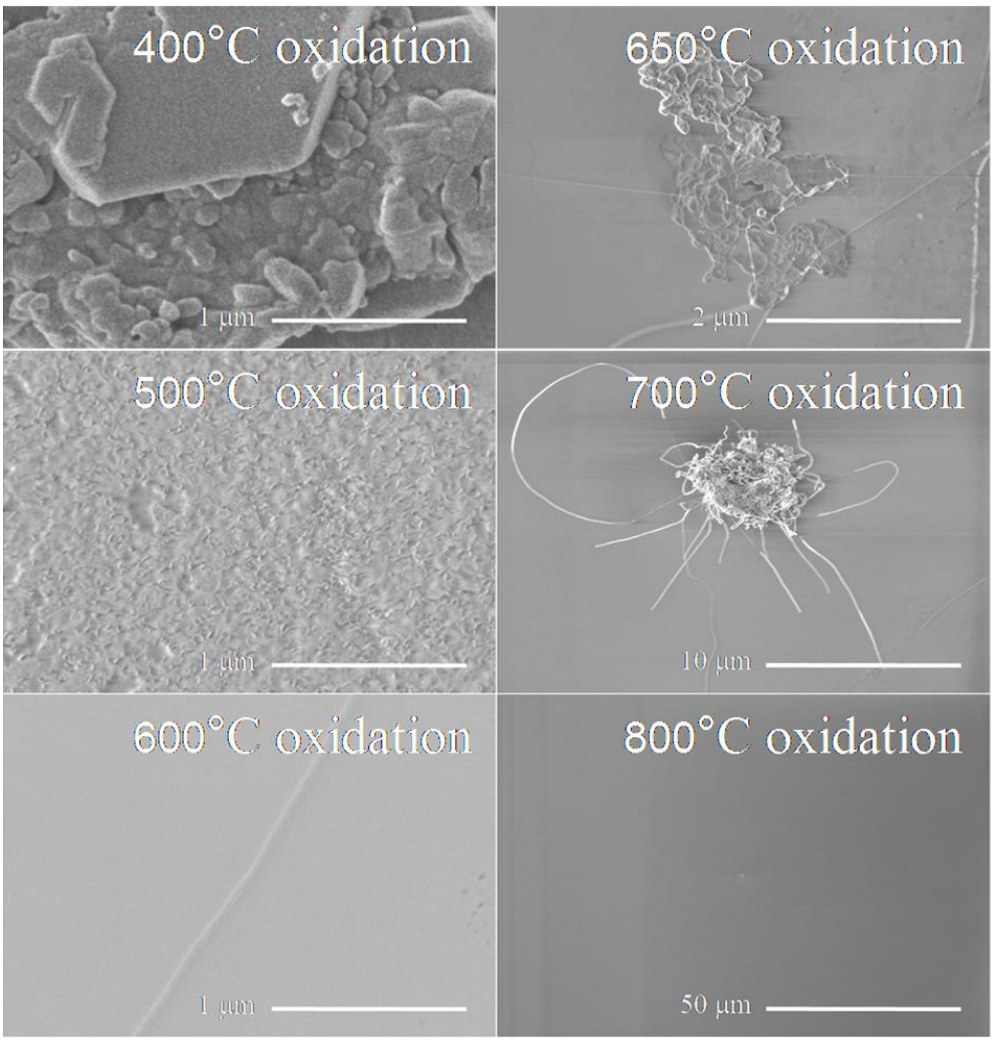

Figure 2.5: SEM micrographs of post-growth samples that were etched in air from T = 400°C - 800°C.

At oxidation temperatures below 500°C, the C_{60} clusters have not been sufficiently broken up and graphitic carbon is formed on the sample surface. SWCNT growth is only achievable at oxidation temperatures between 500°C-800°C. In these cases, the surface density of the oxidized C_{60} islands is quite low, and we observe the appearance of nanotubes and nanofibers, which peaks at around an oxidation temperature of 700°C. Above 800°C, all the C_{60} seeds have been destroyed and no growth is possible upon ethanol introduction.

These observations agree with the obtained Raman data. Figure 2.6 shows Raman spectra from samples that were not sufficiently etched to produce SWCNT following the growth.

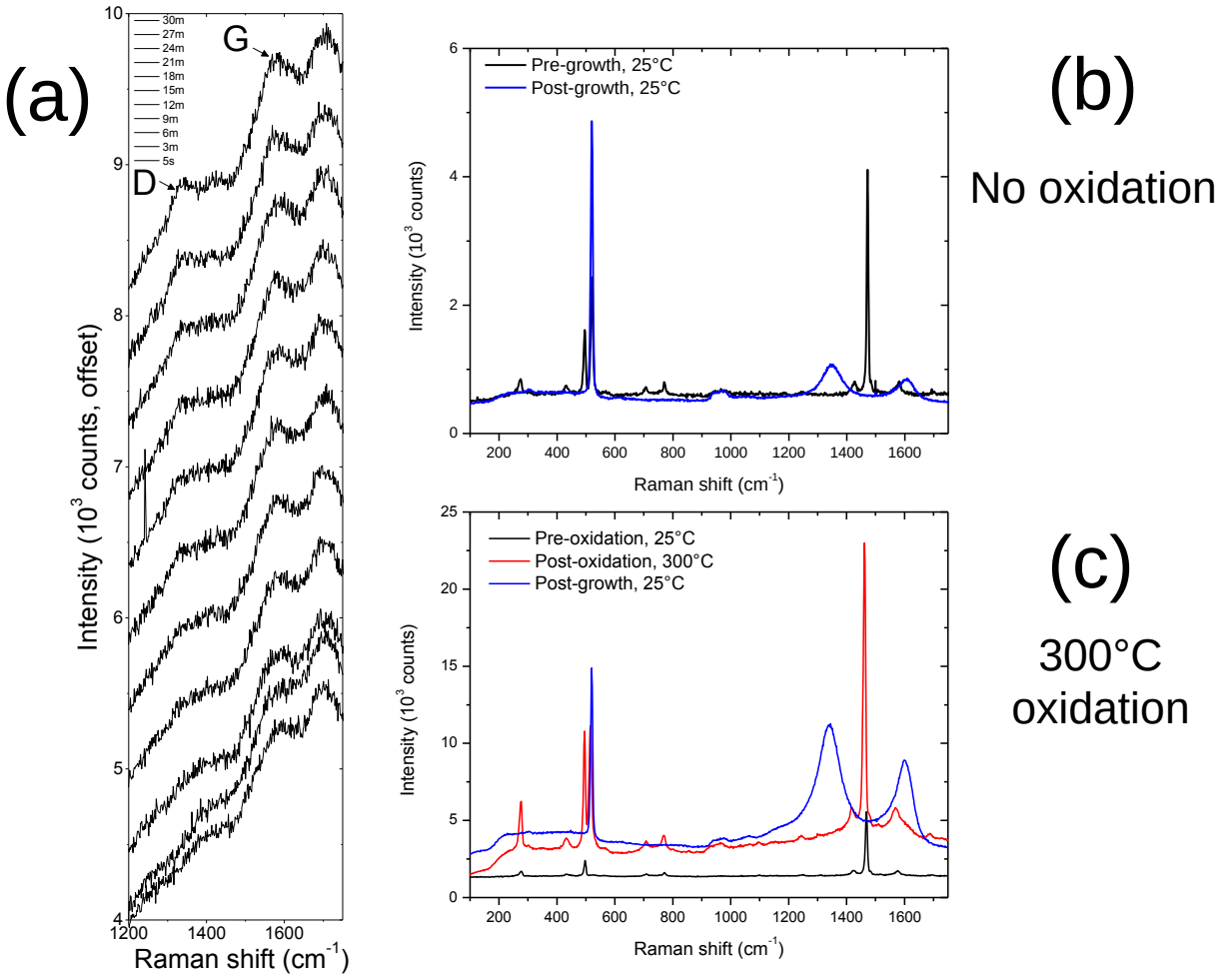

Figure 2.6: (a) Kinetic Raman spectra of sample exposed to ethanol at 900°C, with no oxidation step. Frames were exposed for 1 sec, at 3 minutes intervals, during the first 30 minutes of growth. (b) Comparison of spectra before and after growth at room temperature, when no oxidation step was performed. (c) Comparison of analogous spectra, when a 300°C oxidation step is performed. Spectra in (b) and (c) are taken with 15 sec exposures.

In Figure 2.6, for all spectra, we see a substantial rise in the D band intensity following growth when insufficient etching is performed, along with the disappearance of the $A_g(1)$ and $A_g(2)$ peaks for C_{60}, suggesting that whatever C_{60} that survived the heating process, was covered in thick layers of amorphous carbon. The post-growth D bands in (b) and (c) are substantial indicating the heavy build up of defective graphite. No such increase in the D or G bands occurs at high etch temperature samples, as graphitic accumulation does not occur in these samples.

Despite using different C_{60} solution concentration and deposition methods, SWCNT growth was always quite low, even under optimal conditions. As a result, there was insufficient SWCNT material to generate Raman bands that were intense enough to extract reliably during the growth process. However, occasionally it was possible to visually track the formation of short nanofibers using global Raman imaging. Figure 2.7 depicts this growth occurring on activated C_{60} seeds at 900°C, following oxidation at 700°C.

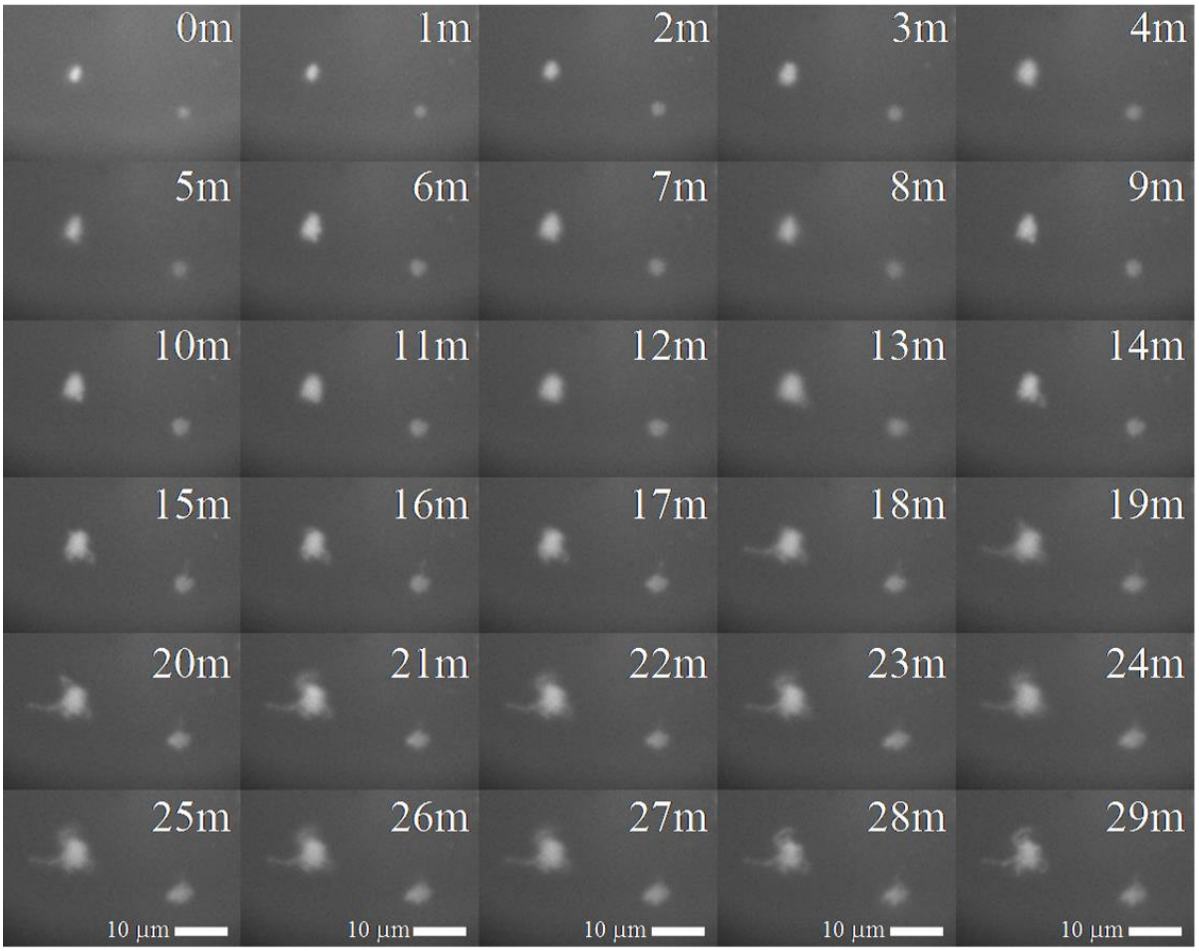

Figure 2.7: Global Raman imaging (at ~1400-1700 cm^{-1}) of nanofibers emerging from C_{60} clusters at 1 minute intervals during CVD growth with ethanol at 900°C, with oxidation performed at 700°C.

From Figure 2.7, one can observe both seeds gradually accumulate mass, which are likely graphitic, prior to nanofiber formation. The growth rates and the times at which the fibers emerge and then cease growing are not uniform. The growth profiles of distinct nanofibers can be tracked visually, as shown in Figure 2.8.

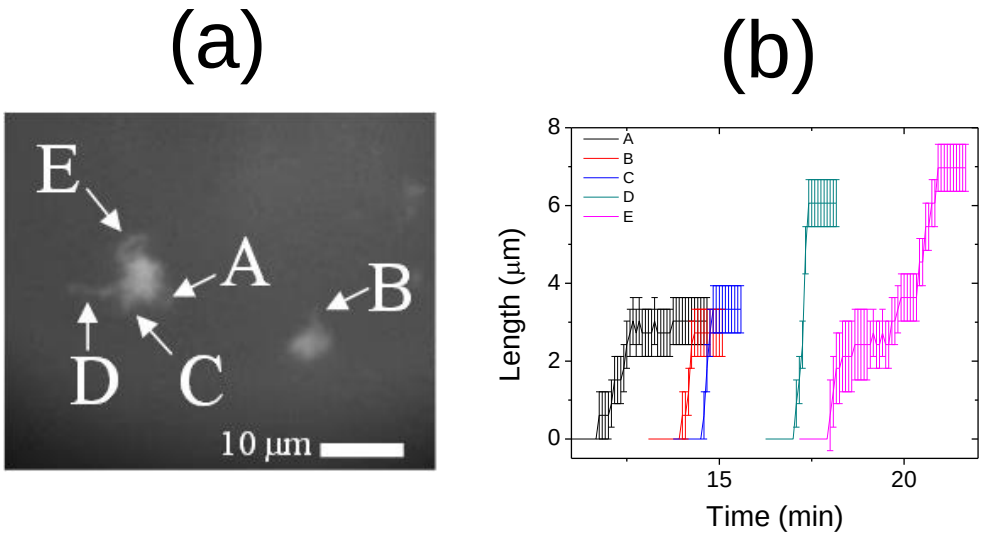

Figure 2.8: (a) Labeling of 5 separate nanofibers from Figure 14. (b) Growth evolution of the nanofibers during 30 minutes of ethanol exposure.

From Figure 2.8(b), one notices that fibers A, C, D, and E all emerge from the same seed particle, but all at different times, and only when the previous fibers has stopped growing. It's unclear what causes growth termination, but it seems possible that the nanofibers are competing for carbon source material on the seeds themselves and that there is only enough accumulated carbon on the seed to allow for the growth of only one nanofiber at a time.

The presence of SWCNT growth was also verified via photoluminescence (PL), as shown in Figure 2.9, using a diluted C_{60} seed solution and deposition by hand stamping on to a Si substrate with trenches. SWCNTs suspended in air are known to fluoresce strongly in the infrared when excited by visible light.[107-109] Therefore, PL imaging can rapidly image individual suspended SWCNTs.[110] On these samples it was very rarely possible to observe suspended SWCNTs with lengths of about 50 μm. PL images of these samples were taken on a custom PL imaging setup. [110]

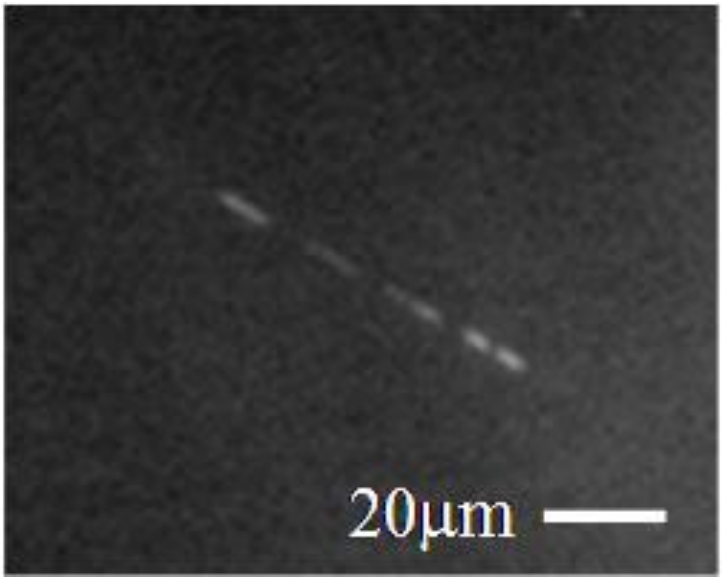

Figure 2.9. Near-infrared photoluminescence image of a grown SWCNT, suspended in air over patterned silicon trenches. The suspended regions have enhanced visibility.

2.5 Conclusions

To summarize, graphitic carbon, carbon nanofibers, and SWCNTs were all successfully grown using C_{60} seeds following oxidation using air and water vapor, during high temperature CVD growth in ethanol vapor. The destruction/opening of C_{60} seed particles could easily tracked using *in situ* Raman spectroscopy and imaging and the air oxidation temperature determined which nanocarbon structures formed during growth. At oxidation temperatures below 500°C, large masses of C_{60} remained intact, which were subsequently coated with defective graphitic carbon . Above 500°C, most of the C_{60} is etched away, but surviving seed particles are successfully activated and contribute to the formation of low density carbon nanofibers and SWCNTs. SWCNT yield was very low, and highest when C_{60} is in low abundance.

To obtain nanotube growth with ethanol, we verified the necessity of a pre-growth oxidation step in order to activate C_{60}, presumably by opening and removing traces of defective carbon. Notably, i*n situ* Raman tracking was found to very effective at tracking material in this step. This has the potential to be very important, since the oxidation step which proceeds the growth phase must be well controlled.

Although further experiments exploring SWCNT growth kinetics were not possible due to this low yield, the etching apparatus was fully developed and full control over etching rates while performing *in situ* Raman spectroscopy was demonstrated. More importantly, species specific cloning remains an important direction of research for the nanotube growth community. Since cloning often involves cleaving pre-existing nanotubes, and the etching process itself is species-selective, we decided to shift our investigation to the SWCNT etching process.

3. SELECTIVE ETCHING OF SWCNTS IN AIR TRACKED BY *IN SITU RAMAN*

Foreword

In this published work, we used the air oxidation setup to controllably etch CVD growth SWCNTs with probing them with single laser *in situ* Raman spectroscopy. The combustion process was found to be a chirally-sensitive process, with metallic species etching faster than semiconducting species. This occurred even if the metallic species would have had more thermodynamically stable structures, if diameter were the only consideration. The decay kinetics of graphitic species, individual SWCNT species, and defective carbon were contrasted with each other, with both the defective and graphitic species experiencing biexponential decay.

Single laser spectroscopy was found to be a simple and effective way of tracking chemical changes to different SWCNT species in real-time, such as for species of different diameter, and it indicated that metallic type selective etching had occurred. However, in this work we used only a single laser for *in situ* spectroscopy. While practical, we realized that this approach also has some drawbacks, and so we added an additional laser source to the optical system in the subsequent chapter to address this weakness.

In this paper based thesis we reproduce in full the publication entitled "**Type- and Species-Selective Air Etching of Single-Walled Carbon Nanotubes Tracked with *in Situ* Raman Spectroscopy**", which is cited as ***ACS Nano* 2013, 7(8), Pages 6507-6521**. The supplementary information is also reproduced and can be found online at http://pubs.acs.org/doi/abs/10.1021/nn402412t .

Type- and Species-Selective Air Etching of Single-Walled Carbon Nanotubes Tracked with *in Situ* Raman Spectroscopy

Andrew Li-Pook-Than,[†,‡] Jacques Lefebvre,[†] and Paul Finnie[†,‡,*]

[†]National Research Council Canada, Building M-50, 1200 Montreal Road, Ottawa, ON, K1A 0R6, Canada and [‡]Department of Physics, University of Ottawa, 150 Louis Pasteur, Ottawa, ON, K1N 6N5, Canada. The manuscript was written through contributions of all authors. All authors have given approval to the final version of the manuscript. A.L. performed the experiments, P.F. and A.L. planned the experiments, and all authors contributed to the analysis of the data and the writing of the manuscript.

ABSTRACT The thermal oxidation of carbon nanotubes in air is investigated by *in situ* Raman spectroscopy. Etching rates are directly seen to be diameter, chirality, and type dependent. We directly track the evolution of bundled nanotube networks that undergo air etching from 300 to 600 °C. Some species are more robust than others. Changes to radial breathing mode (RBM) and G− peak structures suggest that metallic species etch away more rapidly, with smaller diameter semiconducting species etching more slowly and large diameter nanotubes, including semiconductors, etching last. The decay in integrated G and D band intensities is tracked and fit reasonably well with biexponential decay. The RBM evolution is better represented by a single exponential. All bands are fit to activation plots with RBMs showing significantly different rates.

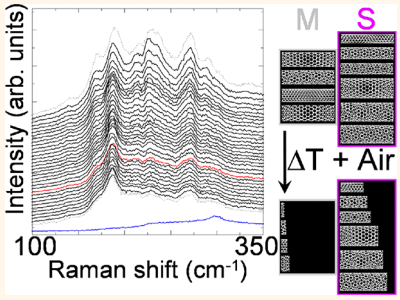

KEYWORDS: carbon nanotube combustion · air etching · *in situ* Raman spectroscopy · purification · chirality

Depending on the situation, the combustion of carbon nanotubes (CNTs) in air can be either detrimental or useful. In synthesis, it can inhibit or counteract growth, and in devices it can limit operating currents and temperatures. Controlled, it is a powerful chemical tool that plays a role in CNT characterization, structure modification, and purification.[1−7] There has recently been a resurgence of interest in the manipulation of nanotube populations *via* oxidation. In this work we will show evidence obtained by *in situ* Raman tracking that combustion is type selective, with potential applications for preparing semiconductor-rich nanotube ensembles. *In situ* Raman provides a unique window on the dynamics of the process, allowing one to track the evolution as it happens and observe trends that might be difficult to detect in static *ex situ* measurements.

Before discussing our experiments, we briefly review aspects of nanotube oxidation and purification. Oxidation is routinely used to characterize CNT purity. The mass and chemical characterization of CNTs and composite materials are commonly studied by techniques such as thermogravimetric analysis and differential thermal analysis, which can involve thermally oxidizing these samples in air.[4,8−12] It is also common to thermally oxidize CNT material in air or oxygen in order to remove defective carbon coatings, expose and/or remove catalyst particles following CNT synthesis, or otherwise modify non-CNT structures in the sample.[7,10,13−16] More generally, gas-phase oxides are frequently used to chemically alter the outcome of a number of CNT growth and separation practices.[13,14,17−23]

Perfect chirality control in nanotube synthesis has not been achieved. However, postprocessing separation and purification processes have been remarkably successful, encompassing an enormous variety of techniques of different yield and complexity.[24] Solution-based sorting is extensively studied, being potentially very high fidelity, relatively scalable, and inexpensive. However, such methods are not without weaknesses: they can be complicated and may be difficult to scale, and preparation of solutions typically damages nanotubes and coats them with difficult-to-remove adsorbates. Gas-phase selectivity would have some compelling advantages. It potentially would not leave residues and could potentially leave

* Address correspondence to paul.finnie@nrc-cnrc.gc.ca.

Received for review October 10, 2012 and accepted July 3, 2013.

Published online July 09, 2013
10.1021/nn402412t

nanotubes in a pristine state.[2,6] Recently there has been a resurgence of interest in oxidative etching and its selectivity, especially with respect to semiconducting or metal type.[25,26] Furthermore, there is an emerging consensus that etching plays a significant role in selectivity in synthesis, and efforts are being made to harness this.[22,27] So one motivation to explore gas-phase etching is that it can be naturally combined with chemical vapor deposition synthesis.

Air etching is very simple and scalable. However, as we will show, one drawback of air etching is that the selectivity that is presently achievable is relative and all CNTs are destroyed to some extent, such that a large initial mass is required. This is less of a problem now that high-yield synthesis is achievable. This method might one day allow sufficient nanotube separation for some applications. Furthermore, this drawback may not be important if etching is integrated with CVD synthesis.

Oxidation is well known to be effective at selectively burning off nongraphene nanocarbons and removing impurities while leaving behind sp^2 carbon. Reactivity reportedly increases going from graphite to well-graphitized amorphous carbon, to multiwalled CNTs, and then to single-walled CNTs (SWNTs).[8] Fullerenes are even more reactive than CNTs, which is attributed to higher surface curvature.[28] Defective sp^3-hybridized carbon is expected to etch faster than nondefective carbon.[8,29] Furthermore, compared to graphite, oxygen adsorbs onto and dopes carbon nanotubes more easily.[30−32] Osswald *et al.* found that disordered carbon removal by air oxidation was more complete in double-walled CNTs, compared to SWNTs.[33] The controlled oxidation of defective CNT walls has also been used to selectively remove layers from multiwalled CNTs and modify conductivity.[34]

There is already evidence that separation can be achieved by selective CNT destruction using various gas-phase oxidants, including air,[1,6] O_2 gas,[3−5,22,23] SO_3,[35] hydrogen plasma,[36] methane plasma,[37] water vapor,[27] and fluorine gas.[38] In all these studies, etching rates were found to increase with smaller CNT diameter (d_t), although these rates were also often found to be sensitive to CNT chirality. This diameter dependency, also observed in solution-phase oxidation studies,[39,40] is typically explained in terms of higher C−C bond strain, resulting in higher chemical reactivity with adsorbates.[1−6,35,37,38,41−43]

While bond strain does scale with diameter to a first approximation, it is the local curvature radius (LCR) that determines the weakest carbon−carbon bond and consequently is thought to be a limiting factor in oxidative etching.[1,44] LCR is chiral angle dependent and smallest for armchair tubes and largest for zigzags, with the result that armchairs should be least robust. This is despite an earlier study having ascribed faster etching to zigzag CNTs.[40] So, in terms of chirality, when etching with air, studies have found that etching rate scaled directly with higher chiral angle (θ) values and explained this in terms of LCR differences.[1,43−45] Miyata *et al.* have explicitly modeled this rate-determining process for chiral angle. These purely geometric arguments predict faster etch rates for small-diameter nanotubes and do not in themselves explain differences in electronic type, *e.g.*, differing etch rates for metallic CNTs (m-CNTs) and semiconducting CNTs (s-CNTs). Doping, however, is expected to be as significant a factor as chiral angle.[1,46] More generally, other studies have shown that chirality is expected to have a direct effect on oxygen sidewall chemisorption and can affect chemical reactivity in general.[47,48]

Depending on the etching gas and the particular treatment, there are already some reports indicating that m-CNTs may etch more rapidly with gas-phase oxidants than s-CNTs.[2,36−38,40,49] Using laser irradiation in air, Huang *et al.* observed both the preferential destruction of m-CNTs and high chiral angle s-CNTs.[50] Similar studies involving the light-induced selective attack of m-CNTs have also been reported.[51,52]

Very recently Lukaszczuk *et al.* claimed on the basis of absorption experiments and Raman data that metallic SWNTs can be selectively etched in open air, such that 95% semiconducting purity can be obtained.[25] Also very recently, Li *et al.* have reported that carbothermic oxidation of nanotubes, obtained by oxidizing nanotubes in air under a NiO layer, results in selective etching of metallic nanotubes.[26] These exciting new results with respect to type-selective oxidation reinforce the promise of such approaches and the value of *in situ* data.

Preferential m-CNT etching has been attributed to different mechanisms in various situations. One factor is the lower enthalpy of formation of semiconductors,[37,53] while another factor may be the presence of delocalized electronic states and separately the smaller ionization potential.[22,26,37,38] The presence of electronic states near the Fermi level for metals and the differences in work function[54,55] between semiconductors and metals are very important for the selectivity of chemical reactions.[26,55−57]

In other studies the opposite trend, with semiconductors being preferentially etched, has been observed, including those involving H_2O_2 as an oxidant.[2,35,40] Kawai *et al.* suggests that this might be due to the C−C bond weakening caused by hole doping.[44] Theoretically, density functional calculations have also suggested that CO_2 gas will preferentially etch non-armchair CNTs.[58]

In situ approaches are especially well suited to investigating such problems, as one can actually track the selectivity of the etching as it happens. Raman spectroscopy is solidly established as a tool that provides detailed information about all aspects of nanotubes and nanocarbon ensembles. In this work, as-grown CNT films on silicon are etched in air and dynamically

characterized using *in situ* Raman spectroscopy, a technique that has been used to monitor CNT growth at high temperature.[59−65] Here, samples are etched at temperatures between 300 and 600 °C, and dynamic changes to ~10 radial breathing mode (RBM) peaks, each corresponding to specific CNT diameter and chiralities, are tracked at all temperatures. The corresponding spectral evolution of the G and D bands is also tracked. At low temperatures, we validate the finding that metallic nanotubes etch faster, producing a semiconductor-enriched sample, and analyze the activation profiles of the G band, D band, and different semiconducting and metallic RBMs. A chirality/diameter (*n*,*m*) dependence also appears to be present, but we were unable to match the data to a single, simple relation with chiral angle. The etching dynamics and the Arrhenius plots of the various modes provide insight into the possible mechanisms of selectivity.

RESULTS AND DISCUSSION

Scanning electron microscope (SEM) images provide a general overview of the sample and the progress of etching. The same sample was imaged and etched in steps to evaluate the progress of etching (Figure 1). The technical details of the etching procedure are listed in the Methods section. Figure 1(a) shows an SEM image prior to etching. The CNTs form a tangled network of thick bundles, with most bundles less than 25 nm wide and occasional individual tubes or small bundles less than 5 nm wide. Essentially no individual SWNTs can be seen: all are bundled. Figure 1(b) shows an image after 30 min of etching at 425 °C. There are fewer stacks of bundles, and the network appears less dense. Individual bundle lengths appear similar, but the bundle thickness may be less uniform. Some bundles appear to be peeling off and forking into thinner bundles. Candidates for individualized SWNTs are visible (diameters <5 nm).

Figure 1(c) shows the corresponding image after a total of 90 min of etching at 425 °C. The surface density of nanotubes has decreased even more, and the bundles are thinner, though they remain present. The sidewalls of the forking bundles appear to be "frayed" and more uneven, while some bundles have been completely severed, although most bundle lengths remain the same. The silicon substrate surface, including the catalyst nanoparticles on the surface, is more exposed in Figure 1(b) than at earlier etching times such as Figure 1(a), where the mat of nanotubes obscures the catalyst nanoparticles. Higher accelerating voltage SEM images also show the presence of surface nanoparticles for all etching times, which would correspond to catalyst particles.

Thus, the overall effect of the air etch is to decrease the CNT film density and to attack along the entire length of the bundles, not only at the end of the bundles. A similar form of sidewall attack is described

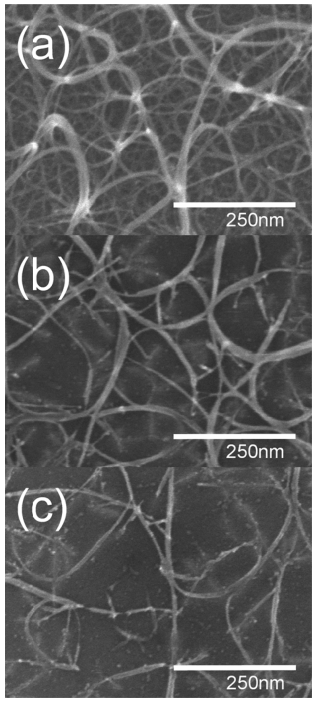

Figure 1. Scanning electron microscope micrographs of sample etched in air: (a) before etching, (b) after 30 min of etching, and (c) after 1 h 30 min of etching. The sample was etched at 425 °C.

by Miyata *et al.*, in which different barrier heights for C−C bond breaking during air combustion are found to be dependent on sidewall curvature.[1] Sidewall attack due to oxidation has also been described in a very recent transmission electron microscope (TEM) study.[66]

Transmission electron microscope images, including high-resolution TEM (HRTEM), of a typical pre-etch sample are included and discussed in the Supporting Information (SI), showing a similar configuration of primarily bundled nanotubes, with a smaller number of isolated SWNTs. From the TEM and SEM micrographs, we notice that the surface of the nanotube bundles appears to be relatively free of any large deposits of amorphous carbon. The HRTEM images reveal that bundles are very clean, and isolated SWNTs appear uncoated. There are certainly no large deposits of unstructured carbon; however, we cannot rule out the presence of intimately associated graphitic-like coatings, which are likely to be present at least to some extent.

In addition to TEM, X-ray photoelectron spectroscopy (XPS) was also performed to better characterize any non-nanotube carbon on pre-etch samples. A typical XPS spectrum is included in the SI. The asymmetric and narrow 1s C peak is essentially dominated by sp^2 carbon, consistent with the CNTs being relatively pristine and having very limited amounts of amorphous or defective carbon present.

The progress of the etching was tracked by *in situ* Raman spectroscopy. Figure 2 shows the *in situ* Raman

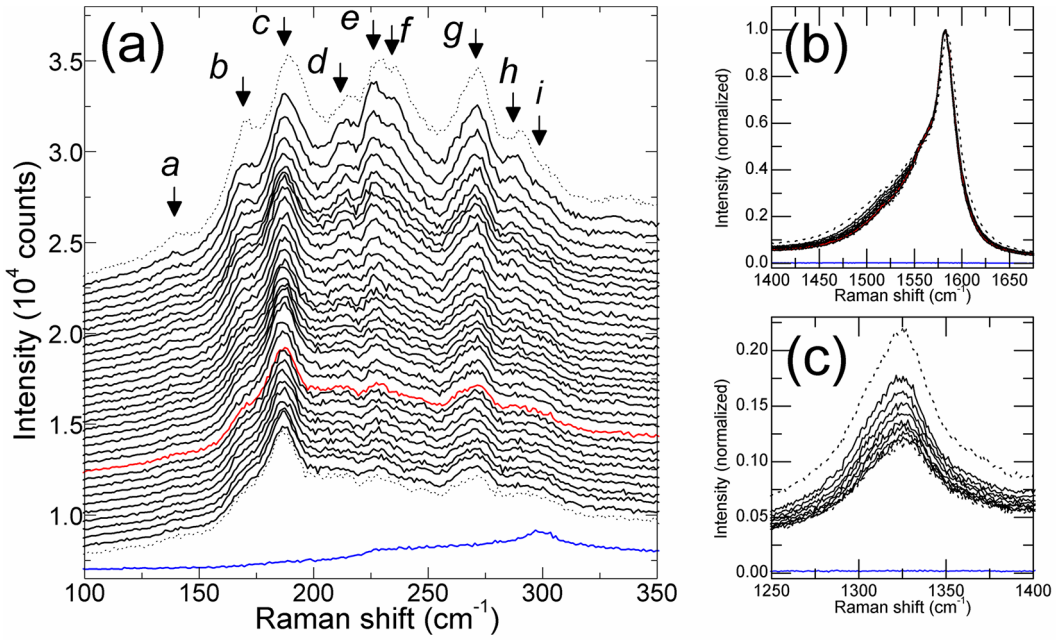

Figure 2. *In situ* **Raman spectra of a sample being etched at 350 °C, displayed chronologically from top to bottom. (a) Spectral changes in the RBM region. Spectra have been offset for clarity. Also shown are corresponding changes to (b) G and (c) D bands. These spectra are not offset. The top and bottom dotted spectra correspond respectively to pre- and post-etch spectra (after t = 132 min) for the sample. The corresponding Si/SiO_2 backgrounds are displayed in blue. In (a) spectra are shown every 4 min, from t = 4 min to t = 128 min, with air input occurring at t = 0 s (the original frames were taken with 5 s exposure every 10 s and then binned over 2 min). In (b) and (c) every spectrum is normalized to their maximum G band intensity. In (b) and (c), spectra are shown every 16 min, from t = 16 min to t = 128 min. The Raman excitation wavelength for all spectra was 532 nm.**

spectra of a typical sample etched at 350 °C. Figure 2(a) shows the spectral region of RBMs and their time evolution in 4 min intervals. The spectra are shown in chronological order, from top to bottom, with the top spectrum corresponding to conditions before air is first flowed into the reactor. In Figure 2(a) the spectra are slightly offset vertically to make tracking the RBMs easier. The most prominent RBMs appear to be visible on all samples both at room temperature and when heated. There are changes in peak intensity with heating, as expected due to the softening of the modes themselves, as well as the gradual shift in the energy of the resonant level that occurs when materials are heated. These RBMs experience an expected[67] frequency downshift of 3 cm^{-1} to 7 cm^{-1} with respect to their room-temperature frequencies when the given sample is heated from room temperature to temperatures between 300 and 600 °C.

We label nine of the most intense peaks in Figure 2(a), namely, the peaks centered at (*a*) 143 cm^{-1}, (*b*) 171 cm^{-1}, (*c*) 189 cm^{-1}, (*d*) 216 cm^{-1}, (*e*) 228 cm^{-1}, (*f*) 236 cm^{-1}, (*g*) 272 cm^{-1}, (*h*) 290 cm^{-1}, and (*i*) 303 cm^{-1}. On the basis of peak width and asymmetry, some of these peaks may represent more than one RBM.[68] For example, peak *c* contains at least RBMs at 187 and 189 cm^{-1}. The intensity of peak *a* is reduced due to a drop in the transmission caused by the optical setup at this and lower wavenumbers. All RBM peaks are superimposed on a distinctive silicon/silicon dioxide background signal (blue spectrum).

As discussed, early work indicates that smaller diameter nanotubes burn first, followed by large-diameter nanotubes.[39,41] Since the RBM frequency is nearly inversely proportional to diameter, RBM peaks at higher Raman shift are expected to burn before those at smaller RBM energies. This general trend does seem to be present in our data, with, for example, peak *i* etching faster than peak *c*. However, that is clearly only a rough approximation, and the true evolution is more subtle than just small diameter burning faster than large diameter.

Most notably, peak *c* remains resistant to etching compared to all other peaks. So, although a large proportion of the nanotubes are burned off (*i.e.*, ~55% of the G band intensity is lost), the residue is relatively "enriched" with the RBM *c* nanotubes after etching (*i.e* the relative intensity of RBM *c* has increased by more than twice when compared to total RBM intensity).

At the outset (t = 0 s) the relative intensities of peak *c* *versus* peaks *e* and *f* are comparable. However, by t = 92 min (red spectrum) peaks *e* and *f* can no longer be clearly distinguished, while peak *c* has undergone relatively less etching. Importantly, the larger diameter peak *b* also etches faster than peak *c*, with the peak *b* shoulder having almost vanished at this time as well, meaning that we have more than just diameter dependence. A more subtle change also occurs within the first 2 min of etching, such that the center of peak *c* moves from 189 cm^{-1} to 187 cm^{-1} and stays there

until etching is stopped, suggesting that two RBM populations with similar diameters can etch at substantially different rates.

Peak *g* similarly appears to resist etching compared to other peaks, albeit not as much as peak *c*. That is, prior to etching peak *g* is comparable in intensity to peak *c*, but after stopping the etching, peak *c* is at least twice the intensity of peak *g*. More generally, peaks *d* to *f* appear to etch faster than the smaller diameter peaks *g* to *i*, while both of these groups etch faster than peak *c*. Again, pure diameter dependence cannot explain this group behavior.

Assignment to chiralities can be performed with reference to a Kataura plot. Most of the pre-etch RBM peaks at room temperature remain clearly visible as the samples are heated to their etching temperatures, so despite changes to peak intensity and frequency, chiral assignments made at room temperature and etching temperatures are essentially the same.[67] For small-diameter nanotubes there are only a few possible chiralities, and above ~250 cm^{-1} a robust assignment is possible. At smaller Raman shifts the assignment can only be tentative. However, the peaks can be naturally grouped into semiconducting and metallic types; see SI for details. Qu *et al*. applied a similar grouping technique when analyzing the selective growth of s-CNTs *vs* plasma CVD.[69] From the SI it is very likely that peaks *g* to *i* correspond to semiconducting (E_{22}^{S} excitonic transition energy) species, with the most likely chiral assignments being *g* 272 cm^{-1} (8,4), *h* 290 cm^{-1} (9,2), and *i* 303 cm^{-1} (6,5). Peaks *d* to *f* correspond to metallic (E_{11}^{M}) species, with some possible chiral assignments being *d* 216 cm^{-1} (8,8), (12,3), or (13,1), *e* 228 cm^{-1} (9,6), and *f* 236 cm^{-1} (10,4). Peaks *b* and *c* correspond either to metallic (E_{11}^{M}) or semiconducting (E_{33}^{S}) species, and chiral assignments are uncertain because of the crowding of different possibilities in the Kataura plot. However, the resistant peak *c* could very well correspond to (16,0), a semiconducting zigzag species. The low-intensity peak *a* corresponds to a semiconducting species: (E_{33}^{S}) or (E_{44}^{S}). In terms of type, it is normal for a fixed wavelength slice of the Kataura plot to break down this way, with metallic peaks in the middle and semiconducting peaks on either side. This assignment suggests that the SWNT populations that etch the fastest correspond to metallic species.

Further information about the evolution of the ensemble comes from the G and D band evolution. Both bands decrease with time as material is etched away. Changes to the G and D bands for the sample etched at 350 °C are shown in Figure 2(b,c). Spectra are shown at 16 min intervals, and all spectra have been normalized to a peak G band intensity of unity.

The G band line shape contains information about diameter and metallicity (*i.e.*, semiconductor/metal ratios). The G band for a single nanotube is made up of a G+ at around 1590 cm^{-1} and the G− at smaller Raman shifts, and ensembles such as these are a superposition of many individual G+ and G− peaks. The G− peak position is diameter dependent and can be used in an analogous way as the RBM to determine diameter.[70,71] The further to the left the G− is, the smaller the CNT diameter. However, unlike the smaller energy RBM modes, the G− to G+ spacing depends on whether the tubes are metallic or not. For a fixed diameter, a metallic G− is approximately twice as far in energy from the G+ for a semiconductor.[71,72] A 1 nm diameter semiconducting nanotube has a G− at about 1550 cm^{-1},[70] whereas a metallic tube of the same diameter is at about 1510 cm^{-1}.[71,72] The resonance window for G bands is broader than for RBMs (about 300 meV compared to about 100 meV),[70] meaning that resonance conditions are not as strict for G bands.

The G+ band is the strongest peak in Figure 2(b), and normalized to its peak intensity, it appears to show essentially no change, apart from its initial 2 cm^{-1} downshift. The G−, on the other hand, changes significantly. In the G−, there is a gradual loss of intensity for small wavenumbers (below ~1555 cm^{-1}), suggesting a decrease in smaller diameter nanotubes. But this loss also indicates a change in metallicity. Importantly, below about 1490 cm^{-1} there is practically no contribution from semiconducting nanotubes, as they would be smaller than 0.5 nm in diameter and so would not be stable.[70,71] Therefore, any G− intensity to the left of this point can be attributed only to metallic nanotubes. There is a substantial loss of spectral intensity in this region. Furthermore, the decrease is relatively uniform from 1425 cm^{-1} to 1525 cm^{-1}. This suggests that the etching throughout this region is primarily metallic etching over a broad range of diameters.

The loss in G− broadness is consistent with the RBM region loss of peaks *e* and *f* if they are metallic peaks, as proposed. The loss in lower frequency G− peaks is also consistent with the initial loss of small-diameter nanotubes present in the RBM. The G− band evolution is an independent line of evidence that supports the contention that the air has preferentially etched metallic nanotubes. This is in contrast to the very recent selective oxidation report of Lukaszczuk *et al*., where there is little obvious change in the G− features.[25] The reason for the apparent lack of G band evolution in their work is not entirely clear; certainly the G band shape should change if the semiconductor to metallic ratios changes, provided both types are resonant. By contrast, studies involving the etching of m-SWNTs using microwave irradiation with mixed-acid-assisted dispersion[73] as well as fluorine gas[38] and oxygen gas[23] did show a significant change in G− structure, as expected. Also, unlike the work of Lukaszczuk *et al*., we never observe the reappearance of new small-diameter, semiconducting RBMs, an intriguing outcome of that work.

The D band gives information about the evolution of crystallinity and the degree of bundling. In Figure 2(c) the D band evolution is shown normalized to the G band peak intensity. Over the entire 132 min etching time, the D/G ratio drops by about a factor of 2, likely indicating that the crystallinity of the remaining nanotubes is higher than the starting material, as expected.[33] The time evolution of the D/G integrated peak intensity ratios for samples etched at different temperatures is given in the SI. Lower, improved D/G ratios can be obtained by etching the samples longer. For example, for the 350 °C sample, the initial D/G is *ca.* 0.12, and this value falls to D/G ≈ 0.08 when 50% of the carbon is etched, as estimated by the reduction in G band intensity.

In Figure 2(c) the D band is composed of at least two peaks centered at around 1324 and 1355 cm^{-1}. These likely correspond to bundled *versus* unbundled nanotube populations, respectively, although for isolated SWNTs the D band has been seen to be somewhat sensitive to CNT diameter.[74] Since the scaled D band line shape changed little over the course of the etching and shows only a gradual shift in spectral weight to small Raman shifts, this implies that the amount of bundling has not changed significantly and has probably not had a significant effect on D/G ratio.

A separate example of etching performed at a higher temperature, in which the sample is more completely etched, is shown in the SI. At late times even the etch-resistant bands are destroyed, which indicates that there is a compromise between selectivity and yield, and the best situation will be obtained at some intermediate amount of etching. However, because a more complete etching is achieved, the defect density is reduced significantly. The D/G ratio continues to drop below even 1% of its initial value, although the G band is still easily detectable. The G band line shape is indicative of large-diameter semiconducting nanotubes remaining at the end. Partial etching in this way is therefore usable to obtain highly defect free large-diameter SWNTs.

More generally, there appears to be little or no change in the amount of type selectivity or species selectivity over the range T = 300 to 400 °C, for a fixed amount of G band etching. Thus a wide temperature range is usable for this type of selectivity, with mainly the rate increasing as the temperature is increased. Above 400 °C, the evolution seems similar; however the changes take place too fast and our data were not good enough to determine convincingly whether or not the degree of selectivity had changed at these high temperatures.

Room-temperature Raman spectra provide another perspective on the changes caused by air etching. Figure 3 shows the room-temperature spectra of a sample that was etched at 550 °C, such that the pre-etch (black) and post-etch (red) spectra are displayed. A scaled-up version of the post-etch spectrum (green)

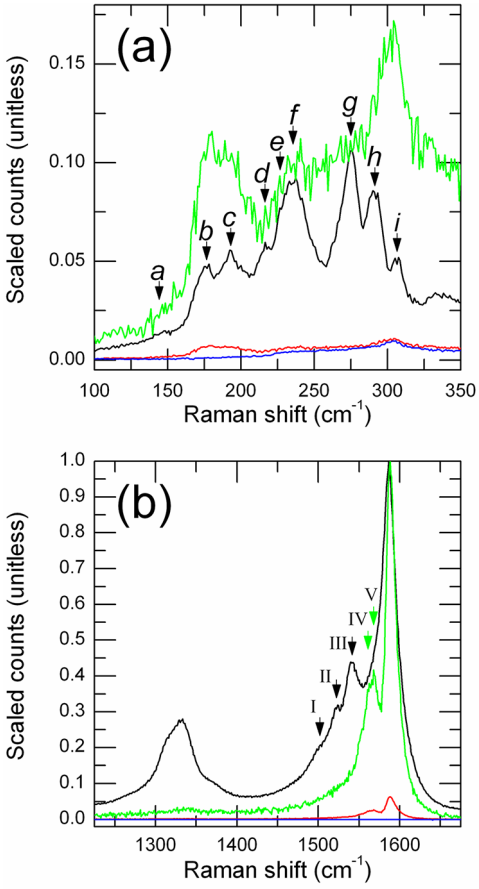

Figure 3. Room-temperature pre-etch Raman spectra (black), with corresponding post-etch (red) spectra and Si/SiO_2 background (blue). The (a) RBMs and (b) G and D bands are shown. The intensity is normalized so that the pre-etched maximum G band peak intensity is unity. The post-etch spectrum is also shown normalized to the post-etch G maximum (green). The peak on the blue, green, and red curves near 300 cm^{-1} is from the substrate. The sample was etched at 550 °C (with 6 × 5 s exposures).

is also shown, such that the G+ matches that of the pre-etch spectrum in order to contrast the change in G band structure. Prior to etching, most of the RBMs visible at high temperature remain visible at room temperature, although they are shifted and at different relative intensities. As indicated in Figure 3(a), we have *a* 145 cm^{-1}, *b* 177 cm^{-1}, *c* 192 cm^{-1}, *d* 217 cm^{-1}, *e* 230 cm^{-1}, *f* 236 cm^{-1} (possibly at 242 cm^{-1}), *g* 273 cm^{-1}, *h* 290 cm^{-1}, and *i* 307 cm^{-1}. After etching, only RBMs lower than 200 cm^{-1} (peaks *a*, *b*, and *c*) are still abundant. The peak at 300 cm^{-1} is substrate related. This sample was so completely etched that it is difficult to assess the selectivity from the RBM spectra. Here, the small-diameter semiconductors have been etched away along with the metallic nanotubes. Semiconducting nanotubes are still present, but they are at the same time large-diameter nanotubes.

The G band area in Figure 3(b) reveals more information. Initially, relatively distinct G− peaks can be identified at 1504, 1523, and 1540 cm^{-1}. The 1540 and 1523 cm^{-1}

peaks are probably semiconducting, while the 1504 cm^{-1} peak is probably metallic (see SI for details). More G− peaks are present but cannot be directly identified due to overlap. Below ~1500 cm^{-1}, however, this overlapping signal is due almost entirely to m-CNTs.[71] After etching, the three distinct peaks also entirely disappear, while a possible doublet peak composed of 1562 and 1570 cm^{-1} is revealed. These two peaks are very likely semiconducting and were obscured, presumably by large-diameter metallic G− peaks that have been etched away. They probably correspond respectively to the same species producing the RBM *c* and *b* peaks (see SI for more information). The loss in the overall Breit−Wigner−Fano (BWF) line shape, an asymmetric line shape thought to be characteristic of metallic nanotubes, is apparent. Here again the G− band evolution provides an independent line of evidence for metal-specific etching. The G+ peak also narrows from 3.2 meV to 1.8 meV (*i.e.*, full width at half-maximum), probably representing the narrowing distribution of nanotubes.

The D band intensity falls dramatically, with the D/G ratio falling from $I_D/I_G = 0.26$ to $I_D/I_G = 0.01$. This drop likely corresponds to the well-established and expected oxidation of defective and/or amorphous carbon and resulting improvement to CNT sample crystallinity.[25,33,61] The D band line shape before, during, and after etching is compared in the SI. Again, we observe no clear change in D band structure.

Exposing the samples to ambient air during the etching process is expected to p-dope the CNTs, so it is also important to distinguish which Raman spectral changes are due to doping and which are due to material loss *via* etching. In particular, oxygen gas and water vapor are known to affect the electrical characteristics of CNT devices, and the presence of oxygen gas has been used to tune the band gap of s-CNTs.[75] Additionally, if substantial doping does occur, we expect the Kohn anomaly resulting from electron−phonon coupling in m-CNTs to be affected.[76,77] Due to this effect, different levels of doping have been shown to change the G− width of m-CNTs, so it would be useful to distinguish whether the change in G− shape we observe is primarily due to this effect or preferential metallic destruction.

To determine the amount of doping occurring during exposure to air in our samples, we compare our spectra to the work of Kavan *et al.*, which shows how the typical electrochemical doping of both metallic and semiconducting CNTs causes the Raman intensities of RBMs and the G band to fall in intensity and shift.[78] Depending on the applied voltage, doping was found to either fill or deplete the peaks in the density of electronic states of s-CNTs and m-CNTs. Some irreversible oxidation was found to occur at large positive potential (>1.2 V), with the largest losses in G+ intensity accompanied by upshifts of up to ~20 cm^{-1} and RBM upshifts of up to ~5 cm^{-1}.[78]

In the present work, throughout all our etching temperatures, no substantial shifts to G+ frequency are shown to accompany G band intensity loss, such as in Figure 2(b). Likewise, no shifts to RBM frequencies were observed to occur simultaneously with falling RBM intensities. It therefore seems likely that the majority of the observed Raman intensity loss is due to nanotube destruction instead of doping effects, especially for small-diameter RBMs.

It is also notable that, at low etching temperatures ($T < 400$ °C), the intensity drop can occur over a period of several hours. Unless there is a high barrier for the doping, which would not be the case if it requires only physisorption, for example, one might expect the time scale of doping to be much faster. We do observe a very small, 1−2 cm^{-1} downshift of some RBMs immediately after exposure to air, and this could be doping related; but this change occurs during the first seconds of a run and is unrelated to the large drops in Raman intensity during etching. Additionally, given the unambiguous loss in BWF character after etching, accompanying loss in G+ intensity and the fact that we start with a significant amount of s-CNTs prior to etching, it seems unlikely that line width changes can be explained by doping.

We attempted to explore type and chiral selectivity using *ex situ* multiwavelength Raman at 514, 633, and 785 nm for the 400 °C etched sample, before and after etching. The data are not obtained *in situ* and come from different areas of the same sample. We only have a snapshot at some location after a fixed amount of etching. Definitive (*n*,*m*) assignment of the RBMs remains difficult, although a larger population of CNTs resonant at different wavelengths is examined. Effects beyond diameter, presumably related to chiral angle, are blatant, with several examples of close neighbors in diameter etching at different rates. However semiconductor *versus* metal type selectivity proved difficult to verify, mainly because the resonant nanotubes at 633 and 785 nm turned out to be primarily semiconducting to begin with, but there are some specific examples of faster etch rates for peaks that could be tentatively assigned to metallic peaks. A detailed discussion is included in the SI. Here we provide a brief summary with respect to type selectivity.

The results at 514 nm were for the most part similar to 532 nm. At 514 nm (see SI), RBM *g* is probably semiconducting, and peaks *h* to *k* are probably metallic. Since it is a larger diameter, the relative robustness of peak *g* might be consistent with semiconductors resisting etching more than metallic. The G− line shape loses its metallic BWF line shape and appears more semiconducting. Finally the 2D band, which is initially split into two peaks, retains only the large-frequency peak. This could have various causes, but speculatively might be because a metallic 2D peak is lost or due to the loss of certain CNT diameters.

Interestingly, RBM *i* resists etching, yet our most likely assignment for it is metallic. A possible assignment for this peak is to the (8,8) species, despite armchair nanotubes being expected to etch rapidly.[45]

At 633 nm (see SI) RBM *e* is more resistant to etching than RBMs *c* and *d*, despite being a smaller diameter nanotube. This might be because *e* is semiconducting, and a reasonable assignment is that *c* and *d* are metallic. Chiral angle dependent rates are clear because *g*, *h*, and *i* are very close in diameter (and Raman shift), yet *h* etches slowly, while *g* and *i* etch quickly. Changes to the semiconducting/metal character of the G− are not clearly visible here at 633 nm.

At 785 nm (see SI), RBM *d* is a semiconducting nanotube and is quite resistant to etching. Some RBM peaks appear to etch faster and can be assigned to metallic tubes, but there are also possible semiconductor assignments as well. After etching, the G− band is characteristic mainly of large-diameter semiconductors and arguably may have lost some metallic character, but this change, if real, is subtle at best. We conclude that the *ex situ* measurements do not disagree with the *in situ* data, but nor do they demonstrate clear type selectivity.

The *in situ* data also allow us to explore the dynamics of etching, and this was also characterized by extracting the integrated intensities of *in situ* Raman bands as a function of time for various temperatures. A challenge for such measurements is background subtraction, which can be a large source of error in the evolution curves. For background subtraction, we employed a simple trapezoidal background correction algorithm, described in previous work[65] and illustrated in the SI. As described above the integrated intensities were further normalized against the first-order Si band to compensate for any drift in illumination intensity or collection efficiency. This is a good approach as long as the film is very transparent. In Figure 4, the G (consisting of both G+ and G−) and D band evolution is presented with the integrated intensity normalized so that its initial intensity is unity. The change in resonance window for 300 °C is small ($k_BT \approx 0.03$ eV) and comparable to a 6 nm decrease in incident wavelength.

We also analyzed RBMs in this way, and the results are broadly consistent with the preferential etching of metallic nanotubes, but the background subtraction for RBMs is much less robust than for G and D bands because of the uneven background in the RBM spectral range (see SI). This means that the quantitative evolution of the extracted intensities faithfully represents the G and D bands, but is less certain for the RBM bands. The trends in the evolution curves with temperature are smoothly varying. We note that one curve does not fit perfectly in Figure 4, namely, the sample etched at 500 °C (open squares). This is because this sample was grown in a different batch of samples with

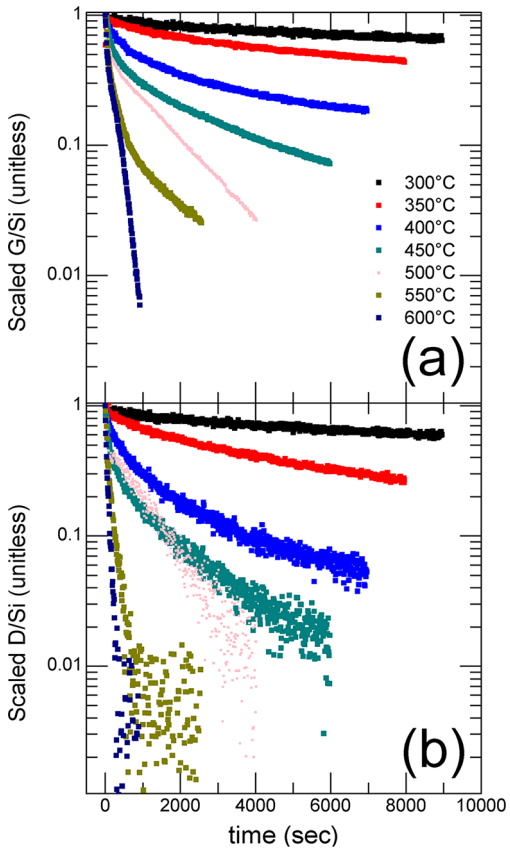

Figure 4. Time evolution plots of the integrated Raman intensities for the (a) G band and (b) D band at different etching temperatures. The samples are etched at 50 °C increments from 300 °C (top) to 600 °C (bottom). The 500 °C sample had a lower pre-etch I_D/I_G ratio. Spectra have been scaled with respect to the first-order Si intensity of the substrate in order to reduce the effect of mechanical drift on the Raman signal and normalized to 1 at $t = 0$.

a somewhat lower starting D/G ratio and different starting RBM intensities than the other samples, which affected the evolution at late times. Despite this different initial state, it does fit the general trend very well at early times.

Across all temperatures, D band etching occurred more rapidly than G band etching, and as expected, all etching rates increase with temperature.

None of the G band and D band evolution curves could be fit with a single-exponential decay function. There are at least two etching phases in each curve. Therefore, as shown in Figure 5(a) for the $T = 450$ °C etch, biexponential decay (light gray) does fit reasonably well. One fast (wine) and one slow (violet) exponential function are fit, such that the scaled intensity $I(t)$ is $I(t) = I_{fast} + I_{slow} = A_{fast}\exp(-t/\tau_{fast}) + A_{slow}\exp(-t/\tau_{slow})$, where A_{fast} and A_{slow} are proportionality constants, τ_{fast} and τ_{slow} are time constants, and t is the time elapsed from when air input begins. For the $T = 300$ to 600 °C samples, τ_{slow} varied from 16 900 s to 250 s and τ_{fast} varied from 1200 s to 35 s for the G bands. For some etching temperatures, the fast etching phase may actually contain more than one exponential, so the biexponential fit is only an

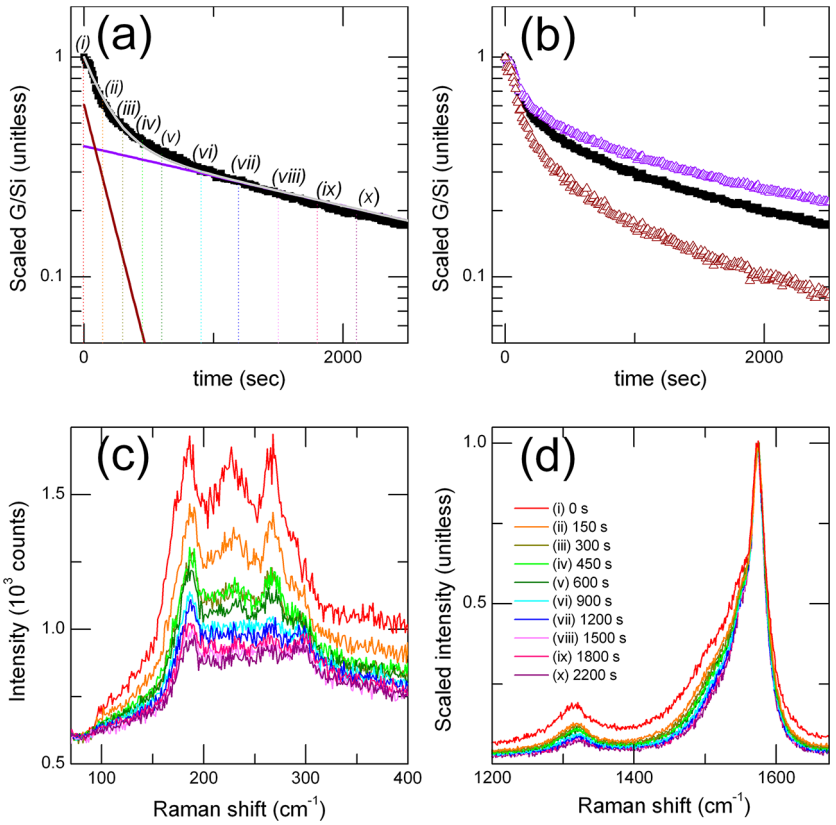

Figure 5. (a) Typical biexponential fit (light gray) of the G band signal (black, normalized to the Si intensity) for the 450 °C etched sample. Slow (violet) and fast (wine) decay components are indicated. The respective time scales for the slow and fast components are $\tau = 3203 \pm 25$ s and $\tau = 188 \pm 3$ s. (b) Comparison of G band decay: Total G band signal (black) *versus* metallic G− signal (wine, from 1456 to 1476 cm^{-1}) and G+ signal (violet, from 1565 to 1585 cm^{-1}) for the 450 °C etched sample. Corresponding (c) RBM and (d) D and G spectra for each of the 10 etching times shown in (a).

approximation, although for other temperatures the fit was excellent. Also, for comparison with total G band evolution, Figure 5(b) shows the evolution of the low-frequency, metallic G− peaks from 1456 to 1476 cm^{-1} (wine triangles) and that of the G+ peak from 1565 to 1585 cm^{-1} (violet triangles). As expected, the metallic peaks decay more rapidly.

There is some evidence that the fast and slow components represent different nanotube populations. Spectrally, as seen in Figure 5(b) and (c), by the time when I_{fast} drops close to 0 (*i.e.*, at point (vi)), in all samples, RBM *c* is the dominant peak and, assuming that G band contribution from non-CNT sources at this stage of the etch is low, I_{slow} at least roughly tracks the decay of RBM *c*. After I_{fast} drops close to 0, the G line shape appears much more stable, indicating that the majority of metal etching has already occurred during this first etching stage. It follows that the amount of metal/semiconductor etching can be optimized by stopping air input at different times. Roughly speaking, one can conclude that the fast component corresponds to the phase when the G band narrows most, and many species are selectively lost in the RBM region, while the slow component corresponds to the phase when the remaining G band and RBM band intensities simply decrease uniformly.

Our samples are highly bundled, so we should consider what effect bundling has on the kinetic Raman spectra and the observed fast and slow components. While the fraying of bundles observed in SEM may indicate that air is still efficiently getting to the core of the bundles, it is still possible that outer CNTs will etch before the inner CNTs and protect them to a degree. In CVD growth, the *a priori* expectation is that chirality, diameter, and metallicity of individual CNTs are randomly distributed within the bundle, with bundle formation occurring well after CNT nucleation. It is therefore unlikely that distinct inner and outer CNT groups within a bundle are directly responsible for the fast and slow components. This random CNT distribution within the sample should actually decrease the amount of etching selectivity, since some portion of the protected inner CNTs would consist of otherwise etch-susceptible species. More generally, CNT bundles and surface CNTs are not well organized on the substrate. So, the chirality and type dependence of etching should be enhanced for debundled and individualized nanotubes.

Debundling caused by etching may directly impact the resonance windows of different CNTs. Additionally, bundle thickness is expected to affect overall G bandwidth.[79] However, at all etching temperatures,

we do not see any significant shift in the RBM, G−, or G+ frequencies, which would indicate that a significant change to strain induced by debundling has occurred.[80] If anything, based on the aforementioned SEM images in Figure 1 and lack of D band shift, there appears to be minimal debundling, and few individual CNTs are visible once the fast component has fallen to zero and selective etching has already occurred.

One complication in trying to understand the time evolution is that at high temperatures the etch rate becomes so fast that it is no longer possible to ignore the time it takes to change over the gas composition from reducing to oxidizing. The chamber has an internal volume of ~29 cm^3, and the supply lines have a volume of ~4 cm^3. The air is introduced at a flow rate of 16 sccm, meaning it should take a time scale on the order of 90 s to turn over the gas composition. Such effects do not explain the biexponential, however, as they should be negligible at low temperatures because of the slow etch rate. Furthermore, one would expect the presence of the purge gas transient to decrease the etching rate, instead of increasing it, as observed here. However, for the fastest etching rates, it is clear that one has to view the gas concentration as ramping up during the etch. For the highest temperatures, it is not a good approximation to view the gas concentrations as static.

Since the $1/\tau$ values are simply rates, the temperature dependence of these etch rates can be plotted in an activation plot as shown in Figure 6. The slow (black squares) and fast (red squares) G band etch rates are activated with energies 0.67 ± 0.05 and 0.50 ± 0.12 eV, respectively. That is, given the large uncertainty they are barely distinguishable, if at all, in activation energy. The slow (blue triangles) and fast (green triangles) D band etch rates are activated with energies of 0.79 ± 0.13 and 0.58 ± 0.13 eV, respectively. Given the large uncertainty, these too cannot be meaningfully distinguished. These energies are of the same order of magnitude for activation energies obtained in studies involving the etching of graphitic carbon.[8,29] If the fast and slow modes correspond to different populations, the difference in etching activation energy for these populations was too small to measure in our experiment.

As described in the SI, as an alternative to fitting biexponentials for the entire duration of the G and D band evolutions, one exponential could be fit at early times and one exponential could be fit at late times. Using this method, activation plots for the fast and slow phases for the G and D bands were also obtained. These energies are similar to the results obtained from the biexponential fits, indicating that the biexponential function reasonably approximates G and D evolution.

It is possible to extract and analyze certain RBM evolution curves and extract different activation energies, similar to what was accomplished for the G and D bands in Figures 5 and 6. Depending on RBM peak

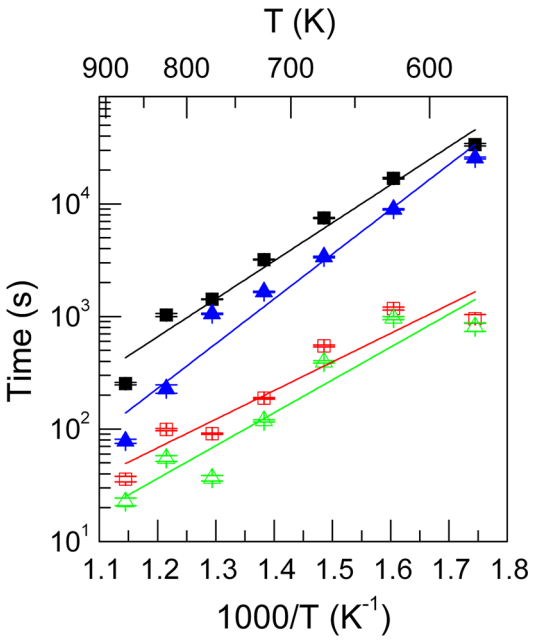

Figure 6. Activation plots for the G band slow (black square) and fast (red square) τ values and for the D band slow (blue triangle) and fast (green triangle) τ values. Activation energies are taken from the slopes of the four linear fits (lines) and are listed in the main text.

intensity, spectral background intensity, and etching rate, it was not possible to obtain evolution curves for all RBMs. However, curves from peaks *b*, *c*, *e*, *f*, and *g* identified in Figure 2 could be tracked over a variety of temperatures, with Figure 7(a) displaying the 350 °C etching case. Due to overlap, the intensities of peaks *e* and *f* were combined. Unlike the G and D bands, all the RBM curves can be roughly fit with a single-exponential function, with the assigned metallic *e* and *f* peaks (blue) etching rapidly and peak *c* (red) being the most resistant. Keeping in mind that the resonance window of the G band is larger than that of the RBMs, slow G band decay generally corresponds well with the decay of peak *c*, while fast G band decay may correspond with the averaged decay of the remaining RBM peak populations.

Some RBM-activated plots are shown in Figure 7(b). Note that due to the large signal-to-noise ratios of the RBMs, the energy uncertainties are larger than those of the G and D bands. The energies for peaks *b*, *c*, and *g* and the combined peaks *e* and *f* are respectively found to be 1.19 ± 0.69, 0.99 ± 0.23, 0.78 ± 0.20, and 0.72 ± 0.20 eV. Therefore, while the energies for the larger diameter peaks *b* and *c* may be larger than those of the other RBMs, the RBM energies cannot be meaningfully distinguished from each other or from the energies of the G and D bands, despite the substantially different etching rates of different RBMs.

This raises an interesting point about the mechanism of selectivity. One model is that selectivity in oxidation rates arises from different activation barriers. This may be true in some cases, and we may simply lack the energy resolution in the current experiment.

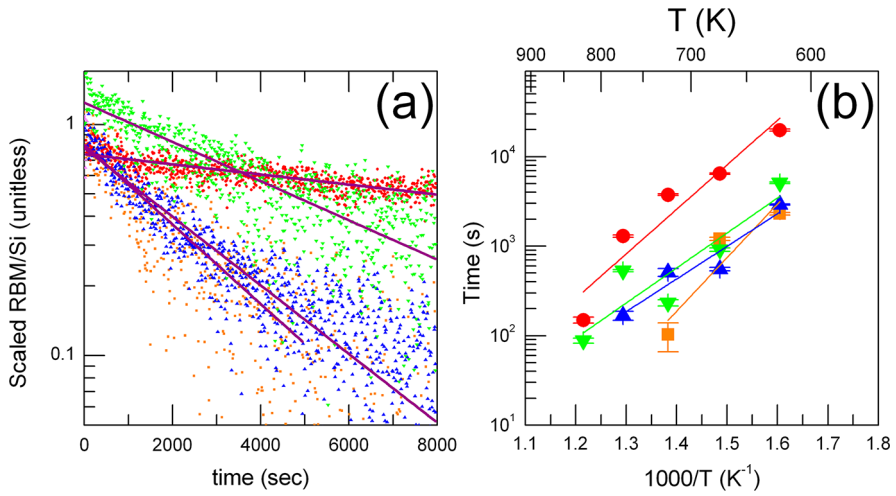

Figure 7. (a) Typical exponential fits (violet lines) of RBM band signals during etching at 350 °C. RBMs at 177 cm^{-1} ("peak *b*", orange), 192 cm^{-1} ("peak *c*", red), and 273 cm^{-1} ("peak *g*", green) are shown. The intensities of the RBM signals at 230 and 236 cm^{-1} ("peaks *e* and *f*", blue) have been combined. All signals are scaled to the Si intensity and normalized to 1 at $t = 0$. (b) Activation plots for the four RBM groups identified in part (a). Activation energies are listed in the main text.

However, this does not explain peak *c* in Figure 7, which etches much more slowly despite having a similar activation energy to the others. So at least in this case, this is evidence that selectivity is determined by the prefactor in the Arrhenius equation and not the activation energy factor.

One interpretation may be that fast etching nanotubes, which we suppose are metallic here, effectively have a higher molecular collision rate. Speculatively, this might be explained by the relative delocalization of metallic electrons on m-CNTs[81] or possibly by the higher polarizability of m-CNTs, which increases the magnitude of van der Waals interactions,[82] resulting in a larger effective cross-section. Another possibility is that metallic species are more sensitive to defects formed during growth, resulting in greater reactivity.[83,84]

Mechanisms of selectivity related to the electronic density of states near the Fermi level for m-CNTs are also often used to explain enhanced metallic etch rate.[22,38,85] For example, An *et al*. have attributed the selective reactivity of diazonium reagents with m-CNTs to the stabilization of a charge-transfer complex formed at the metallic density of states.[82,83] Likewise, the preferential etching of m-CNTs with methanol has been linked to the lower ionization potential of m-CNTs.[86] Independent density functional theory calculations have shown that semiconducting single-walled nanotubes have a lower heat of formation,[53] while unique impurity states near the Fermi level of m-CNTs act as a strong scattering center,[87] both of which result in m-CNTs being more reactive than s-CNTs.[37] Additionally, it is known that the atmospheric oxygen and water can cause charge transfer and trapping, which can affect the behavior of s-CNT and m-CNT devices differently.[75]

It is important to note that our samples have cobalt catalyst present. Cobalt oxides might also play a similar role to the nickel oxides in the carbothermic reaction very recently reported by Li *et al*., and the mechanism of selectivity may be similar in that case.[26] Catalyst particle shape[88] and catalyst reduction potential[26,27,89] may be important factors.

Recently there has been discussion that growth rates might be proportional to chiral angle.[60,90] If that were true, one might imagine that etch rates could also be proportional to chiral angle, and there is evidence for such scaling in air etching studies.[1,50] Note that this is a different argument than the local curvature radius limiting etch rates, which implies a specific, but different chiral angle dependence. The argument for growth rates proportional to chiral angle hinges on the graphene edge step density scaling with chiral angle. In etching this would be relevant if it took place from the end only. Very recent observations of oxidation in aberration-corrected environmental transmission electron microscopy show, however, that etching proceeds by attacking sidewalls more commonly.[66] Although oxidation is in some ways the opposite of growth, it would appear that the time reverse of the growth model does not match the oxidation dynamics, at least in our case.

The local curvature radius model might explain some of the data. Here, there are a large range of chiral angles visible in the RBM and/or G− spectra. However, we do not generally observe large variations in etch rate due to chiral angles when we make a tentative assignment. For example, large and small chiral angles are present in RBMs *g* to *i*, but we do not observe any large difference in etching behavior within this group (see SI). Bundling, too, may be a factor here, since the inner nanotubes are protected from gas exposure to at least some extent, which would weaken any specific chirality dependence. If that is the case, one should expect better selectivity from more debundled samples.

In general, assigning chiralities to large-diameter nanotubes *via* Raman spectroscopy is prone to error. It is possible that the etch-resistant RBM *c* corresponds to the semiconducting zigzag (16,0) species. This assignment would be compatible with a chiral angle determining the etch rate. However, there are many equally plausible assignments for that peak. Moreover, other near-zigzag peaks at small diameter can be assigned, and they do not show significantly slower etch rates. Therefore, we could not find clear evidence of the simple chiral angle rate dependence suggested by the local curvature model. If there is a simple chiral angle dependency, it is perhaps masked by semiconductor/metal type dependences and by bundling. Certainly, however, the trend of small-diameter nanotubes being etched first is clear.

CONCLUSIONS

To summarize, our *in situ* Raman spectroscopy generally supports the idea that etch rates are faster for small-diameter nanotubes. However this is only the beginning of the story. Subsets of the population persist longer than other species. Chiral angle effects are clearly present, but there is also evidence for type dependence. In particular, the *in situ* data are consistent with m-CNTs etching more rapidly than s-CNTs, and this is manifested in a biexponential of G band intensity. Extracted activation energies appear largely independent of tube chirality, leading to the conclusion that differences in etch rates are predominantly determined by other factors such as cross-section.

This selective etching approach, while suffering from the drawback of destroying a lot of material, is very simple and scalable and would be particularly interesting to integrate with gas-phase synthesis. With further study, it could have the potential to be used as a tool to produce semiconductor-enriched samples, while improving crystallinity. *In situ* tools such as *in situ* Raman can help test the mechanism of selectivity and help to optimize selectivity.

METHODS

Etching was tracked by *in situ* Raman spectroscopy as follows: samples, consisting of chemical vapor deposition produced nanotubes grown from cobalt thin film catalyst on thermally oxidized silicon wafers, were cleaved into 3 mm × 3 mm square pieces and loaded into a miniature hot-walled chemical reactor (Linkam CCR1000). A custom-built Raman spectroscopy system was used to monitor the sample *in situ* as described in previous work.[65,91] The reactor was purged in 2% H_2/Ar at 16 sccm and heated to a fixed temperature between 300 and 600 °C. Etching was initiated by pumping ambient room air with a diaphragm pump into the reactor at a flow rate of 16 sccm, and air flow was maintained for a matter of minutes or hours, depending on the etch rate. After etching, the reactor was again purged with H_2/Ar at 16 sccm and cooled to room temperature.

Raman spectroscopy was performed on all samples before, during, and after etching, always using the 532 nm laser line. Focusing conditions are important. To avoid laser heating the beam was defocused to a narrow elliptical spot roughly ∼50 μm long and ∼5 μm wide, with incident power ∼1 mW using a 50× long working distance objective. A spatially extended spot provides a stronger Raman signal than would be obtained from a point, while minimizing local heating. Given the lack of a noticeable frequency shift of the Raman first-order Si band and the carbon-related bands, local sample heating due to the laser is estimated to be less than ∼25 °C. Second, small spatial drifts in the *z* (focusing) direction can cause large drifts in the collection efficiency, and so cause artifacts in the evolution profile. To compensate, we used a separate imaging arm[63,65] built into our Raman system. This arm was used to continually refocus the laser spot between acquisitions of spectra to compensate for any drift. Furthermore, the nanotube layer was thin enough to be transparent, and we normalize the nanotube-related bands to the substrate silicon first-order band to cancel out small drifts. The result was that very smooth and reproducible evolution curves could be extracted.

Conflict of Interest: The authors declare no competing financial interest.

Supporting Information Available: Diameter and chirality assignment for radial breathing mode and G− peaks. Raman spectra of sample etched at T = 600 °C. Radial breathing mode time evolution plots. D/G ratio time evolution plots. Alternative G and D band activation plots. TEM images at low and high resolution of pre-etch material. Multiwavelength Raman spectra of sample etched at T = 400 °C. Background correction illustration. Comparison of D band line shape for sample etched at T = 550 °C. XPS spectra of pre-etch material. This material is available free of charge *via* the Internet at http://pubs.acs.org.

Acknowledgment. This work was supported by a Discovery Grant (P.F., A.L.) from the Natural Sciences and Engineering Research Council of Canada (NSERC) and a grant (A.L.) from Le Fonds de Recherche du Québec—Nature et Technologies (FRQNT). We are grateful for the assistance of Paul Marshall, Phillip Vinten, Hue Tran, Chris Kingston, and Xiaohua Wu for TEM data, Martin Couillard for HRTEM data, and Oltion Kodra for XPS data.

REFERENCES AND NOTES

1. Miyata, Y.; Kawai, T.; Miyamoto, Y.; Yanagi, K.; Maniwa, Y.; Kataura, H. Chirality-Dependent Combustion of Single-Walled Carbon Nanotubes. *J. Phys. Chem. C* **2007**, *111*, 9671–9677.
2. Hodge, S. A.; Bayazit, M. K.; Coleman, K. S.; Shaffer, M. S. P. Unweaving the Rainbow: A Review of the Relationship between Single-Walled Carbon Nanotube Molecular Structures and their Chemical Reactivity. *Chem. Soc. Rev.* **2012**, *41*, 4409–4429.
3. Borowiak-Palen, E.; Pichler, T.; Liu, X.; Knupfer, M.; Graff, A.; Jost, O.; Pompe, W.; Kalenczuk, R. J.; Fink, J. Reduced Diameter Distribution of Single-Wall Carbon Nanotubes by Selective Oxidation. *Chem. Phys. Lett.* **2002**, *363*, 567–572.
4. Chiang, I. W.; Brinson, B. E.; Huang, A. Y.; Willis, P. A.; Bronikowski, M. J.; Margrave, J. L.; Smalley, R. E.; Hauge, R. H. Purification and Characterization of Single-Wall Carbon Nanotubes (SWNTs) Obtained from the Gas-Phase Decomposition of CO (HiPco Process). *J. Phys. Chem. B* **2001**, *105*, 8297–8301.
5. Nagasawa, S.; Yudasaka, M.; Hirahara, K.; Ichihashi, T.; Iijima, S. Effect of Oxidation on Single-Wall Carbon Nanotubes. *Chem. Phys. Lett.* **2000**, *328*, 374–380.
6. Wiltshire, J. G.; Khlobystov, A. N.; Li, L. J.; Lyapin, S. G.; Briggs, G. A. D.; Nicholas, R. J. Comparative Studies on Acid and Thermal Based Selective Purification of HiPCO Produced Single-Walled Carbon Nanotubes. *Chem. Phys. Lett.* **2004**, *386*, 239–243.

7. Balasubramanian, K.; Burghard, M. Chemically Functionalized Carbon Nanotubes. *Small* **2005**, *1*, 180–192.
8. Brukh, R.; Mitra, S. Kinetics of Carbon Nanotube Oxidation. *J. Mater. Chem.* **2007**, *17*, 619–623.
9. Bom, D.; Andrews, R.; Jacques, D.; Anthony, J.; Chen, B.; Meier, M. S.; Selegue, J. P. Thermogravimetric Analysis of the Oxidation of Multiwalled Carbon Nanotubes: Evidence for the Role of Defect Sites in Carbon Nanotube Chemistry. *Nano Lett.* **2002**, *2*, 615–619.
10. Dillon, A. C.; Gennett, T.; Jones, K. M.; Alleman, J. L.; Parilla, P. A.; Heben, M. J. A Simple and Complete Purification of Single-Walled Carbon Nanotube Materials. *Adv. Mater.* **1999**, *11*, 1354–1358.
11. Yang, S.; Rafael Castilleja, J.; Barrera, E. V.; Lozano, K. Thermal Analysis of an Acrylonitrile-Butadiene-Styrene/SWNT Composite. *Polym. Degrad. Stab.* **2004**, *83*, 383–388.
12. Arepalli, S.; Nikolaev, P.; Gorelik, O.; Hadjiev, V. G.; Holmes, W.; Files, B.; Yowell, L. Protocol for the Characterization of Single-Wall Carbon Nanotube Material Quality. *Carbon* **2004**, *42*, 1783–1791.
13. Futaba, D. N.; Hata, K.; Yamada, T.; Mizuno, K.; Yumura, M.; Iijima, S. Kinetics of Water-Assisted Single-Walled Carbon Nanotube Synthesis Revealed by a Time-Evolution Analysis. *Phys. Rev. Lett.* **2005**, *95*, 056104.
14. Magrez, A.; Seo, J. W.; Kuznetsov, V. L.; Forro, L. Evidence of an Equimolar C_2H_2-CO_2 Reaction in the Synthesis of Carbon Nanotubes. *Angew. Chem.* **2007**, *119*, 445–448.
15. Zhang, G.; Mann, D.; Zhang, L.; Javey, A.; Li, Y.; Yenilmez, E.; Wang, Q.; McVittie, J. P.; Nishi, Y.; Gibbons, J.; *et al*. Ultra-High-Yield Growth of Vertical Single-Walled Carbon Nanotubes: Hidden Roles of Hydrogen and Oxygen. *Proc. Natl. Acad. Sci. U.S.A.* **2005**, *102*, 16141–16145.
16. Xu, Y.; Peng, H.; Hauge, R. H.; Smalley, R. E. Controlled Multistep Purification of Single-Walled Carbon Nanotubes. *Nano Lett.* **2005**, *5*, 163–168.
17. Nikolaev, P.; Bronikowski, M. J.; Bradley, R. K.; Rohmund, F.; Colbert, D. T.; Smith, K. A.; Smalley, R. E. Gas-Phase Catalytic Growth of Single-Walled Carbon Nanotubes from Carbon Monoxide. *Chem. Phys. Lett.* **1999**, *313*, 91–97.
18. Nasibulin, A. G.; Brown, D. P.; Queipo, P.; Gonzalez, D.; Jiang, H.; Kauppinen, E. I. An Essential Role of CO_2 and H_2O during Single-Walled CNT Synthesis from Carbon Monoxide. *Chem. Phys. Lett.* **2006**, *417*, 179–184.
19. Huang, J.; Zhang, Q.; Zhao, M.; Wei, F. The Release of Free Standing Vertically-Aligned Carbon Nanotube Arrays from a Substrate Using CO_2 Oxidation. *Carbon* **2010**, *48*, 1441–1450.
20. Corthals, S.; Van Noyen, J.; Geboers, J.; Vosch, T.; Liang, D.; Ke, X.; Hofkens, J.; Van Tendeloo, G.; Jacobs, P.; Sels, B. The Beneficial Effect of CO_2 in the Low Temperature Synthesis of High Quality Carbon Nanofibers and Thin Multiwalled Carbon Nanotubes from CH_4 Over Ni Catalysts. *Carbon* **2012**, *50*, 372–384.
21. Chen, Z.; Ziegler, K. J.; Shaver, J.; Hauge, R. H.; Smalley, R. E. Cutting of Single-Walled Carbon Nanotubes by Ozonolysis. *J. Phys. Chem. B* **2006**, *110*, 11624–11627.
22. Yu, B.; Liu, C.; Hou, P.; Tian, Y.; Li, S.; Liu, B.; Li, F.; Kauppinen, E. I.; Cheng, H. Bulk Synthesis of Large Diameter Semiconducting Single-Walled Carbon Nanotubes by Oxygen-Assisted Floating Catalyst Chemical Vapor Deposition. *J. Am. Chem. Soc.* **2011**, *133*, 5232–5235.
23. Yu, B.; Hou, P.; Li, F.; Liu, B.; Liu, C.; Cheng, H. Selective Removal of Metallic Single-Walled Carbon Nanotubes by Combined *in Situ* and Post-Synthesis Oxidation. *Carbon* **2010**, *48*, 2941–2947.
24. Hersam, M. C. Progress Towards Monodisperse Single-Walled Carbon Nanotubes. *Nat. Nanotechnol.* **2008**, *3*, 387–394.
25. Lukaszczuk, P.; Mijowska, E.; Kalenczuk, R. Selective Oxidation of Metallic Single-Walled Carbon Nanotubes. *Chem. Pap.* **2013**, *10*), 1–5.
26. Li, S.; Liu, C.; Hou, P.; Sun, D.; Cheng, H. Enrichment of Semiconducting Single-Walled Carbon Nanotubes by Carbothermic Reaction for Use in All-Nanotube Field Effect Transistors. *ACS Nano* **2012**, *6*, 9657–9661.
27. Zhou, W.; Zhan, S.; Ding, L.; Liu, J. General Rules for Selective Growth of Enriched Semiconducting Single Walled Carbon Nanotubes with Water Vapor as *in Situ* Etchant. *J. Am. Chem. Soc.* **2012**, *134*, 14019–14026.
28. Valuev, I.; Norman, G.; Shub, B. Mechanisms of the Oxidation of Defect-Free Surfaces of Carbon Nanostructures: The Influence of Surface Curvature. *Russ. J. Phys. Chem. B* **2011**, *5*, 156–162.
29. Hahn, J. R. Kinetic Study of Graphite Oxidation along Two Lattice Directions. *Carbon* **2005**, *43*, 1506–1511.
30. Jhi, S.; Louie, S. G.; Cohen, M. L. Electronic Properties of Oxidized Carbon Nanotubes. *Phys. Rev. Lett.* **2000**, *85*, 1710–1713.
31. Lee, S. M.; Lee, Y. H.; Hwang, Y. G.; Hahn, J. R.; Kang, H. Defect-Induced Oxidation of Graphite. *Phys. Rev. Lett.* **1999**, *82*, 217–220.
32. Sorescu, D. C.; Jordan, K. D.; Avouris, P. Theoretical Study of Oxygen Adsorption on Graphite and the (8,0) Single-Walled Carbon Nanotube. *J. Phys. Chem. B* **2001**, *105*, 11227–11232.
33. Osswald, S.; Flahaut, E.; Gogotsi, Y. *In Situ* Raman Spectroscopy Study of Oxidation of Double- and Single-Wall Carbon Nanotubes. *Chem. Mater.* **2006**, *18*, 1525–1533.
34. Collins, P. G.; Arnold, M. S.; Avouris, P. Engineering Carbon Nanotubes and Nanotube Circuits using Electrical Breakdown. *Science* **2001**, *292*, 706–709.
35. Zhang, H.; Liu, Y.; Cao, L.; Wei, D.; Wang, Y.; Kajiura, H.; Li, Y.; Noda, K.; Luo, G.; Wang, L.; *et al*. A Facile, Low-Cost, and Scalable Method of Selective Etching of Semiconducting Single-Walled Carbon Nanotubes by a Gas Reaction. *Adv. Mater.* **2009**, *21*, 813–816.
36. Hassanien, A.; Tokumoto, M.; Umek, P.; Vrbanic, D.; Mozetic, M.; Mihailovic, D.; Venturini, P.; Pejovnik, S. Selective Etching of Metallic Single-Wall Carbon Nanotubes with Hydrogen Plasma. *Nanotechnology* **2005**, *16*, 278.
37. Zhang, G.; Qi, P.; Wang, X.; Lu, Y.; Li, X.; Tu, R.; Bangsaruntip, S.; Mann, D.; Zhang, L.; Dai, H. Selective Etching of Metallic Carbon Nanotubes by Gas-Phase Reaction. *Science* **2006**, *314*, 974–977.
38. Yang, C.; An, K. H.; Park, J. S.; Park, K. A.; Lim, S. C.; Cho, S.; Lee, Y. S.; Park, W.; Park, C. Y.; Lee, Y. H. Preferential Etching of Metallic Single-Walled Carbon Nanotubes with Small Diameter by Fluorine Gas. *Phys. Rev. B* **2006**, *73*, 075419.
39. Zhou, W.; Ooi, Y. H.; Russo, R.; Papanek, P.; Luzzi, D. E.; Fischer, J. E.; Bronikowski, M. J.; Willis, P. A.; Smalley, R. E. Structural Characterization and Diameter-Dependent Oxidative Stability of Single Wall Carbon Nanotubes Synthesized by the Catalytic Decomposition of CO. *Chem. Phys. Lett.* **2001**, *350*, 6–14.
40. Menna, E.; Della Negra, F.; Dalla Fontana, M.; Meneghetti, M. Selectivity of Chemical Oxidation Attack of Single-Wall Carbon Nanotubes in Solution. *Phys. Rev. B* **2003**, *68*, 193412.
41. Moon, C.; Kim, Y.; Lee, E.; Jin, Y.; Chang, K. J. Mechanism for Oxidative Etching in Carbon Nanotubes. *Phys. Rev. B* **2002**, *65*, 155401.
42. An, K. H.; Park, J. S.; Yang, C.; Jeong, S. Y.; Lim, S. C.; Kang, C.; Son, J.; Jeong, M. S.; Lee, Y. H. A Diameter-Selective Attack of Metallic Carbon Nanotubes by Nitronium Ions. *J. Am. Chem. Soc.* **2005**, *127*, 5196–5203.
43. Ye, J. T.; Tang, Z. K. Raman Spectra and Thermal Stability Analysis of 0.4nm Freestanding Single-Walled Carbon Nanotubes. *Phys. Rev. B* **2005**, *72*, 045414.
44. Kawai, T.; Miyamoto, Y. Chirality-Dependent C-C Bond Breaking of Carbon Nanotubes by Cyclo-Addition of Oxygen Molecule. *Chem. Phys. Lett.* **2008**, *453*, 256–261.
45. Miyata, Y.; Kawai, T.; Miyamoto, Y.; Yanagi, K.; Maniwa, Y.; Kataura, H. Bond-Curvature Effect on Burning of Single-Wall Carbon Nanotubes. *Phys. Status Solidi B* **2007**, *244*, 4035–4039.
46. Miyata, Y.; Maniwa, Y.; Kataura, H. Selective Oxidation of Semiconducting Single-Wall Carbon Nanotubes by Hydrogen Peroxide. *J. Phys. Chem. B* **2006**, *110*, 25–29.
47. Kroes, J. M. H.; Pietrucci, F.; Curioni, A.; Jaafar, R.; Gröning, O.; Andreoni, W. Atomic Oxygen Chemisorption on Carbon Nanotubes Revisited with Theory and Experiment. *J. Phys. Chem. C* **2013**, *117*, 1948–1954.

48. Doyle, C. D.; Rocha, J. R.; Weisman, R. B.; Tour, J. M. Structure-Dependent Reactivity of Semiconducting Single-Walled Carbon Nanotubes with Benzenediazonium Salts. *J. Am. Chem. Soc.* **2008**, *130*, 6795–6800.
49. Song, J. W.; Seo, H. W.; Park, J. K.; Kim, J. E.; Choi, D. G.; Han, C. S. Selective Removal of Metallic SWNTs using Microwave Radiation. *Curr. Appl. Phys.* **2008**, *8*, 725–728.
50. Huang, H.; Maruyama, R.; Noda, K.; Kajiura, H.; Kadono, K. Preferential Destruction of Metallic Single-Walled Carbon Nanotubes by Laser Irradiation. *J. Phys. Chem. B* **2006**, *110*, 7316–7320.
51. Gomez, L. M.; Kumar, A.; Zhang, Y.; Ryu, K.; Badmaev, A.; Zhou, C. Scalable Light-Induced Metal to Semiconductor Conversion of Carbon Nanotubes. *Nano Lett.* **2009**, *9*, 3592–3598.
52. Hong, G.; Zhang, B.; Peng, B.; Zhang, J.; Choi, W. M.; Choi, J.; Kim, J. M.; Liu, Z. Direct Growth of Semiconducting Single-Walled Carbon Nanotube Array. *J. Am. Chem. Soc.* **2009**, *131*, 14642–14643.
53. Li, Y.; Peng, S.; Mann, D.; Cao, J.; Tu, R.; Cho, K. J.; Dai, H. On the Origin of Preferential Growth of Semiconducting Single-Walled Carbon Nanotubes. *J. Phys. Chem. B* **2005**, *109*, 6968–6971.
54. Okazaki, K.; Nakato, Y.; Murakoshi, K. Absolute Potential of the Fermi Level of Isolated Single-Walled Carbon Nanotubes. *Phys. Rev. B* **2003**, *68*, 035434.
55. Suzuki, S.; Watanabe, Y.; Homma, Y.; Fukuba, S.; Heun, S.; Locatelli, A. Work Functions of Individual Single-Walled Carbon Nanotubes. *Appl. Phys. Lett.* **2004**, *85*, 127–129.
56. Kang, S. J.; Song, Y.; Yi, Y.; Choi, W. M.; Yoon, S.; Choi, J. Work-Function Engineering of Carbon Nanotube Transparent Conductive Films. *Carbon* **2010**, *48*, 520–524.
57. Xu, S.; Yuan, G.; Li, C.; Liu, W.; Mimura, H. Modulation of the Work Function of Capped Single-Walled Carbon Nanotube by Alkali-Metal Adsorption: A Theoretical Study. *J. Phys. Chem. C* **2011**, *115*, 8928–8933.
58. Seo, K.; Kim, C.; Choi, Y. S.; Park, K. A.; Lee, Y. H.; Kim, B. Tuning Chirality of Single-Wall Carbon Nanotubes by Selective Etching with Carbon Dioxide. *J. Am. Chem. Soc.* **2003**, *125*, 13946–13947.
59. Chiashi, S.; Kohno, M.; Takata, Y.; Maruyama, S. Localized Synthesis of Single-Walled Carbon Nanotubes on Silicon Substrates by a Laser Heating Catalytic CVD. *J. Phys.: Conf. Ser.* **2007**, *59*, 155.
60. Rao, R.; Liptak, D.; Cherukuri, T.; Yakobson, B. I.; Maruyama, B. *In Situ* Evidence for Chirality-Dependent Growth Rates of Individual Carbon Nanotubes. *Nat. Mater.* **2012**, *11*, 213–216.
61. Osswald, S.; Havel, M.; Gogotsi, Y. Monitoring Oxidation of Multiwalled Carbon Nanotubes by Raman Spectroscopy. *J. Raman Spectrosc.* **2007**, *38*, 728–736.
62. Pauzauskie, P. J.; Jamshidi, A.; Zaug, J. M.; Baker, S.; Han, T. Y. -.; Satcher, J. H.; Wu, M. C. *In Situ* Raman Spectroscopy of COOH-Functionalized SWCNTs Trapped with Optoelectronic Tweezers. *Adv. OptoElectron.* **2012**, *2012*, 4.
63. Kaminska, K.; Lefebvre, J.; Austing, D. G.; Finnie, P. Real-Time *in Situ* Raman Imaging of Carbon Nanotube Growth. *Nanotechnology* **2007**, *18*, 165707.
64. Picher, M.; Anglaret, E.; Arenal, R.; Jourdain, V. Self-Deactivation of Single-Walled Carbon Nanotube Growth Studied by *in Situ* Raman Measurements. *Nano Lett.* **2009**, *9*, 542–547.
65. Li-Pook-Than, A.; Lefebvre, J.; Finnie, P. Phases of Carbon Nanotube Growth and Population Evolution from *in Situ* Raman Spectroscopy during Chemical Vapor Deposition. *J. Phys. Chem. C* **2010**, *114*, 11018–11025.
66. Koh, A. L.; Gidcumb, E.; Zhou, O.; Sinclair, R. Observations of Carbon Nanotube Oxidation in an Aberration-Corrected Environmental Transmission Electron Microscope. *ACS Nano* **2013**, *7*, 2566–2572.
67. Raravikar, N. R.; Keblinski, P.; Rao, A. M.; Dresselhaus, M. S.; Schadler, L. S.; Ajayan, P. M. Temperature Dependence of Radial Breathing Mode Raman Frequency of Single-Walled Carbon Nanotubes. *Phys. Rev. B* **2002**, *66*, 235424.
68. Araujo, P. T.; Pesce, P. B. C.; Dresselhaus, M. S.; Sato, K.; Saito, R.; Jorio, A. Resonance Raman Spectroscopy of the Radial Breathing Modes in Carbon Nanotubes. *Phys. E* **2010**, *42*, 1251–1261.
69. Qu, L.; Du, F.; Dai, L. Preferential Syntheses of Semiconducting Vertically Aligned Single-Walled Carbon Nanotubes for Direct Use in FETs. *Nano Lett.* **2008**, *8*, 2682–2687.
70. Telg, H.; Duque, J. G.; Staiger, M.; Tu, X.; Hennrich, F.; Kappes, M. M.; Zheng, M.; Maultzsch, J.; Thomsen, C.; Doorn, S. K. Chiral Index Dependence of the G+ and G− Raman Modes in Semiconducting Carbon Nanotubes. *ACS Nano* **2012**, *6*, 904–911.
71. Dresselhaus, M. S.; Dresselhaus, G.; Saito, R.; Jorio, A. Raman Spectroscopy of Carbon Nanotubes. *Phys. Rep.* **2005**, *409*, 47–99.
72. Jorio, A.; Souza Filho, A. G.; Dresselhaus, G.; Dresselhaus, M. S.; Swan, A. K.; Unlu, M. S.; Goldberg, B. B.; Pimenta, M. A.; Hafner, J. H.; Lieber, C. M.; *et al*. G-Band Resonant Raman Study of 62 Isolated Single-Wall Carbon Nanotubes. *Phys. Rev. B* **2002**, *65*, 155412.
73. Qiu, H.; Maeda, Y.; Akasaka, T. Facile and Scalable Route for Highly Efficient Enrichment of Semiconducting Single-Walled Carbon Nanotubes. *J. Am. Chem. Soc.* **2009**, *131*, 16529–16533.
74. Saito, R.; Fantini, C.; Jiang, J. In *Excitonic States and Resonance Raman Spectroscopy of Single-Wall Carbon Nanotubes*; Jorio, A., Dresselhaus, G., Dresselhaus, M. S., Eds.; *Carbon Nanotubes: Advanced Topics in the Synthesis, Structure, Properties and Applications* (Topics in Applied Physics); Springer-Verlag: Berlin, 2008; Vol. 111, p 251.
75. McClain, D.; Thomas, N.; Youkey, S.; Schaller, R.; Jiao, J.; O'Brien, K. P. Impact of Oxygen Adsorption on a Population of Mass Produced Carbon Nanotube Field Effect Transistors. *Carbon* **2009**, *47*, 1493–1500.
76. Caudal, N.; Saitta, A. M.; Lazzeri, M.; Mauri, F. Kohn Anomalies and Nonadiabaticity in Doped Carbon Nanotubes. *Phys. Rev. B* **2007**, *75*, 115423.
77. Farhat, H.; Son, H.; Samsonidze, G. G.; Reich, S.; Dresselhaus, M. S.; Kong, J. Phonon Softening in Individual Metallic Carbon Nanotubes Due to the Kohn Anomaly. *Phys. Rev. Lett.* **2007**, *99*, 145506.
78. Kavan, L.; Rapta, P.; Dunsch, L.; Bronikowski, M. J.; Willis, P.; Smalley, R. E. Electrochemical Tuning of Electronic Structure of Single-Walled Carbon Nanotubes: In-Situ Raman and Vis-NIR Study. *J. Phys. Chem. B* **2001**, *105*, 10764–10771.
79. Mews, A.; Jiang, C.; Schuessler, T.; Philipp, G.; Fan, Y.; Burghard, M. Raman Investigation of Single Oxidized Carbon Nanotubes. *Isr. J. Chem.* **2001**, *41*, 15–22.
80. Kumar, R.; Cronin, S. B. Raman Scattering of Carbon Nanotube Bundles Under Axial Strain and Strain-Induced Debundling. *Phys. Rev. B* **2007**, *75*, 155421.
81. Usrey, M. L.; Lippmann, E. S.; Strano, M. S. Evidence for a Two-Step Mechanism in Electronically Selective Single-Walled Carbon Nanotube Reactions. *J. Am. Chem. Soc.* **2005**, *127*, 16129–16135.
82. Lu, J.; Nagase, S.; Zhang, X.; Wang, D.; Ni, M.; Maeda, Y.; Wakahara, T.; Nakahodo, T.; Tsuchiya, T.; Akasaka, T.; *et al*. Selective Interaction of Large or Charge-Transfer Aromatic Molecules with Metallic Single-Wall Carbon Nanotubes: Critical Role of the Molecular Size and Orientation. *J. Am. Chem. Soc.* **2006**, *128*, 5114–5118.
83. An, L.; Fu, Q.; Lu, C.; Liu, J. A Simple Chemical Route to Selectively Eliminate Metallic Carbon Nanotubes in Nanotube Network Devices. *J. Am. Chem. Soc.* **2004**, *126*, 10520–10521.
84. Choubak, S.; Biron, M.; Levesque, P. L.; Martel, R.; Desjardins, P. No Graphene Etching in Purified Hydrogen. *J. Phys. Chem. Lett.* **2013**, *4*, 1100–1103.
85. Strano, M. S.; Dyke, C. A.; Usrey, M. L.; Barone, P. W.; Allen, M. J.; Shan, H.; Kittrell, C.; Hauge, R. H.; Tour, J. M.; Smalley, R. E. Electronic Structure Control of Single-Walled Carbon Nanotube Functionalization. *Science* **2003**, *301*, 1519–1522.
86. Ding, L.; Tselev, A.; Wang, J.; Yuan, D.; Chu, H.; McNicholas, T. P.; Li, Y.; Liu, J. Selective Growth of Well-Aligned Semiconducting Single-Walled Carbon Nanotubes. *Nano Lett.* **2009**, *9*, 800–805.
87. Park, H.; Zhao, J.; Lu, J. P. Distinct Properties of Single-Wall Carbon Nanotubes with Monovalent Sidewall Additions. *Nanotechnology* **2005**, *16*, 635–638.

88. Harutyunyan, A. R.; Chen, G.; Paronyan, T. M.; Pigos, E. M.; Kuznetsov, O. A.; Hewaparakrama, K.; Kim, S. M.; Zakharov, D.; Stach, E. A.; Sumanasekera, G. U. Preferential Growth of Single-Walled Carbon Nanotubes with Metallic Conductivity. *Science* **2009**, *326*, 116–120.
89. Lee, J. H.; Shin, J. H.; Kim, Y. H.; Park, S. M.; Alegaonkar, P. S.; Yoo, J. A New Method of Carbon-Nanotube Patterning Using Reduction Potentials. *Adv. Mater.* **2009**, *21*, 1257–1260.
90. Ding, F.; Harutyunyan, A. R.; Yakobson, B. I. Dislocation Theory of Chirality-Controlled Nanotube Growth. *Proc. Natl. Acad. Sci.* **2009**, *106*, 2506–2509.
91. Finnie, P.; Li-Pook-Than, A.; Lefebvre, J.; Austing, D. G. Optimization of Methane Cold Wall Chemical Vapor Deposition for the Production of Single Walled Carbon Nanotubes and Devices. *Carbon* **2006**, *44*, 3199–3206.

Type and Species Selective Air Etching of Single Walled Carbon Nanotubes Studied with *In Situ* Raman Spectroscopy

Andrew Li-Pook-Than [†‡], *Jacques Lefebvre* [†] *and Paul Finnie* *[†‡]

[†]Institute for Microstructural Sciences, National Research Council Canada, Building M-50, 1200 Montreal Road, Ottawa, ON, K1A 0R6, Canada and [‡]Department of Physics, University of Ottawa, 150 Louis Pasteur, Ottawa, ON, K1N 6N5, Canada

Supporting Information (19 pp.)

Diameter and chirality assignment for Radial Breathing Mode and G- peaks. Raman spectra of sample etched at T = 600°C. Radial Breathing Mode time evolution plots. This material is available free of charge via the Internet at http://pubs.acs.org.

1. Diameter and chirality assignment

A standard way to determine the (n,m) of single walled carbon nanotubes (SWNTs) is to use the so called Kataura plot. In the Kataura plot, the Raman laser energy is displayed on the y-axis, while the measured Radial Breathing Mode (RBM) frequency is on the x-axis. Because the RBM frequency is roughly inversely proportional to nanotube diameter, and because RBM visibility depends on being resonant with laser energy, with the resonances being chirality dependent, each nanotube has a specific

position on the Kataura plot. In essence, each SWNT chirality (n,m) is assigned to different ω_{RBM} and E_{ii} pairs.

In this work, Kataura plots are obtained using data from R. Saito's Exciton Kataura Plot page (i.e. http://flex.phys.tohoku.ac.jp/eii/).[1, 2]

Assignment may not be straightforward because RBM frequencies shift weakly and resonance energies (i.e. E_{11}, E_{22}, etc.) shift strongly under different nanotube environments. Specifically, these pairings can be sensitive to a dielectric function κ, which depends on local environment and nanotube diameter.[1] Furthermore, we are using a fixed wavelength laser so observation of an RBM means the laser is "near" the resonant frequency (i.e. within ~100 meV), but we do not determine the exact resonance (i.e. position on the y-axis of the Kataura plot).[3]

In Table S1, we list the room temperature RBMs shown in Figure 3. Our aim is to assign these to specific species.

A simple model of the diameter dependence of the RBM frequency is $\omega_{RBM} = A/d_t + B$, where A and B are constants that depend on local environment and sample type. This has often been used to assign experimental RBM peaks; different values for A and B have been obtained in different studies.[4-7] Since our samples were grown under water-assisted CVD on Si subtrate, we expect A to vary between 227 nm·cm^{-1} and 248 nm·cm^{-1}, while B should be close to 0 cm^{-1}.[8, 9] These extreme limits correspond to Models 1 and 3 in Table S1.

Another model for the diameter dependence is described by $\omega_{RBM} = (227/d_t)\sqrt{1 + C_e \cdot d_t^2}$, where C_e is a constant sensitive to the environment surrounding the nanotubes.[4, 10] If peaks *g*, *h*, and *i* are assigned to (8,4), (9,2), and (6,5),[11]

we obtain $C_e = 0.046\ nm^{-2} \pm 0.020\ nm^{-2}$, which corresponds to Model 2 in Table S1. This model likely corresponds to the most likely peak assignment.

		Extreme Case 1		Most Likely Assignment		Extreme Case 2	
Peak Label (Fig 3)	Raman Shift (cm^{-1})	Diameter (nm) Model 1 A = 227 $nm \cdot cm^{-1}$, B = 0 cm^{-1}	Assignment Model 1 A = 227 $nm \cdot cm^{-1}$, B = 0 cm^{-1}	Diameter (nm) Model 2 $C_e = 0.046$ nm^{-2}	Assignment Model 2 $C_e = 0.046$ nm^{-2}	Diameter (nm) Model 3 A = 248 $nm \cdot cm^{-1}$, B = 0 cm^{-1}	Assignment Model 3 A = 248 $nm \cdot cm^{-1}$, B = 0 cm^{-1}
a	145	1.57	S	1.66	S	1.71	S
b	177	1.28	S (E_{33}^S) or M (E_{11}^M)	1.33	S (E_{33}^S) or M (E_{11}^M)	1.40	S (E_{33}^S) or M (E_{11}^M)
c	192	1.18	S (E_{33}^S) or M (E_{11}^M)	1.22	S (E_{33}^S) or M (E_{11}^M)	1.29	S (E_{33}^S) or M (E_{11}^M)
d	217	1.05	M (E_{11}^M)	1.07	M (E_{11}^M)	1.14	M (E_{11}^M)
e	230	0.99	M (E_{11}^M)	1.01	M (E_{11}^M)	1.08	M (E_{11}^M)
f	236	0.96	M (E_{11}^M)	0.98	M (E_{11}^M)	1.05	M (E_{11}^M)
g	273	0.83	(8, 4) S (E_{22}^S)	0.85	(8, 4) S (E_{22}^S)	0.91	(11,1) S (E_{22}^S)
h	290	0.78	(9,2) S (E_{22}^S)	0.79	(9,2) S (E_{22}^S)	0.86	(8, 4) S (E_{22}^S)
i	307	0.74	(6,5) S (E_{22}^S)	0.75	(6,5) S (E_{22}^S)	0.81	(9,2) S (E_{22}^S)

S=semiconducting, M=metallic

Table S1. Radial Breathing Mode assignments

Assignments using these three models are graphically shown in Figures S1 to S3. Assignments from Models 1 and 2 are probably more accurate than those in Model 3.

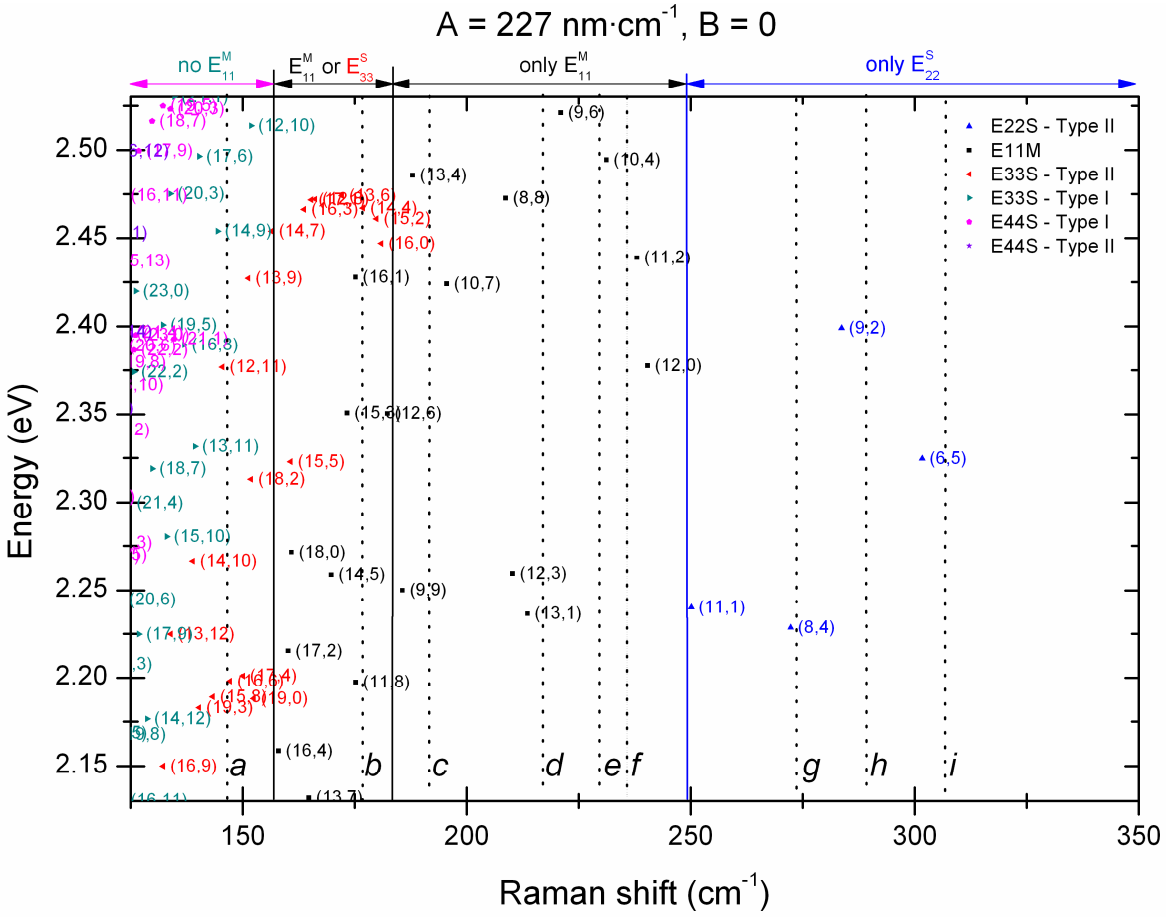

Figure S1. Kataura plot for the Extreme Case of Model 1. Frequencies were calculated using the expression $\omega_{RBM} = A/d_t + B$, where A = 227 nm·cm^{-1}, B = 0 cm^{-1}. Different (n,m) values are present. Only diameters larger than 0.7 nm are shown. Dotted lines represent observed RBMs shown in Figure 3. Points are labelled by the band they originate in. Semiconducting, metallic and mixed regions are delineated with respect to

the labels along the top axis, indicating the band of origin (e.g. E_{11}^{M} is metallic, E_{22}^{S} is semiconducting) along the top horizontal axis.

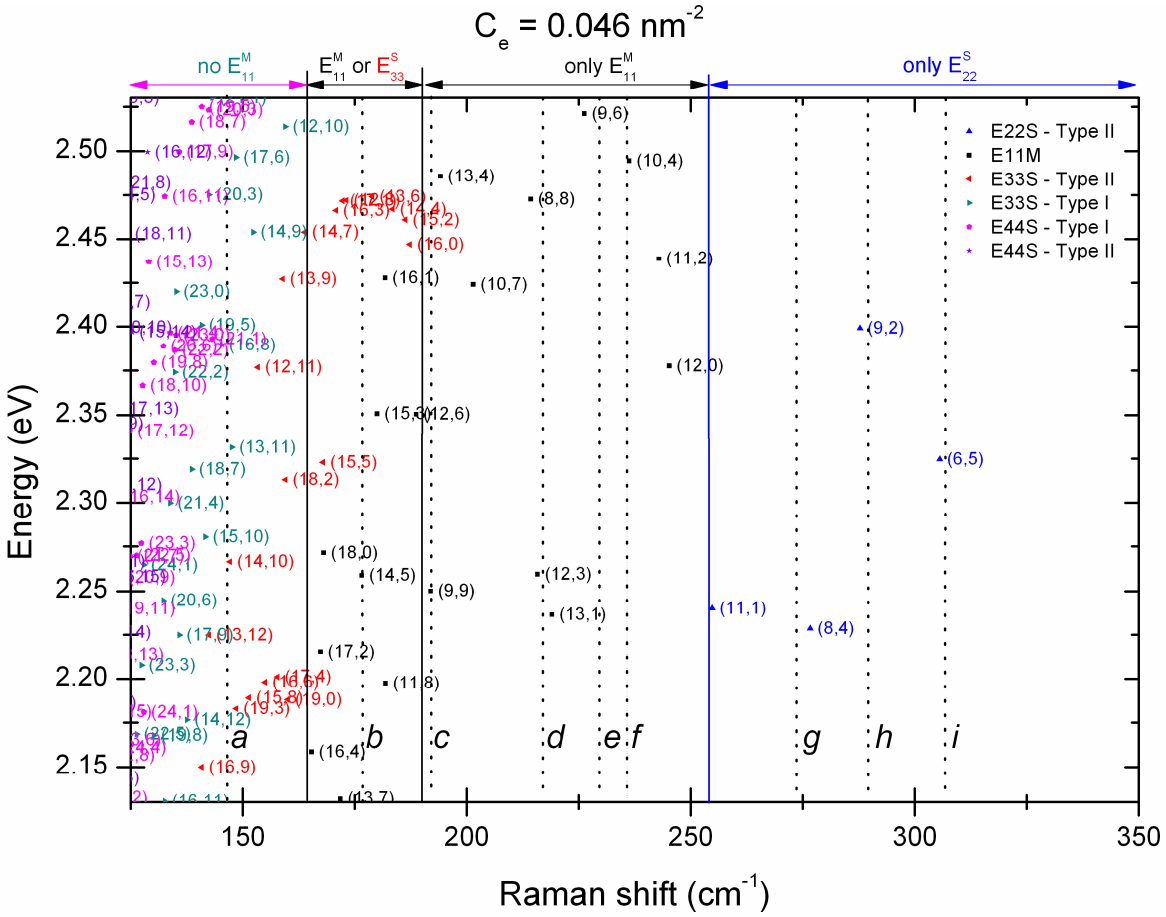

Figure S2. Kataura plot for the Most Likely Assigment of Model 2. Frequencies were calculated using the expression $\omega_{RBM} = (227/d_t)\sqrt{1 + C_e \cdot d_t^2}$, where $C_e = 0.046$ nm^{-2}. Different (n,m) values are present. Only diameters larger than 0.7 nm are shown. Dotted lines represent observed RBMs shown in Figure 3. Points are labelled by the band they originate in. Semiconducting, metallic and mixed regions are delineated with respect to the labels along the top axis, indicating the band of origin along the top horizontal axis.

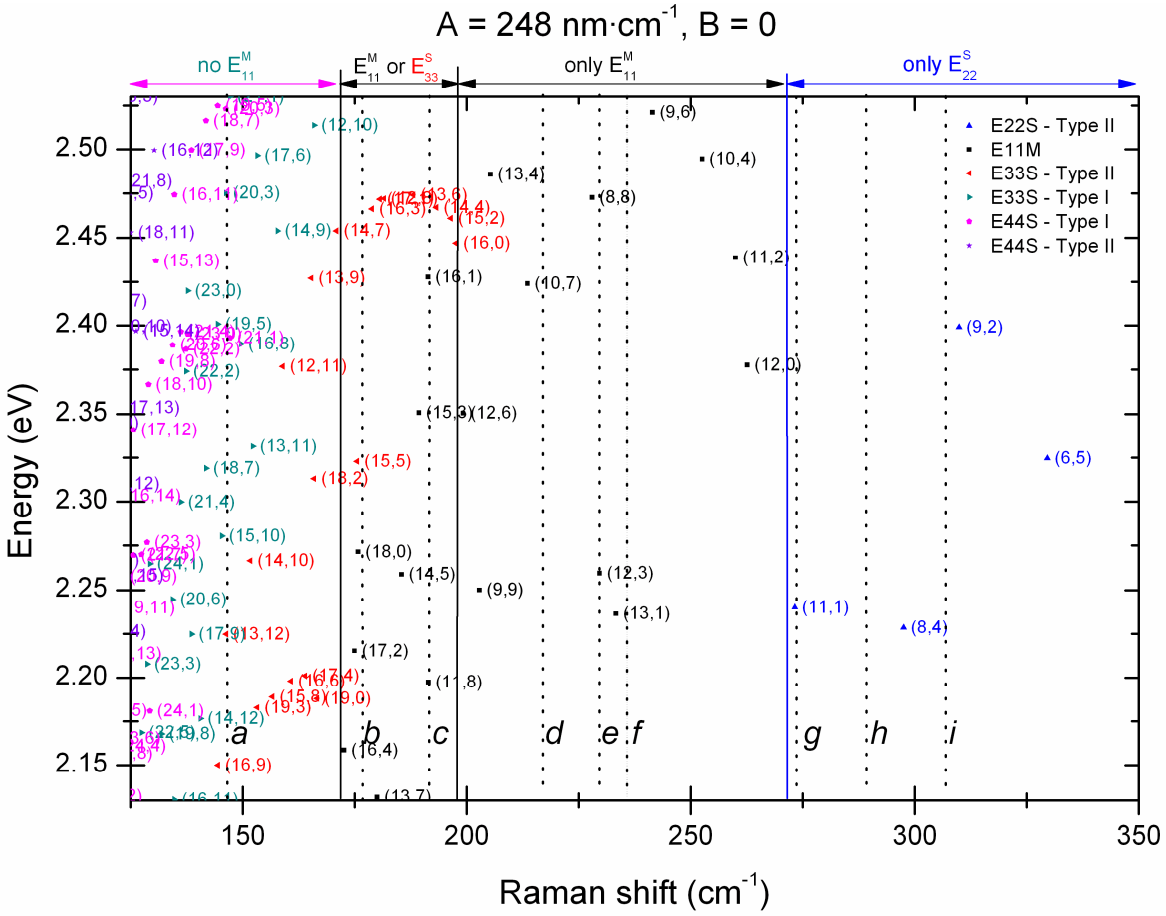

Figure S3. Kataura plot for the Extreme Case of Model 3. Frequencies were calculated using the expression $\omega_{RBM} = A/d_t + B$, where A = 248 nm·cm^{-1}, B = 0 cm^{-1}. Different (n,m) values are present. Only diameters larger than 0.7 nm are shown. Dotted lines represent observed RBMs shown in Figure 3. Points are labelled by the band they originate in. Semiconducting, metallic and mixed regions are delineated with respect to the labels along the top axis, indicating the band of origin along the top horizontal axis.

There is no obvious scaling of etch rates with chiral angle. However, all three models predict that peak *a* is semiconducting (E_{33}^S or E_{44}^S), peaks *d* to *f* are metallic

(E_{11}^M), and peaks *g* to *i* are semiconducting (E_{22}^S). Peaks *b* and *c* may be either type (E_{11}^M or E_{22}^S).

We can similarly use the G- peaks in Figure 3 for assignment; see Table S2.[3, 9] The G- resonance window is larger than the RBM resonance window. As a result, while all the strongest RBM peaks should produce visible G- peaks, some G- peaks may correspond to RBMs that are off-resonance and not visible. The center of the windows and window width may shift depending whether the plot corresponds well to sample environment. For example, CNT bundling can widen the RBM window.[6, 12]

Label	Raman Shift (cm^{-1})	Diameter (nm)	Assignment	Comments
I	~1504 cm^{-1}	~0.85	M	Corresponds to unresolved RBMs at 240-255 cm^{-1}
II	1523 cm^{-1}	0.75 (1.00)	S (M)	Corresponds to RBM-*i* (overlapping RBM-*d* to *f*)
III	1540 cm^{-1}	~0.85	S	Corresponds to RBM-*g* or *h*
IV	~1562 cm^{-1}	~1.20	S	Corresponds to RBM-*b* and/or RBM-*c*
V	1570 cm^{-1}	~1.50	S	Corresponds to RBM-*a*

Table S2. G- band assignments

The (6,5) nanotube, assigned to peak-*i* in Model 1, is highly resonant and was found by Telg et al. to generate a G- at 1528 cm^{-1}.[3] This likely corresponds to the G- peak near 1523 cm^{-1} (peak-II). Also in this spectral range are metallic peaks from larger diameter nanotubes. Although the (6,4) species may also contribute, it is not clearly visible in the RBM region.

If the 1540 cm^{-1} peak is semiconducting it should correspond to diameters of close to ~0.85 nm.[3, 9] For Model 1 this would correspond to ~270 cm^{-1} (peak-*g*), or for Model 3 this would correspond to 290 ~cm^{-1} (peak-*h*). In either assignment these peaks are semiconducting.

The low intensity G- peak at ~1504 cm^{-1} is most likely to be metallic. A semiconducting nanotube in this would not be very stable as it would correspond to diameters of ~0.5 nm. Additionally, the lineshape of the G- in this region appears to be asymmetric, likely having a "Breit-Wigner-Fano lineshape" typical of metallic CNTs. Metallic tubes with this resonance are ~1 nm in diameter, and thus this correlates well with the large unresolved RBM shoulder at around 240-250 cm^{-1}.

After the etching procedure all the previously discussed G- peaks are destroyed. However, as shown in Figure 3(a), RBMs-*b* and *c* (i.e. 177 cm^{-1} and 192 cm^{-1}) are fairly persistent. Notably, the G- doublet (i.e. 1562 cm^{-1} and 1570 cm^{-1}) in Figure 3(b) is also persistent. The presence of a semiconducting G- near 1562 cm^{-1} suggests that at least one of *b* and *c* are semiconducting, if not both. The peak at 1570 cm^{-1} likely corresponds to the semiconducting RBM-*a*.[3]

2. Raman spectra of sample etched at T = 600°C

The result of etching at T = 600 °C is presented in Figure S4. As seen in Figure 2(a), the ~10 RBMs of interest at low temperature are also present at high temperature, although individual RBM peaks have downshifted, and not all the same RBM peaks are visible due to the change in resonance conditions. We indicate peaks *a*: 140 cm^{-1}, *b*: 168 cm^{-1}, c: 185 cm^{-1}, *d:* 203 cm^{-1}, *d**: 211 cm^{-1}, *e*: 225 cm^{-1}, *f*: 240 cm^{-1}, *g*: 260 cm^{-1}, *g**: 266 cm^{-1}, *h*: 280 cm^{-1}, *i*: 290 cm^{-1}. RBMs-*d*/*d** and *g*/*g** may be doublet peaks, perhaps containing peaks from species only resonant at high temperatures. A 295 cm^{-1} SiO_2 background peak (blue) is present.

RBM etching is much more complete than in the low temperature case and air input was stopped (at t = 16 min) before the sample was entirely etched away. It appears that the diameter dependence is more pronounced at these high temperatures, or alternatively, when the etching is continued for a long time. Similar trends are likely present but less pronounced than at low temperatures. For example, it is unclear whether the higher etching temperature reduces etching peak-*c* selectivity, although the spectrum at t = 3 min 30 s seems comparable to the final spectrum in Figure 2a. The weak RBM-*a* peak is difficult to track visually, but seems to vanish the earliest after t = 2 min 30 s.

The corresponding change in the normalized G and D bands is much more pronounced in Figure 3(b) and 3(c), respectively. After t = 9 min 30 s, the G band is still easily visible, though much sharper, and the D band has completely vanished. Prior to this, the D band frequency upshifts from 1316 cm^{-1} to 1323 cm^{-1}, indicating a change in bundling or a loss in resonant small diameter nanotubes.[5] Likewise, the loss in G-

intensity below 1567 cm^{-1} is much more significant than for the lower etch temperature case. The loss in Breit-Wigner-Fano (BWF) character in the G- region is obvious, suggesting that the surviving RBM-c and RBM-d peaks correspond, at least in part, to semiconducting species.

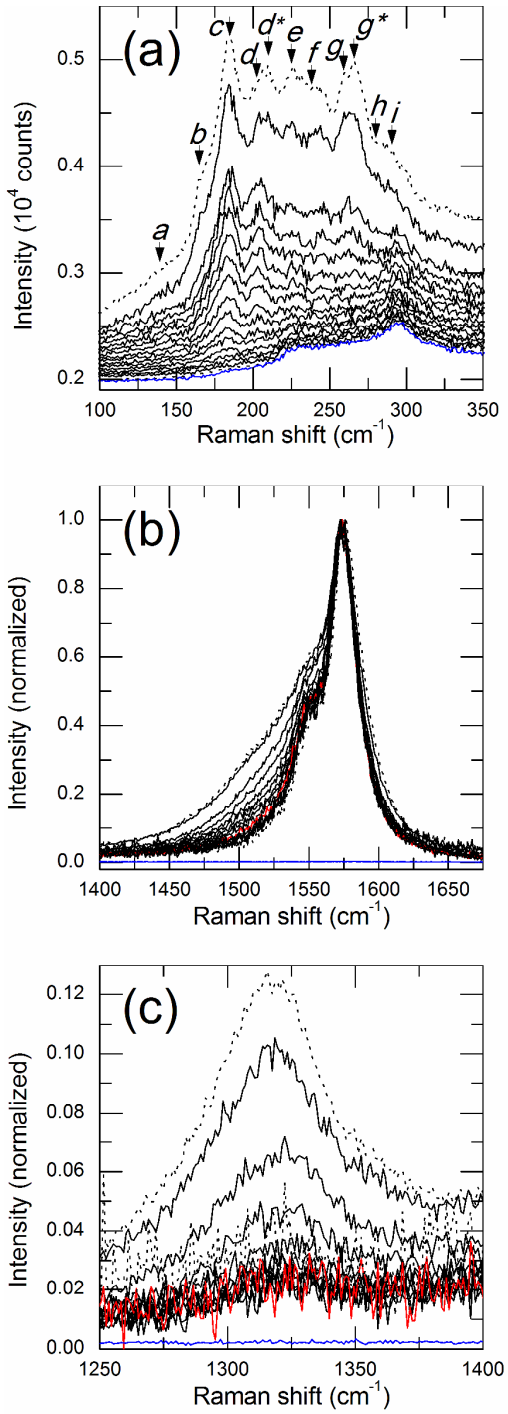

Figure S4. *In situ* Raman spectra of a sample being etched at 600 °C, displayed chronologically from top to bottom. (a) Spectral changes in the RBM region. Also shown are corresponding changes to (b) G and (c) D bands. The top and bottom dotted spectra

correspond respectively to pre- and post-etch spectra (after t = 16 min) for the sample (30 s exposure and scaled to black frames). The correspond Si/SiO_2 backgrounds are displayed in blue. In (a) the spectra are shown every 1 min, from t = 30 s to t = 14 min 30 s, with air input occurring at t = 0 s. In (b) and (c), every spectrum is normalized to their maximum G band intensity. In (b), spectra are shown every 1 min, from t = 30 s to t = 12 min 30 s. In (c), spectra are shown every 1 min, from t = 30 s to t = 10 min 30 s.

3. RBM Time Evolution Curves

Figure S5 displays the time evolution of the most intense RBM peaks for the 350°C air etched sample, compared with the time evolution of the G and D bands. With respect to the peaks in Figure 2(a), the evolution of peaks-*b*, *c*, and *g* are plotted. The evolution of peaks-*e* and *f* is also plotted, but since the peaks overlap, the sum of both signals was plotted together. As usual, peak evolution is scaled with respect to the Si band, and normalized with respect to peak signal at t = 0 s.

A significant amount of noise is present in these curves due to the comparatively low signals of the RBM peaks. Data extraction is further complicated by the presence of a non-flat background and unresolved RBMs that are close to the distinct RBM peaks.

The RBM time evolution curves correspond well with the changes directly observed in Figure 2(a). RBM-*c* is by far the most persistent peak followed by RBM-*g*. The likely E_{11}^{M} peaks at *e* and *f* etch rapidly. The RBM-*b* shoulder peak also appears to decrease very rapidly, however it must be noted that as a shoulder peak, background subtraction is particularly subject to error. A simple model with an increasing etch rate with decreasing diameter cannot explain the extracted RBM evolution curves as we have in order of etch rate b>e+f>g(>D>G>)c where if the order were determined by this simple model we would have g>e+f>c>b which is not observed.

As shown in Figure 5, the G band tracks relatively well with the persistent RBM-*c* peak. This makes some sense since CNTs corresponding to the other RBMs are destroyed and cannot contribute as much to the G band.

Another simple model might be that the etch rate is determined by sidewall defects, with tubes etching proportionally with their defect densities. In that case one would expect an etch rate proportional to the D band intensity. With the exception of perhaps the RBM-*g* this is not the case, and such a defect etching model can be ruled out.

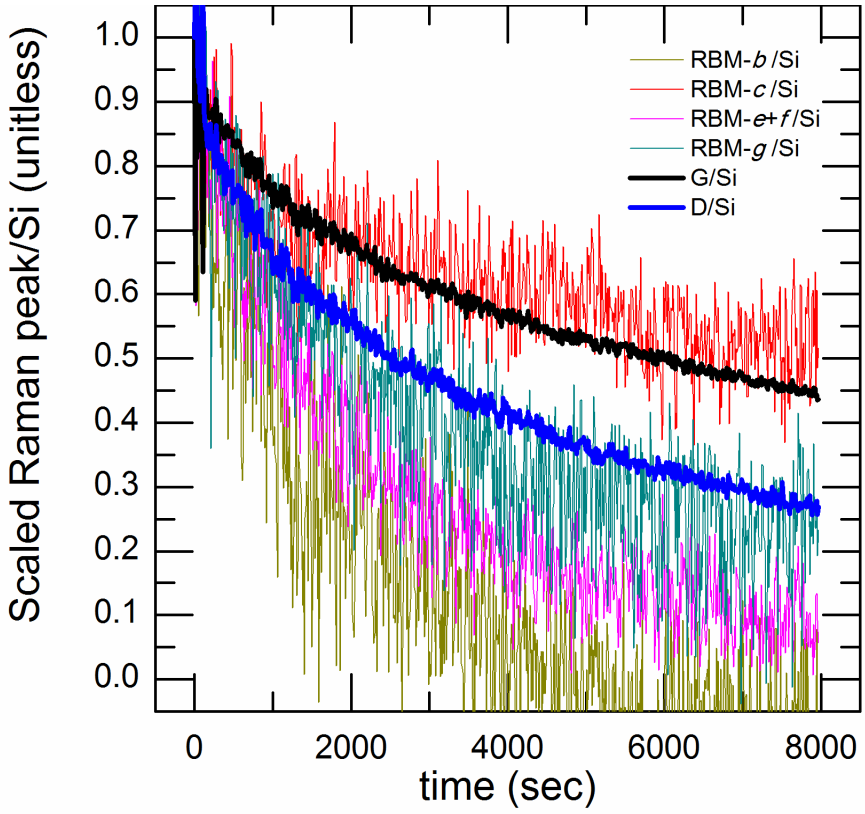

Figure S5. Time evolution of Raman peaks compared with the G and D bands for the sample etched at 350°C. The evolution curves of the scaled, normalized peaks at 177 cm^{-1} (dark yellow), 192 cm^{-1} (red), 230 cm^{-1} and 236 cm^{-1} (magenta), 273 cm^{-1} (dark cyan), alongside the G (black) and D bands (blue), are plotted.

4. D/G Time Evolution Curves

Figure S6 displays the D/G time evolution for all samples from T = 300 °C to 600 °C. The 500 °C sample was more crystalline to begin with and therefore has the least signal due its low D band values. Also note that at higher etch temperatures, pre-etch D band intensities were lowered more than the pre-etch G band intensities due to the change in resonance, so the initial D/G values scale with temperature to an extent. Comparing these values to Figure 4, one can show that D/G time evolution scales directly with remaining G band intensity independently of etching temperature, at least for low temperatures. For example, from T = 350 °C to 500 °C the D/G ratio drops by ~33%, once G band intensity falls by 50%. To obtain high crystallinity samples, prolonged etching is required. For a ~80% drop in D/G, the G band intensity must fall by 72%, and for a ~90% drop in D/G, G band intensity must fall by 80%.

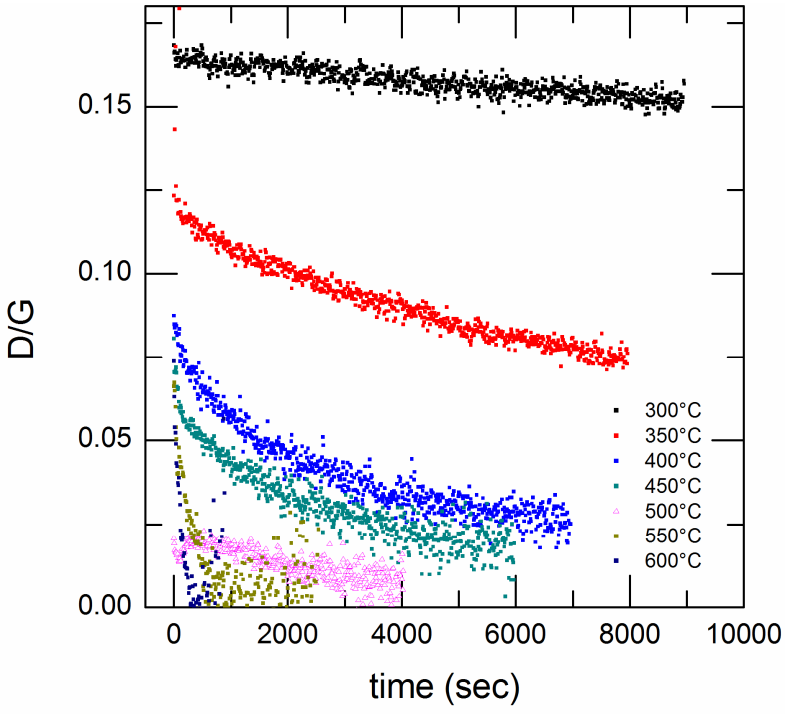

Figure S6. D/G time evolution normalized to initial values from T = 300 °C to 600 °C.

5. Alternative Activated Plots

Instead of performing the biexponential fit shown in Figure 5, one exponential can be fit at early times (red) and one exponential can be fit at late times (green) as shown in Figure S7. These fits were performed for all G and D band time evolution curves, such that time constants τ_{fast} and τ_{slow} can be obtained from the fast (red) and slow (green) components, as they were for the biexponential fit.

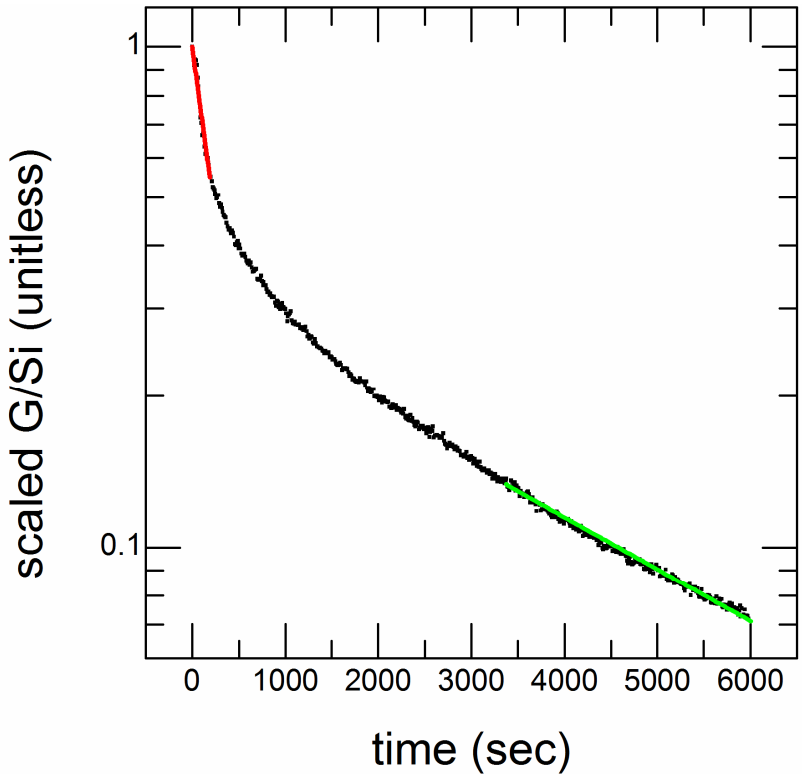

Figure S7. Alternative two exponential fit of the G band signal (normalized to the Si intensity) for the 450° C etched sample. Independent slow (green) and fast (red) fits are indicated.

Using this alternative fitting scheme, alternative activation plots for the G and D bands are given in Figure S8. The fast (black squares) and slow (red squares) G band etch rates are activated with energies 0.53 eV ± 0.10 eV and 0.47 eV ± 0.07 eV, respectively. The fast (blue triangles) and slow (green triangles) D band etch rates are activated with energies 0.63 eV ± 0.11 eV and 0.39 eV ± 0.07 eV, respectively. The large uncertainty makes these activation energies barely distinguishable if at all.

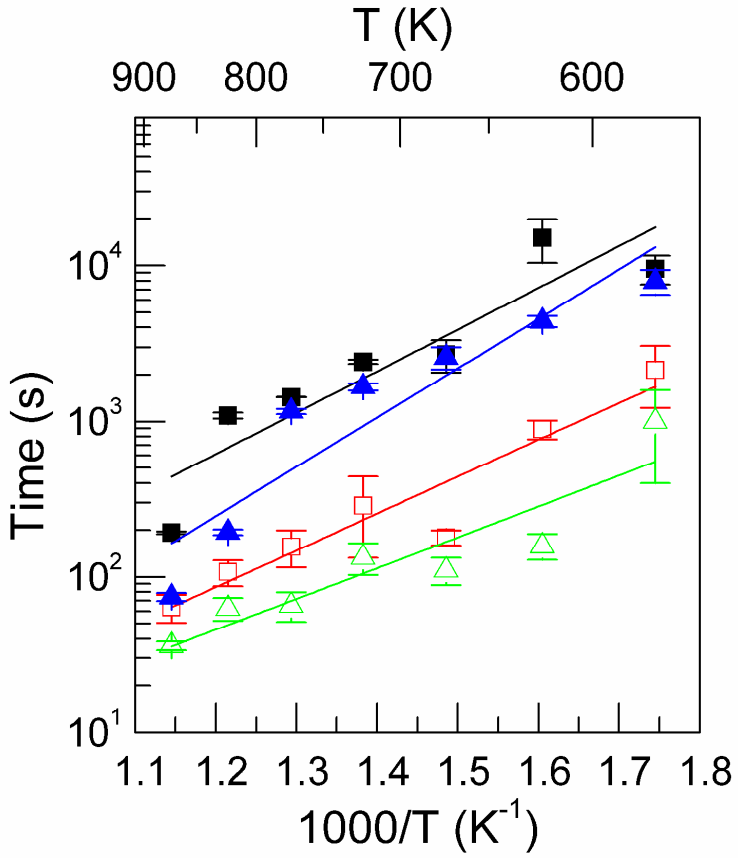

Figure S8. Activation plots for the G band fast (black square) and slow (red square) τ values and for the D band fast (blue triangle) and slow (green triangle) τ values. Activation energies are taken from the slopes of the four linear fits and are listed above.

6. TEM images

Transmission electron microscope (TEM) images of a typical pre-etch sample, taken using a JEOL JEM-2100F TEM, are shown in Figure S9. CNTs were transferred by mechanically passing the surface of the sample across a carbon TEM grid.

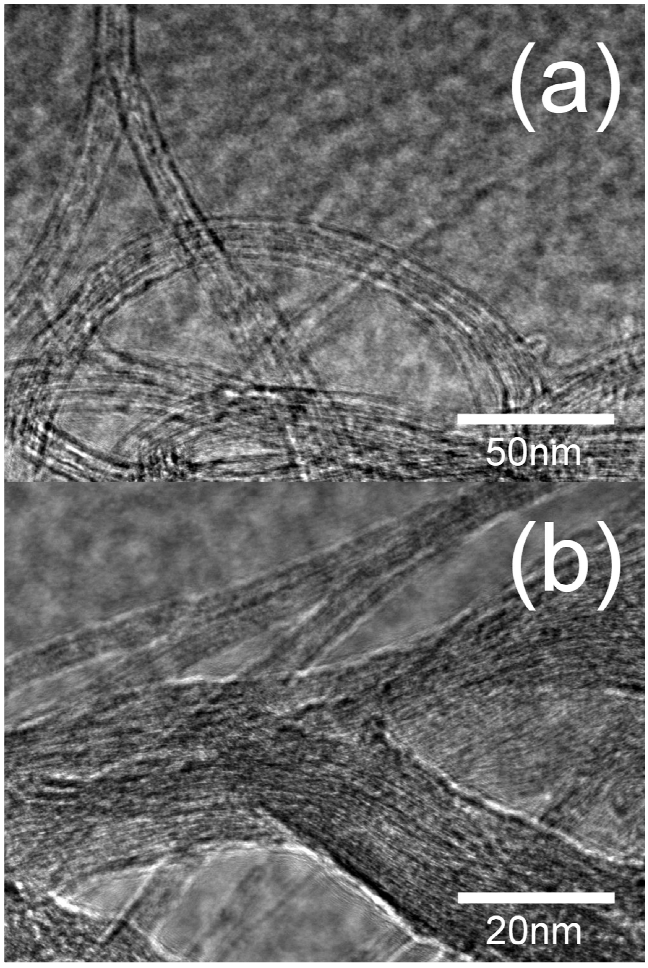

Figure S9. Typical TEM micrographs of the pre-etch sample at different magnifications.

As seen in Figure S9, SWNT bundles <25 nm in thickness are typical, such that thicker bundles often split into thinner bundles and individual SWNTs. Individual CNTs with diameters <5 nm and thin bundles composed of 2-3 CNTs are visible. We were able

to find some isolated individual nanotubes, but they degraded quickly in the TEM. Most tubes were bundled however, and these were more stable in the beam.

From the TEM images we note that large isolated pieces of amorphous carbon are not visible. However, there may be unresolved graphitic carbon coatings intimately contacting the surfaces of nanotubes or bundles. We lack the TEM resolution here to distinguish them. The CNT walls do not appear to be particularly defective.

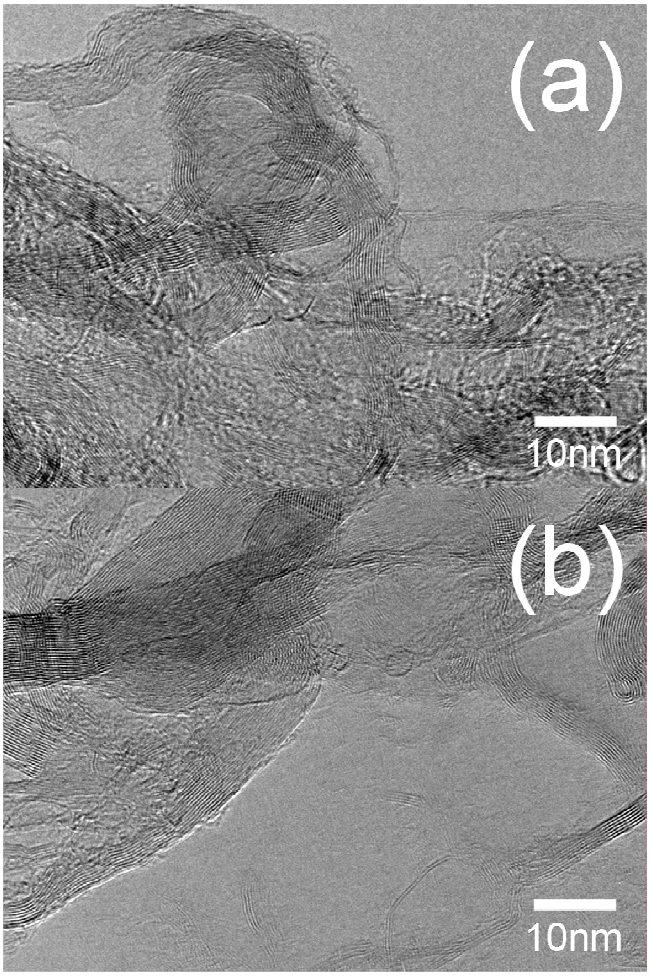

Figure S10: High resolution TEM micrographs of the pre-etch sample.

High-resolution TEM (HRTEM) images of the pre-etch sample were also taken using a Titan^3 80-300 TEM operated at 300 keV. CNTs were transferred by mechanically rubbing the nanotube sample surface onto a lacey carbon grid. Two typical images (a) and (b) are shown in Figure S10.

Consistent with the SEM observations and Raman data, the vast majority nanotubes are organized into bundles, ranging here from ~2 nm to ~10 nm in width. These bundles are extremely well graphitized, with little if any evidence of any amorphous carbon in their interiors. They can be seen to cross in front of other bundles and bundle together into networks in many cases. Individual SWNTs of different diameters can also be seen in places. For the most part the individual nanotubes and bundles of nanotubes appear largely free of coatings, despite the fact that we were looking for examples of particularly coated nanotubes. In some places in these images it is possible to see what might be thin layers of poorly structured carbon on the outside of bundles or individual nanotubes. However, image artifacts such as those due to depth of focus and motion make this unclear, and furthermore TEM induced damage and deposition may also contribute. Certainly, as in the low resolution TEM, there is no evidence of large flakes of amorphous carbon. Here many clean nanotubes and bundles of nanotubes are seen. The level of non-nanotube carbon coating thus appears quite limited, consistent with the XPS, SEM and Raman data.

7. *Ex situ* Raman spectral changes to 400°C etched sample with four laser lines

The *ex situ* Raman spectra of the CNT sample etched at 400°C was obtained using four laser excitation wavelengths at 514 nm, 532 nm, 633 nm, and 785 nm. Both the pre- and post-etch Raman spectra were collected at room temperature for each laser line. The *ex situ* 532 nm spectra were taken using the same apparatus and setup as all the *in situ* spectra. The 514 nm, 633 nm, and 785 nm spectra were taken using a commercial Renishaw inVia Raman microscope system using a slit illuminated 20× objective, with incident laser powers <1 mW. The 532 nm spectra were taken on the same sample and location before and after etching, while the remaining spectra were taken on separate samples and different locations.

These spectra are presented in Figure S11. Spectra above 1692 cm^{-1} for the 532 nm spectra could not be collected. Pre- and post-etch signal intensities were normalized by setting the spectral baseline to 0 and the height of the first order Si band at 520 cm^{-1} to 1. The post-etch spectra were also scaled (blue line) so that the G band maxima and neighboring baselines matched those of the pre-etch spectra. The 2D band profile for the 532 nm spectra was not obtained.

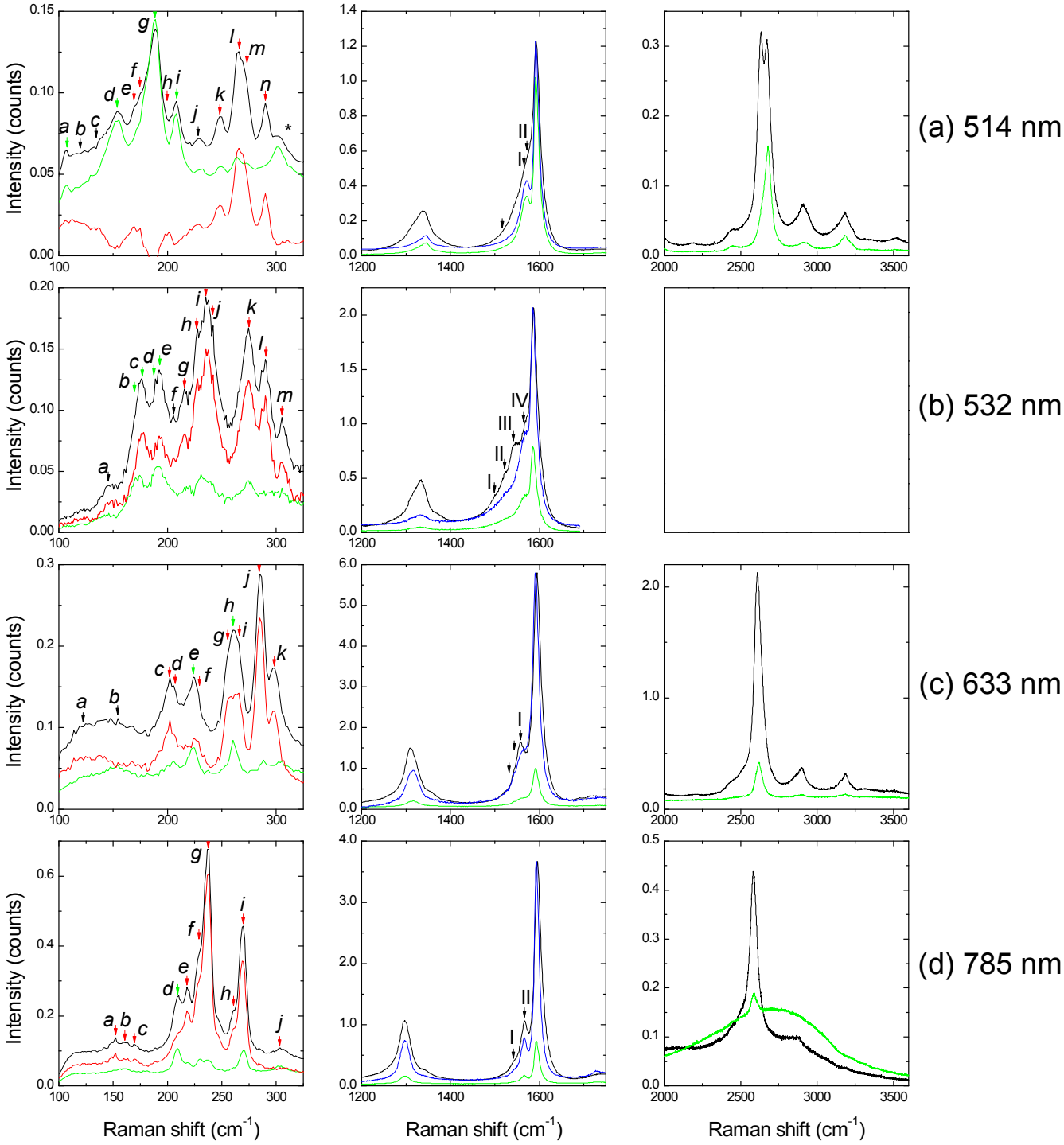

Figure S11. *Ex situ* Raman spectra of pre- (black) and post-etched (green) sample performed with (a) 514 nm, (b) 532 nm, (c) 633 nm, and (d) 785 nm laser lines. The sample was etched at 400°C. Spectra above 1692 cm^{-1} were not collected using the 532 nm laser line. The difference between the pre- and

post-etch spectra is shown in red. Blue spectra shows the scaled post-etch spectra (see text). Asterisks indicate peaks originating from Si/SiO_2.

As we shall describe, these spectra show the rapid etching of E_{11}^M, E_{11}^S, E_{22}^S nanotubes versus comparatively resistant E_{33}^S and E_{44}^S nanotubes in way that cannot be solely explained by diameter dependence. In Table S3, the labelled RBM peaks in Figure S11 are chirality/type assigned using the Models described in Section 1 of the SI. Likewise G- assignment is tabulated in Table S4. Sample Kataura plots using $C_e = 0.046$ nm^{-2} are shown for each of the four laser lines in Figures S12-S15. Again, Kataura plots are obtained using data from R. Saito's Exciton Kataura Plot page (i.e. http://flex.phys.tohoku.ac.jp/eii/).[1, 2] Individual RBMs were indicated as being resistant (green arrow, dotted line) or non-resistant (red arrow, dotted line) to etching based on the relative intensity change before and after etching.

For the 514 nm spectra, the high intensity *d*, *g*, and *i* peaks have undergone little or no etching when compared to the almost totally etched peaks *k* to *n*. However, the low intensity *b*, *c*, *e*, *f*, and *h* peaks also etch faster than the *d*,*g*, and *i* peaks despite their varying diameters. From the Kataura plot we see that the transition between metallic E_{11}^M and semiconducting E_{22}^S species occurs starting at peaks *h* or *g*. Therefore, despite probably being a E_{11}^M nanotube, peak *i* surprisingly etches slowly. One possible assignment for this peak is the high chiral angle (8,8) nanotube, but this is again surprising since higher chiral angle nanotubes are expected to etch more rapidly.[13, 14]

The pre-etch G band of the 514 nm spectra contains unresolved G- peaks between 1500-1540 cm^{-1}, probably containing contributions from the resonant E_{11}^M species. RBM peaks l and m are expected to contribute peaks close to 1540-1550 cm^{-1}, although these peaks are not distinctly visible.

The two most intense G- that persist after etching are peaks II and its shoulder peak I; these correspond nicely with the resistive RBMs at peaks *d* and *g*.

After etching, the D band upshifts from 1338 cm^{-1} to 1344 cm^{-1}, perhaps indicating a minor change in the amount of bundling in the sample or in defective carbon after etching. Notably the 2D peak changes from two peaks centered at 2635 cm^{-1} and 2670 cm^{-1}, to one peak at 2679 cm^{-1}. Different species of SWNT have different 2D peak structures, including doublets.[15] The change in 2D from doublet to single peak may originate in the change in tube distribution.

The 532 nm spectra is similar to previously shown *in situ* data. The RBMs labelled *b* to *e* are resistant compared to the other peaks, while corresponding with the onset of E_{33}^{S} nanotubes in the Kataura plot. The metallic RBMs at peaks *g* to *j* etch as much as the smaller diameter E_{22}^{S} species *k* to *m*. The low intensity RBM-*a* also appears to etch despite being of large diameter, while peak *c* appears to etch slightly more than the smaller diameter peak *e*.

Poorly resolved G- peaks close to peak I should be generated with metallic RBMs such as RBMs *i* and *j*. Likewise peak II can be attributed to metal peaks close to RBM-*g*. The other indicated G-peaks III and IV correspond to the E_{22}^{S} and E_{33}^{S} peaks respectively. This assignment makes sense, since the peak IV appears far more resistant than peak III, and the larger diameter E_{33}^{S} peaks are generally more resistant than the E_{22}^{S} peaks.

The D band at 1333 cm^{-1} does not shift following etching.

The 633 nm RBMs are fairly unstable, with the two most comparatively resistant RBMs being peaks *e* and *h*, which are semiconductors. All the labelled peaks after (and including) peak *e* appear to correspond to small diameter E_{22}^{S}, with peaks *b* to *c* being likely metallics. Large diameter semiconducting peaks before 150 cm^{-1} are not clearly visible. We see that the larger diameter peak *c, a*

metallic tube, does etch faster than peak *e*, a semiconductor, consistent again with the idea that nanotube type may directly affect etching rate. Peak *h* is flanked by two nanotubes of similar diameter that etch more than peak *h* itself indicating indicated a strong chiral dependence on etching rates for these tubes even though they are the both semiconductors.

There are again unresolved low frequency G- peaks present, such that we expect RMBs *c*, *j* and *h* to have G- peaks close to 1532 cm^{-1}, 1543 cm^{-1} and 1548 cm^{-1}. The somewhat resistant peak I corresponds well with the somewhat resistant RBM *e*.

The associated D band experiences a 5 cm^{-1} upshift from 1310 cm^{-1} after etching, while the 2D experiences a comparable shift from 2610 cm^{-1} to 2621 cm^{-1}.

The 785 nm RBMs also experience significant loss, with peaks *i* and *j* corresponding to E_{11}^{S} species, peaks *d* to *h* being E_{22}^{S} nanotubes, with peaks *a* to *c* being either E_{22}^{S} or E_{11}^{M}. The most resistant peak is RBM *d*, a semiconductor. The small diameter RBM *i* appears to be somewhat more resistant than peak *g*, possibly because peak *i* probably corresponds to a low chiral angle species.

In terms of the G- peaks, peak *g* should match with a G- at 1555 cm^{-1}, while peak *i* should have a peak at 1547 cm^{-1} (perhaps corresponding to peak I), both of which may be present as weak peaks in the pre-etch sample. The persistent semiconducting peak II corresponds well with RBM *d*, as expected.

Neither the D band at 1298 cm^{-1} or the 2D band at 2584 cm^{-1} experience major shifts to frequency or lineshape following etching. The broad hill between 2000-3250 cm^{-1} is attributed to the sample background.

Table S3a. Radial Breathing Mode assignments for E_{LASER} = 514 nm (2.41 eV)

		Extreme Case 1		Most Likely Assignment		Extreme Case 2	
Peak Label	Raman Shift (cm^{-1})	Diameter (nm) Model 1 A = 227 $nm \cdot cm^{-1}$, B = 0 cm^{-1}	Assignment Model 1 A = 227 $nm \cdot cm^{-1}$, B = 0 cm^{-1}	Diameter (nm) Model 2 C_e = 0.046 nm^{-2}	Assignment Model 2 C_e = 0.046 nm^{-2}	Diameter (nm) Model 3 A = 248 $nm \cdot cm^{-1}$, B = 0 cm^{-1}	Assignment Model 3 A = 248 $nm \cdot cm^{-1}$, B = 0 cm^{-1}
a	107	2.12	S	2.38	S	2.32	S
b	120	1.89	S	2.07	S	2.07	S
c	134	1.69	S	1.82	S	1.85	S
d	154	1.47	S	1.55	S	1.61	S
e	170	1.34	S (E_{33}^S) or M (E_{11}^M)	1.39	S (E_{33}^S) or M (E_{11}^M)	1.46	S
f	174	1.30	S (E_{33}^S) or M (E_{11}^M)	1.36	S (E_{33}^S) or M (E_{11}^M)	1.43	S (E_{33}^S) or M (E_{11}^M)
g	189	1.20	M (E_{11}^M)	1.24	S (E_{33}^S) or M (E_{11}^M)	1.31	S (E_{33}^S) or M (E_{11}^M)
h	200	1.14	M (E_{11}^M)	1.17	M (E_{11}^M)	1.24	S (E_{33}^S) or M (E_{11}^M)
i	208	1.09	M (E_{11}^M)	1.12	M (E_{11}^M)	1.19	M (E_{11}^M)
j	227	1.00	M (E_{11}^M)	1.02	M (E_{11}^M)	1.09	M (E_{11}^M)
k	248	0.92	S (E_{22}^S) or M (E_{11}^M)	0.93	M (E_{11}^M)	1.00	M (E_{11}^M)
l	266	0.85	S (E_{22}^S) or M (E_{11}^M)	0.87	S (E_{22}^S) or M (E_{11}^M)	0.93	M (E_{11}^M)
m	270	0.84	S (E_{22}^S) or M (E_{11}^M)	0.85	S (E_{22}^S) or M (E_{11}^M)	0.92	S (E_{22}^S) or M (E_{11}^M)
n	290	0.78	(9,2), (6,5) ? S (E_{22}^S)	0.79	(9,2) S (E_{22}^S)	0.86	S (E_{22}^S) or M (E_{11}^M)

Table S3b. Radial Breathing Mode assignments for E_{LASER} = 532 nm (2.33 eV)

			Extreme Case 1		Most Likely Assignment		Extreme Case 2	
Peak Label (Fig S10b)	Corres-ponding Peak Label used in Fig 3	Raman Shift (cm^{-1})	Diameter (nm) Model 1 A = 227 $nm \cdot cm^{-1}$, B = 0 cm^{-1}	Assignment Model 1 A = 227 $nm \cdot cm^{-1}$, B = 0 cm^{-1}	Diameter (nm) Model 2 C_e = 0.046 nm^{-2}	Assignment Model 2 C_e = 0.046 nm^{-2}	Diameter (nm) Model 3 A = 248 $nm \cdot cm^{-1}$, B = 0 cm^{-1}	Assignment Model 3 A = 248 $nm \cdot cm^{-1}$, B = 0 cm^{-1}
a	*a*	146	1.55	S	1.65	S	1.70	S
b	-	170	1.34	S (E_{33}^S) or M (E_{11}^M)	1.39	S (E_{33}^S) or M (E_{11}^M)	1.46	S
c	*b*	177	1.28	S (E_{33}^S) or M (E_{11}^M)	1.33	S (E_{33}^S) or M (E_{11}^M)	1.40	S (E_{33}^S) or M (E_{11}^M)
d	-	189	1.20	S (E_{33}^S) or M (E_{11}^M)	1.24	S (E_{33}^S) or M (E_{11}^M)	1.31	S (E_{33}^S) or M (E_{11}^M)
e	*c*	193	1.18	S (E_{33}^S) or M (E_{11}^M)	1.22	S (E_{33}^S) or M (E_{11}^M)	1.28	S (E_{33}^S) or M (E_{11}^M)
f	-	205	1.11	(10,7) M (E_{11}^M)	1.14	(10,7) M (E_{11}^M)	1.21	(9,9) M (E_{11}^M)
g	*d*	215	1.06	(8,8) or (12,3) M (E_{11}^M)	1.08	(8,8) or (12,3) M (E_{11}^M)	1.15	(10,7) M (E_{11}^M)
h	*e*	227	1.00	(9,6) M (E_{11}^M)	1.02	(9,6) M (E_{11}^M)	1.09	(8,8) or (12,3) M (E_{11}^M)
i	*f?*	236	0.96	(10,4) M (E_{11}^M)	0.98	(10,4) M (E_{11}^M)	1.05	(13,1) M (E_{11}^M)
j	*f?*	240	0.95	(11,2) M (E_{11}^M)	0.97	(11,2) M (E_{11}^M)	1.03	(9,6) M (E_{11}^M)
k	*g*	275	0.83	(8,4) S (E_{22}^S)	0.84	(8,4) S (E_{22}^S)	0.90	(11,1) S (E_{22}^S)
l	*h*	290	0.78	(9,2) S (E_{22}^S)	0.79	(9,2) S (E_{22}^S)	0.86	(8,4) S (E_{22}^S)
m	*i*	306	0.74	(6,5) S (E_{22}^S)	0.75	(6,5) S (E_{22}^S)	0.81	(9,2) S (E_{22}^S)

Table S3c. Radial Breathing Mode assignments for E_{LASER} = 633 nm (1.96 eV)

		Extreme Case 1		Most Likely Assignment		Extreme Case 2	
Peak Label	Raman Shift (cm^{-1})	Diameter (nm) Model 1 A = 227 $nm \cdot cm^{-1}$, B = 0 cm^{-1}	Assignment Model 1 A = 227 $nm \cdot cm^{-1}$, B = 0 cm^{-1}	Diameter (nm) Model 2 C_e = 0.046 nm^{-2}	Assignment Model 2 C_e = 0.046 nm^{-2}	Diameter (nm) Model 3 A = 248 $nm \cdot cm^{-1}$, B = 0 cm^{-1}	Assignment Model 3 A = 248 $nm \cdot cm^{-1}$, B = 0 cm^{-1}
a	121	1.88	S	2.05	S	2.05	S
b	154	1.47	S (E_{33}^S) or M (E_{11}^M)	1.55	S (E_{33}^S) or M (E_{11}^M)	1.61	S (E_{33}^S) or M (E_{11}^M)
c	202	1.12	M (E_{11}^M)	1.16	M (E_{11}^M)	1.23	M (E_{11}^M)
d	206	1.10	M (E_{11}^M)	1.13	M (E_{11}^M)	1.20	M (E_{11}^M)
e	224	1.01	S (E_{22}^S)	1.04	S (E_{22}^S)	1.11	M (E_{11}^M)
f	228	1.00	S (E_{22}^S)	1.02	S (E_{22}^S)	1.09	S (E_{22}^S) or M (E_{11}^M)
g	257	0.88	S (E_{22}^S)	0.90	S (E_{22}^S)	0.96	S (E_{22}^S)
h	260	0.87	S (E_{22}^S)	0.89	S (E_{22}^S)	0.95	S (E_{22}^S)
i	265	0.86	S (E_{22}^S)	0.87	S (E_{22}^S)	0.94	S (E_{22}^S)
j	285	0.80	(7,5) or (8,3) S (E_{22}^S)	0.81	(7,5) S (E_{22}^S)	0.87	S (E_{22}^S)
k	298	0.76	(8,3) or (9,1) S (E_{22}^S)	0.77	(8,3) S (E_{22}^S)	0.83	(7,5) S (E_{22}^S)

Table S3d. Radial Breathing Mode assignments for E_{LASER} = 785 nm (1.58 eV)

		Extreme Case 1		Most Likely Assignment		Extreme Case 2	
Peak Label	Raman Shift (cm^{-1})	Diameter (nm) Model 1 A = 227 $nm \cdot cm^{-1}$, B = 0 cm^{-1}	Assignment Model 1 A = 227 $nm \cdot cm^{-1}$, B = 0 cm^{-1}	Diameter (nm) Model 2 C_e = 0.046 nm^{-2}	Assignment Model 2 C_e = 0.046 nm^{-2}	Diameter (nm) Model 3 A = 248 $nm \cdot cm^{-1}$, B = 0 cm^{-1}	Assignment Model 3 A = 248 $nm \cdot cm^{-1}$, B = 0 cm^{-1}
a	152	1.49	S (E_{22}^S) or M (E_{11}^M)	1.58	S (E_{22}^S) or M (E_{11}^M)	1.63	S (E_{22}^S) or M (E_{11}^M)
b	159	1.43	S (E_{22}^S) or M (E_{11}^M)	1.50	S (E_{22}^S) or M (E_{11}^M)	1.56	S (E_{22}^S) or M (E_{11}^M)
c	170	1.34	S (E_{22}^S)	1.39	S (E_{22}^S) or M (E_{11}^M)	1.46	S (E_{22}^S) or M (E_{11}^M)
d	210	1.08	S (E_{22}^S)	1.11	S (E_{22}^S)	1.18	S (E_{22}^S)
e	218	1.04	S (E_{22}^S)	1.07	S (E_{22}^S)	1.14	S (E_{22}^S)
f	230	0.99	S (E_{22}^S)	1.01	S (E_{22}^S)	1.08	S (E_{22}^S)
g	237	0.96	S (E_{22}^S)	0.98	S (E_{22}^S)	1.05	S (E_{22}^S)
h	261	0.87	S (E_{22}^S) or S (E_{11}^S)	0.89	(9,4) S (E_{22}^S)	0.95	S (E_{22}^S)
i	270	0.84	S (E_{11}^S)	0.85	(11,0) S (E_{11}^S)	0.92	S (E_{22}^S)
j	303	0.75	(8,3) or (9,1) S (E_{11}^S)	0.76	(8,3) or (9,1) S (E_{11}^S)	0.82	S (E_{11}^S)

S=semiconducting, M=metallic

Label	Raman Shift (cm^{-1})	Diameter (nm)	Assignment	Comments
E_{LASER} = 514 nm (2.41 eV)				
I	~1565 cm^{-1}	~1.23 nm?	S	Corresponds to peak *g*
II	1572 cm^{-1}	1.60 nm	S	Corresponds to peak *d*
E_{LASER} = 532 nm (2.33 eV)				
I	~1499 cm^{-1}	~0.94 nm	M	Corresponds to peaks *i*, *j*
II	~1521 cm^{-1}	~1.06 nm	M	Corresponds to peak *g*
III	~1542 cm^{-1}	~0.80 nm	S	Peaks 1542 cm^{-1} and 1545 cm^{-1} correspond to peaks *m* and *l*, respectively
IV	~1565 cm^{-1}	~1.25 nm	S	Peaks 1565 cm^{-1} and 1567 cm^{-1} correspond to peaks *e* (*d*) and *c* (*b*), respectively
E_{LASER} = 633 nm (1.96 eV)				
I	~1558 cm^{-1}	~1.04 nm	S	Corresponds to peak *e*
E_{LASER} = 785 nm (1.58 eV)				
I	~1542 cm^{-1}	~0.80 nm (~1.27 nm)	S(M)	Corresponds to peaks *i* and *j*?
II	~1565 cm^{-1}	~1.3 nm	S	Peak 1561 cm^{-1} corresponds to peak *d*

Table S4. G- band assignments

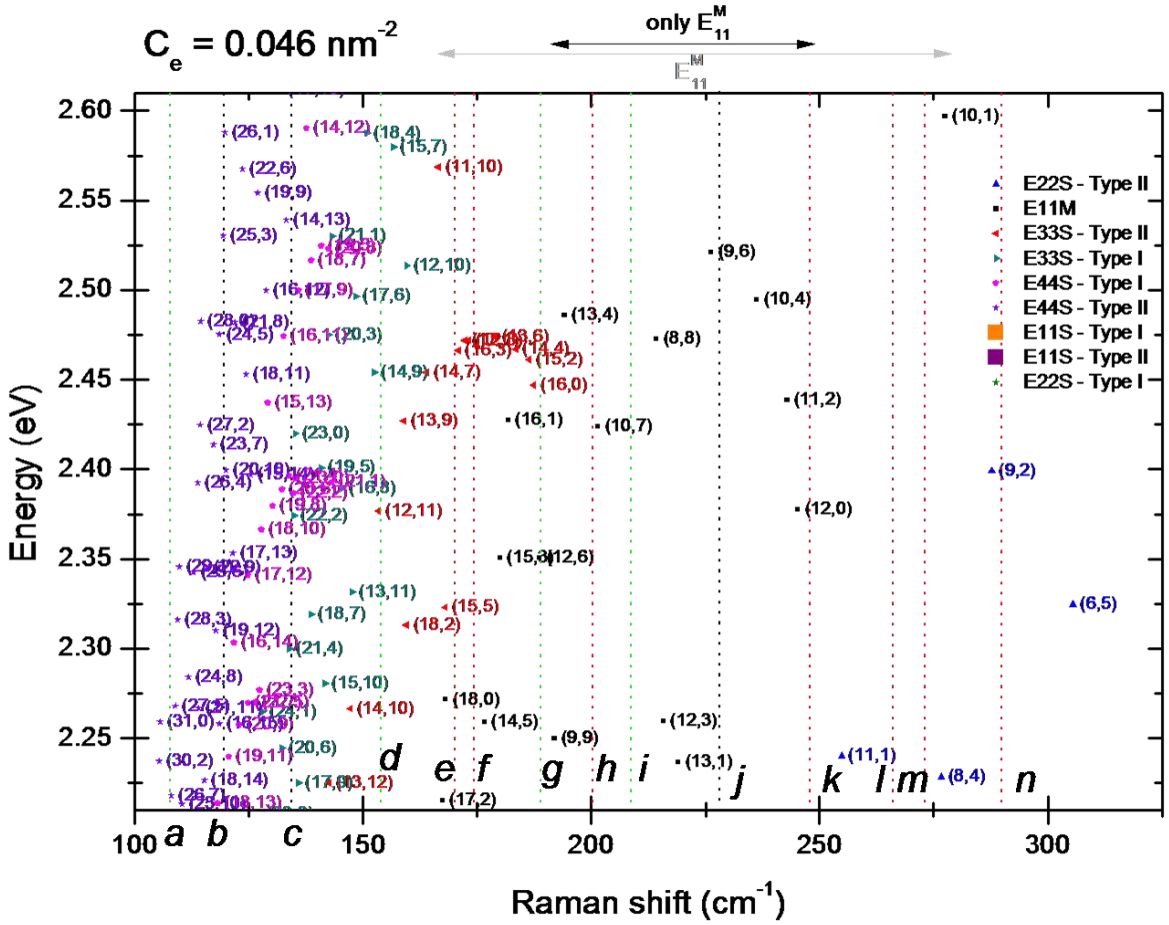

Figure S12. Kataura plot frequencies for E_{LASER} = 514 nm calculated using the expression $\omega_{RBM} = (227/d_t)\sqrt{1+C_e \cdot d_t^2}$, where C_e = 0.046 nm^{-2}. Different (n,m) values are present. Only diameters larger than 0.7 nm are shown. Dotted lines represent observed RBMs shown in Figure S11(a). Points are labelled by the band they originate in. Semiconducting, metallic and mixed regions are delineated with respect to the labels along the top axis, indicating the band of origin (e.g. E_{11}^M is metallic, E_{22}^S is semiconducting) along the top horizontal axis.

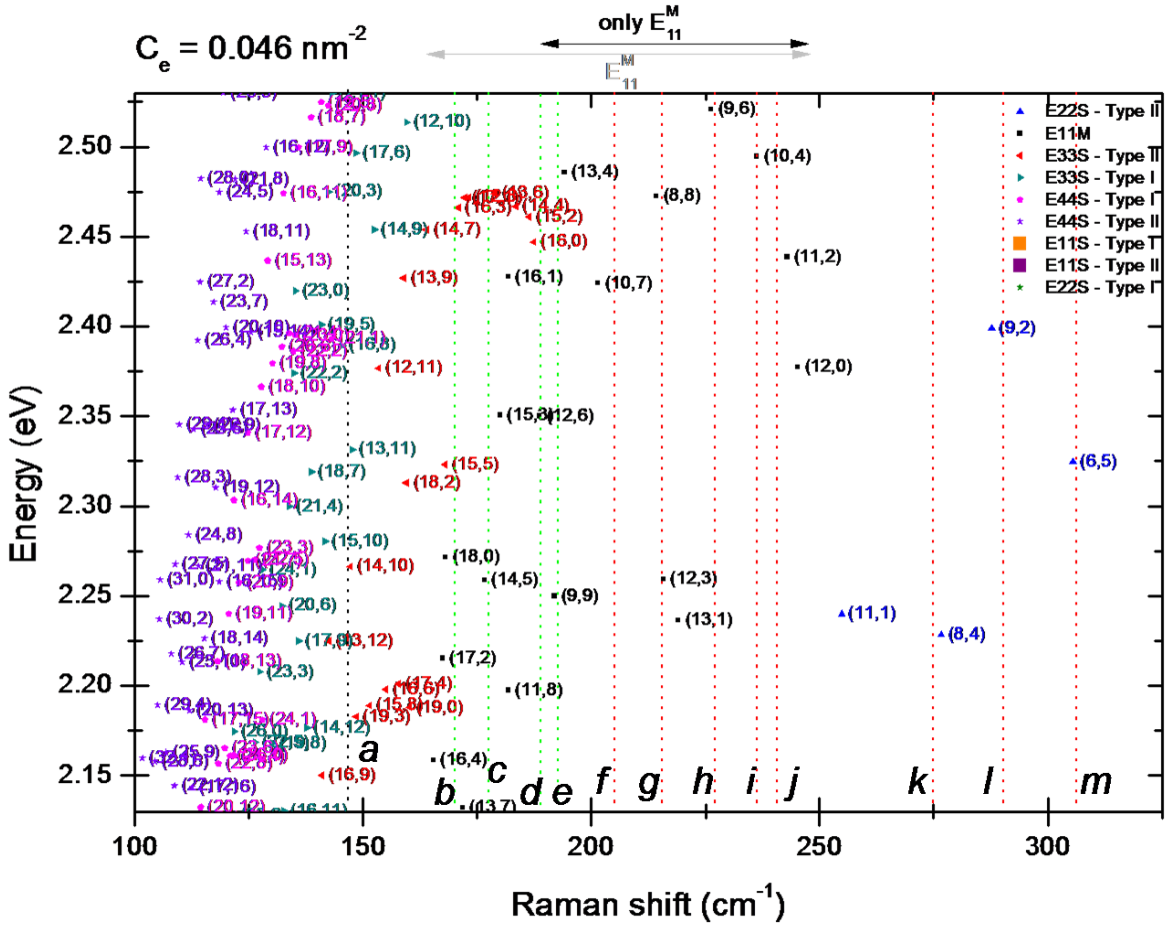

Figure S13. Kataura plot frequencies for E_{LASER} = 532 nm calculated using the expression $\omega_{RBM} = (227/d_t)\sqrt{1+C_e \cdot d_t^2}$, where C_e = 0.046 nm^{-2}. Different (n,m) values are present. Only diameters larger than 0.7 nm are shown. Dotted lines represent observed RBMs shown in Figure S11(b). Points are labelled by the band they originate in. Semiconducting, metallic and mixed regions are delineated with respect to the labels along the top axis, indicating the band of origin (e.g. E_{11}^M is metallic, E_{22}^S is semiconducting) along the top horizontal axis.

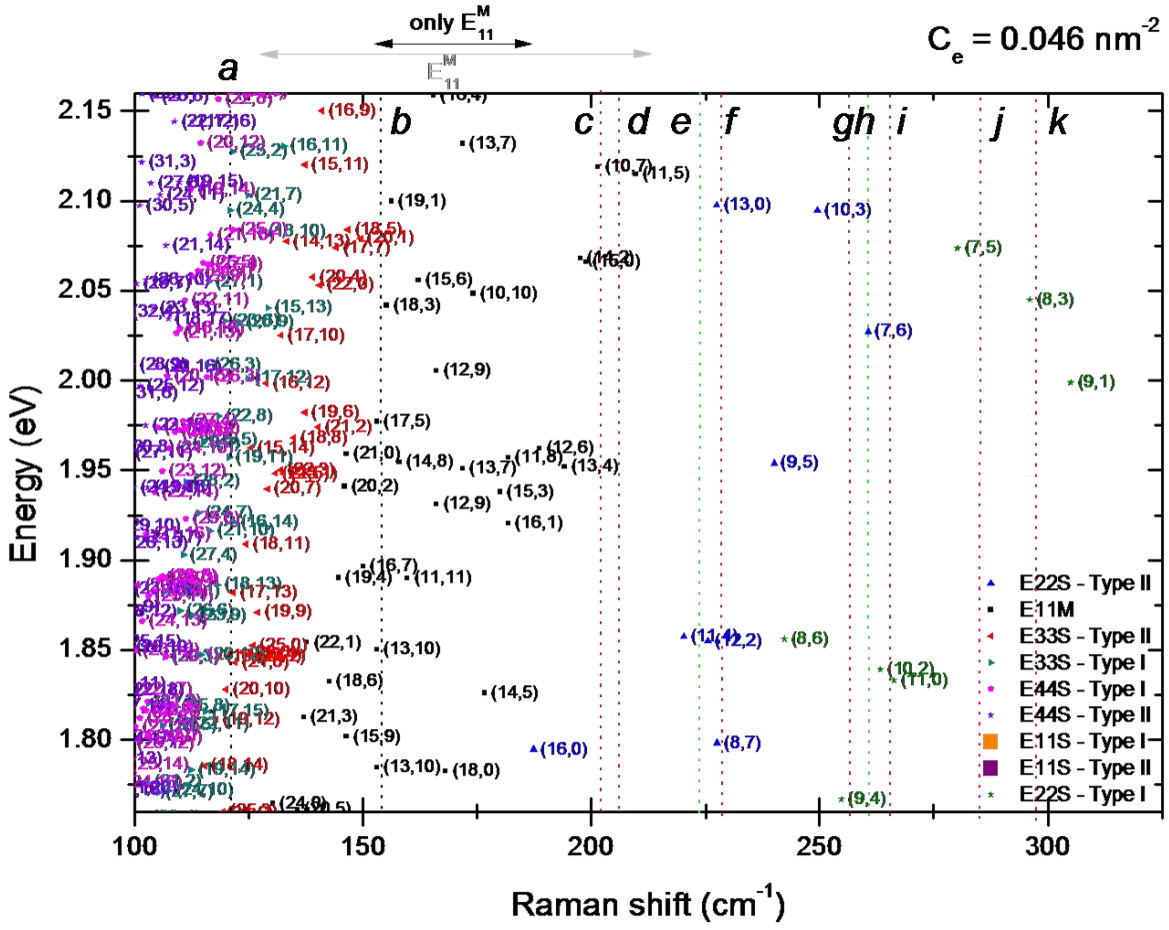

Figure S14. Kataura plot frequencies for E_{LASER} = 633 nm calculated using the expression $\omega_{RBM} = (227/d_t)\sqrt{1+C_e \cdot d_t^2}$, where C_e = 0.046 nm^{-2}. Different (n,m) values are present. Only diameters larger than 0.7 nm are shown. Dotted lines represent observed RBMs shown in Figure S11(c). Points are labelled by the band they originate in. Semiconducting, metallic and mixed regions are delineated with respect to the labels along the top axis, indicating the band of origin (e.g. E_{11}^M is metallic, E_{22}^S is semiconducting) along the top horizontal axis.

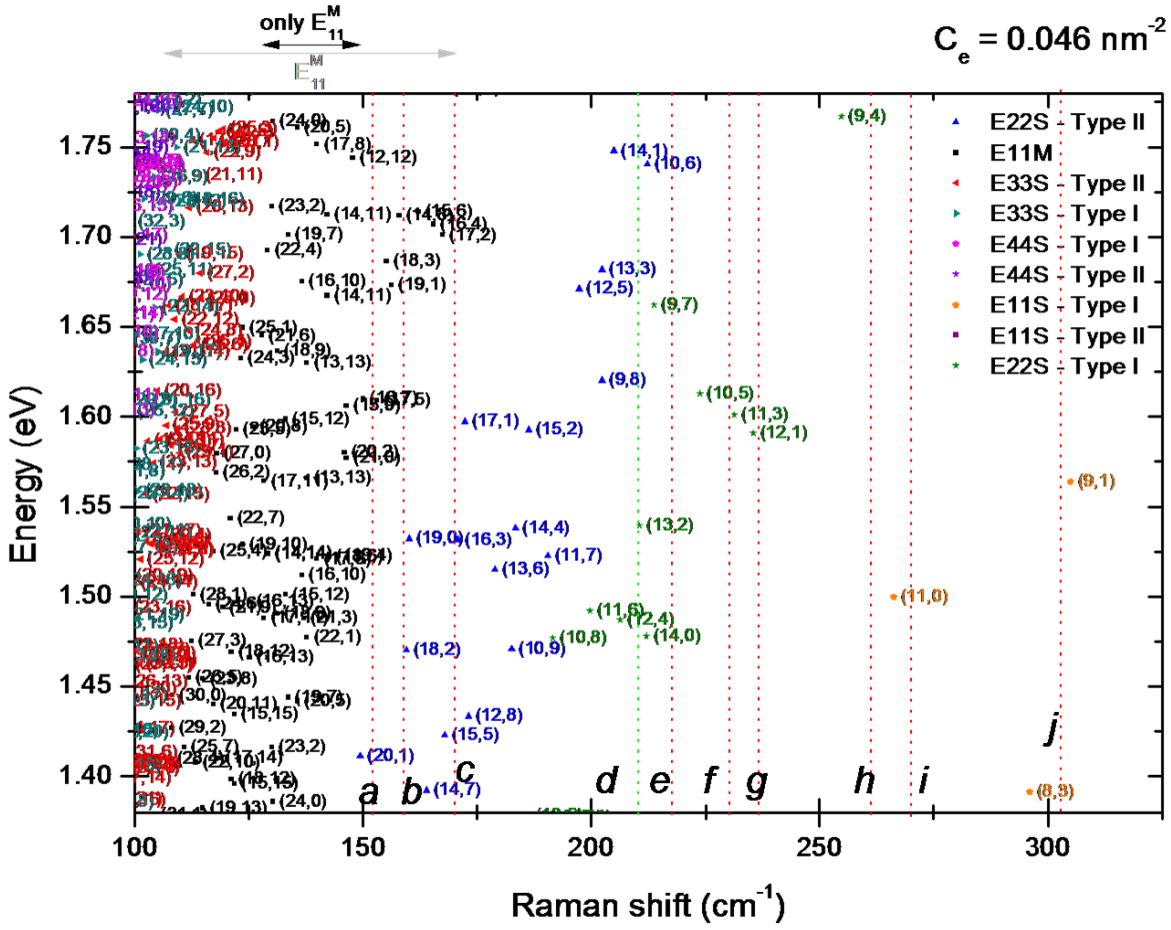

Figure S15. Kataura plot frequencies for E_{LASER} = 785 nm calculated using the expression $\omega_{RBM} = (227/d_t)\sqrt{1+C_e \cdot d_t^2}$, where C_e = 0.046 nm^{-2}. Different (n,m) values are present. Only diameters larger than 0.7 nm are shown. Dotted lines represent observed RBMs shown in Figure S11(d). Points are labelled by the band they originate in. Semiconducting, metallic and mixed regions are delineated with respect to the labels along the top axis, indicating the band of origin (e.g. E_{11}^M is metallic, E_{22}^S is semiconducting) along the top horizontal axis.

8. Background correction illustration

For a given peak, the integrated peak area is obtained by subtracting the trapezoidal baseline. See Figure S16 and ref. 15 for a complete description.[16]

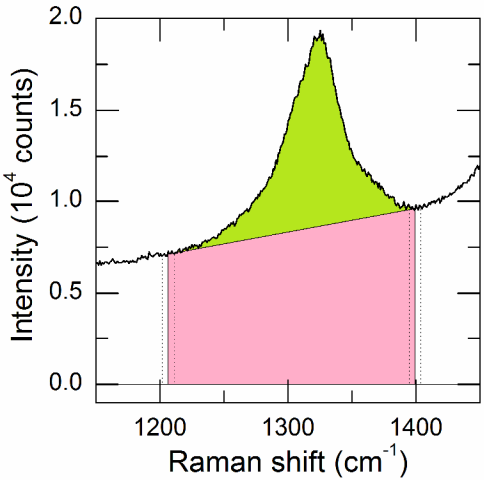

Figure S16. Integrated area (green) and baseline trapezoid (pink) are shown for typical D band at T = 350 °C.

9. Comparison of D band lineshape

Figure S17 shows typical D band spectra before and after etching at room temperature, and during etching at T = 550 °C at different times, with all D band intensities normalized to 1. The sample was etched in air for 42 minutes.

Apart from signal loss incurred from the destruction of sp^3 carbon, there is no clear change in D band structure throughout the entire etching process.

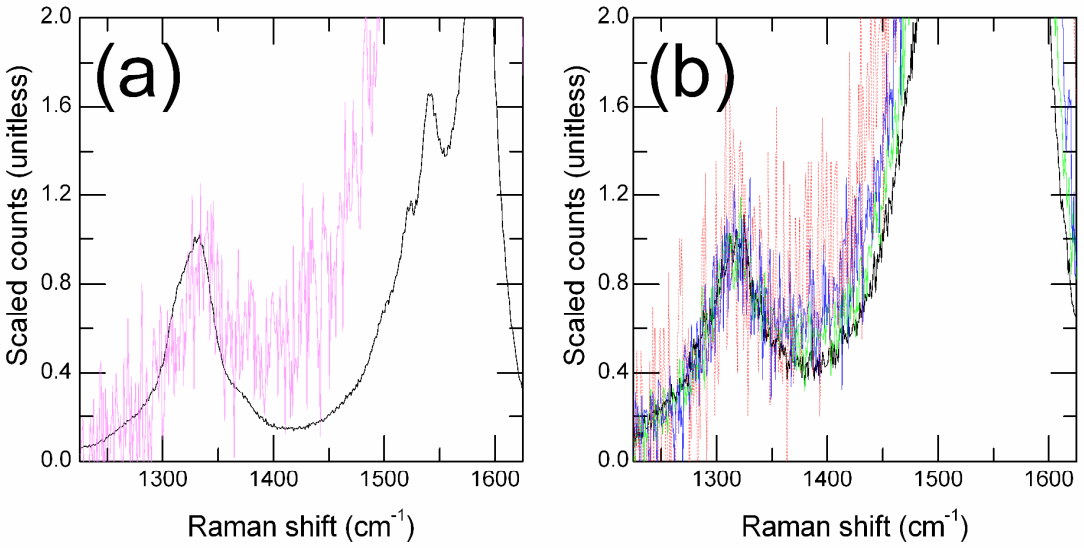

Figure S17. (a) Scaled D band at room temperature before (black) and after etching (magenta). (b) Scaled D band during air etching at T = 550 °C for etching times t = 0 (black), t = 3 min (green), t = 6 min (blue), and t = 12 min (red).

10. XPS spectra

The X-ray photoelectron spectroscopy (XPS) spectrum of a typical pre-etch sample was taken using a PHI 5500 system with an aluminum x-ray source, as shown in Figure S16. The asymmetric peak at ~ 284.3 eV corresponds to the 1s photoelectron line of carbon, typical of sp^2 hybridization.[17-20] The peak is relatively narrow (i.e. full width at half maximum is ~0.92 eV) with no pronounced doublet structure, suggesting that sp^3 content is low compared to sp^2 content. This is consistent with the presence of CNTs with relatively few defects and a low amount of amorphous carbon.[17-20]

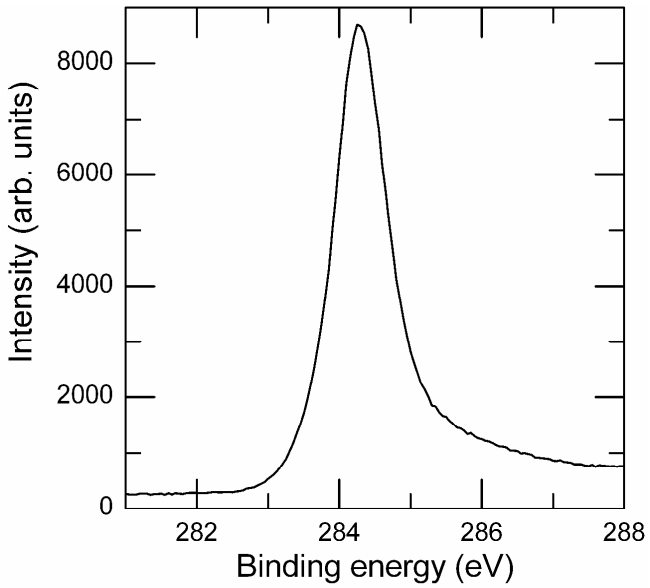

Figure S18. XP spectrum of the C 1s region for a pre-etch sample.

REFERENCES

1. Nugraha, A. R. T.; Saito, R.; Sato, K.; Araujo, P. T.; Jorio, A.; Dresselhaus, M. S. Dielectric Constant Model for Environmental Effects on the Exciton Energies of Single Wall Carbon Nanotubes. *Appl. Phys. Lett.* **2010***, 97*, 091905-3.

2. Sato, K.; Saito, R.; Jiang, J.; Dresselhaus, G.; Dresselhaus, M. S. Discontinuity in the Family Pattern of Single-Wall Carbon Nanotubes. *Phys. Rev. B* **2007***, 76*, 195446.

3. Telg, H.; Duque, J. G.; Staiger, M.; Tu, X.; Hennrich, F.; Kappes, M. M.; Zheng, M.; Maultzsch, J.; Thomsen, C.; Doorn, S. K. Chiral Index Dependence of the G+ and G- Raman Modes in Semiconducting Carbon Nanotubes. *ACS Nano* **2012***, 6*, 904-911.

4. Araujo, P. T.; Pesce, P. B. C.; Dresselhaus, M. S.; Sato, K.; Saito, R.; Jorio, A. Resonance Raman Spectroscopy of the Radial Breathing Modes in Carbon Nanotubes. *Phys. E* **2010***, 42*, 1251-1261.

5. Saito, R.; Fantini, C.; Jiang, J. In *Excitonic States and Resonance Raman Spectroscopy of Single-Wall Carbon Nanotubes;* Jorio, A., Dresselhaus, G. and Dresselhaus, M. S., Eds.; **Carbon Nanotubes: Advanced Topics in the Synthesis, Structure, Properties and Applications (Topics in Applied Physics)**; Springer-Verlag Berlin Heidelberg: Berlin, 2008; Vol. 111, pp 251.

6. Fantini, C.; Jorio, A.; Souza, M.; Strano, M. S.; Dresselhaus, M. S.; Pimenta, M. A. Optical Transition Energies for Carbon Nanotubes from Resonant Raman Spectroscopy: Environment and Temperature Effects. *Phys. Rev. Lett.* **2004***, 93*, 147406.

7. Bachilo, S. M.; Strano, M. S.; Kittrell, C.; Hauge, R. H.; Smalley, R. E.; Weisman, R. B. Structure-Assigned Optical Spectra of Single-Walled Carbon Nanotubes. *Science* **2002***, 298*, 2361-2366.

8. Araujo, P. T.; Fantini, C.; Lucchese, M. M.; Dresselhaus, M. S.; Jorio, A. The Effect of Environment on the Radial Breathing Mode of Supergrowth Single Wall Carbon Nanotubes. *Appl. Phys. Lett.* **2009***, 95*, 261902-3.

9. Jorio, A.; Souza Filho, A. G.; Dresselhaus, G.; Dresselhaus, M. S.; Swan, A. K.; Unlu, M. S.; Goldberg, B. B.; Pimenta, M. A.; Hafner, J. H.; Lieber, C. M.*, et al.* G-Band Resonant Raman Study of 62 Isolated Single-Wall Carbon Nanotubes. *Phys. Rev. B* **2002***, 65*, 155412.

10. Dresselhaus, M. S.; Jorio, A.; Hofmann, M.; Dresselhaus, G.; Saito, R. Perspectives on Carbon Nanotubes and Graphene Raman Spectroscopy. *Nano Lett.* **2010***, 10*, 751-758.

11. Bachilo, S. M.; Balzano, L.; Herrera, J. E.; Pompeo, F.; Resasco, D. E.; Weisman, R. B. Narrow (n,m)-Distribution of Single-Walled Carbon Nanotubes Grown using a Solid Supported Catalyst. *J. Am. Chem. Soc.* **2003***, 125*, 11186-11187.

12. Jorio, A.; Pimenta, M. A.; Filho, A. G. S.; Saito, R.; Dresselhaus, G.; Dresselhaus, M. S. Characterizing Carbon Nanotube Samples with Resonance Raman Scattering. *New J. Phys.* **2003***, 5*, 139.

13. Miyata, Y.; Kawai, T.; Miyamoto, Y.; Yanagi, K.; Maniwa, Y.; Kataura, H. Chirality-Dependent Combustion of Single-Walled Carbon Nanotubes. *J. Phys. Chem. C* **2007***, 111*, 9671-9677.

14. Kawai, T.; Miyamoto, Y. Chirality-Dependent C-C Bond Breaking of Carbon Nanotubes by Cyclo-Addition of Oxygen Molecule. *Chem. Phys. Lett.* **2008***, 453*, 256-261.

15. Dresselhaus, M. S.; Dresselhaus, G.; Saito, R.; Jorio, A. Raman Spectroscopy of Carbon Nanotubes. *Phys. Rep.* **2005***, 409*, 47-99.

16. Li-Pook-Than, A.; Lefebvre, J.; Finnie, P. Phases of Carbon Nanotube Growth and Population Evolution from *in Situ* Raman Spectroscopy during Chemical Vapor Deposition. *J. Phys. Chem. C* **2010***, 114*, 11018-11025.

17. Haerle, R.; Riedo, E.; Pasquarello, A.; Baldereschi, A. Sp^{2}/sp^{3} Hybridization Ratio in Amorphous Carbon from C 1s Core-Level Shifts: X-Ray Photoelectron Spectroscopy and First-Principles Calculation. *Phys. Rev. B* **2001***, 65*, 045101.

18. Nikitin, A.; Ogasawara, H.; Mann, D.; Denecke, R.; Zhang, Z.; Dai, H.; Cho, K.; Nilsson, A. Hydrogenation of Single-Walled Carbon Nanotubes. *Phys. Rev. Lett.* **2005***, 95*, 225507.

19. Kundu, S.; Wang, Y.; Xia, W.; Muhler, M. Thermal Stability and Reducibility of Oxygen-Containing Functional Groups on Multiwalled Carbon Nanotube Surfaces: A Quantitative High-Resolution XPS and TPD/TPR Study. *J. Phys. Chem. C* **2008***, 112*, 16869-16878.

20. Estrade-Szwarckopf, H. XPS Photoemission in Carbonaceous Materials: A "Defect" Peak Beside the Graphitic Asymmetric Peak. *Carbon* **2004***, 42*, 1713-1721.

4. TRACKING OXIDATION OF SWCNTS BY TWO LASER RAMAN SPECTROSCOPY

Foreword

In this study, we investigate the combustion of SWCNTs in oxygen and carbon dioxide gas using a novel two-laser Raman system. In contrast to Chapter 3, which used CVD nanotubes that I synthesized myself, here the sample type was switched to a laser ablation SWCNT source. This was chosen such that metallic and semiconducting species were separately strongly resonant with one of the two laser lines. Again, *in situ* Raman spectroscopy showed that metallic species etch more rapidly.

Metal and semiconducting species evolution can now be contrasted more easily because the two separate spectra appear distinctly semiconducting and metallic from the onset, and because these two nanotube populations share a similar diameter, with the corresponding RBMs being distinctly visible since they are on separate spectra. We again observed clear evidence of type selectivity, but we found that the degree of type selectivity was limited in the sense that although metallic nanotubes etched more quickly, we were not able to continue to etch to leave only semiconducting nanotubes.

In terms of the decay curves, compared to our single-laser, SWCNT etching study, we again see a biexponential trend across all temperatures, but this time the sp^3 populations are found to decay much faster with a single exponential, while the individual nanotube species decay biexponential, matching the decay of the graphitic species.

Up to the accuracy of our experiment, similar activation energies are obtained for all graphitic species, so the overall etching process for metallic and semiconducting species is likely the same.

In this paper based thesis we reproduce in full the publication entitled "**Observation of the Metallic-Type Selective Etching of Single Walled Carbon Nanotubes by Real-Time in situ Two-Laser Raman Spectroscopy** ", which is cited as **Carbon 2015, 89, Pages 232-241**. The supplementary information is also reproduced and can be found online at http://www.sciencedirect.com/science/article/pii/S0008622315002195

CARBON 89 (2015) 232–241

Available at www.sciencedirect.com

ScienceDirect

journal homepage: www.elsevier.com/locate/carbon

Observation of the metallic-type selective etching of single walled carbon nanotubes by real-time *in situ* two-laser Raman spectroscopy

Andrew Li-Pook-Than [a,b], *Paul Finnie* [b,a,*]

[a] *Department of Physics, University of Ottawa, 150 Louis Pasteur, Ottawa, ON K1N 6N5, Canada*

[b] *Security and Disruptive Technologies Portfolio, National Research Council Canada, 1200 Montreal Road, Ottawa, ON K1A 0R6, Canada*

ARTICLE INFO

Article history:
Received 14 November 2014
Accepted 5 March 2015
Available online 13 March 2015

ABSTRACT

Real time, *in situ* Raman spectroscopy with two simultaneously incident laser excitation wavelengths is used to investigate the dynamics of single-walled carbon nanotube etching. For the source material, nanotubes of diameter ~1.4 nm, a 532 nm laser is resonant with semiconducting nanotubes and a 633 nm laser is resonant with metallic nanotubes. Changes in metallic and semiconducting population are tracked separately and simultaneously. In oxygen, metals consistently etch faster than semiconductors, and all etch rates increase with the process temperature and the defect density in the source material. A similar evolution is observed in carbon dioxide. Simultaneous two-color Raman spectroscopy provides information beyond standard Raman spectroscopy and can be effective as an instantaneous measure of metallicity for nanotubes.

1. Introduction

Single walled carbon nanotubes (SWCNTs) are rolled-up sheets of graphene with nanoscale diameters. Their properties are highly dependent on diameter and chiral angle. In particular, 2/3 of all possible SWCNTs are semiconducting (s-SWCNTs), while the remaining 1/3 are essentially metallic (m-SWCNTs). The actual metal/semiconductor ratio in any as-grown sample will depend on the synthesis method [1–6]. The final product commonly contains both s-SWCNTs and m-SWCNTs. Chiral and type selective synthesis is widely studied, yet synthesis alone has not been able to supply type specific SWCNTs, at least not on a large scale.

When isolated from each other, both s-SWCNTs and m-SWCNTs become more useful for a variety of applications. Applications related to conductivity benefit from m-SWCNT samples, while applications such as transistors or optoelectronics benefit from s-SWCNT samples. So there is a strong incentive to produce samples of one type. Several separation and post-processing techniques have emerged over the past decade. Solution based techniques are among the most popular methods of separation, and are very effective [7–9]. There has also been work investigating the selective burning of SWCNTs using reactive gases [8,10–13]. Since SWCNT growth reactions in chemical vapor deposition take place in the gas phase, one approach would be to use gas phase etching in

* *Corresponding author at:* Security and Disruptive Technologies Portfolio, National Research Council Canada, 1200 Montreal Road, Ottawa, Ontario, K1A 0R6, Canada. Fax: +1 613 990 0202.
E-mail address: Paul.Finnie@nrc-cnrc.gc.ca (P. Finnie).

http://dx.doi.org/10.1016/j.carbon.2015.03.023
0008-6223/

tandem to tailor nanotube distributions [14,15]. Additionally, oxygen removes defective and amorphous carbon from SWCNT samples [16–21]. Mild oxygen etching with chlorine has a role in the removal of metal catalyst impurities from SWCNTs [22,23]. Carbon dioxide gas can also be used as a more mild etchant to etch carbon nanotubes [24,25].

Here, we provide spectroscopic evidence that m-SWCNTs oxidize faster than s-SWCNTs of similar diameter under oxygen. We show this by tracking SWCNT samples with an *in situ* Raman system that is non-standard in that it uses two distinct laser wavelengths simultaneously. The reason this is useful is that for any given laser energy, only a subset of the SWCNT population will be resonant. For large diameter nanotubes (>1 nm) laser wavelengths can be chosen so that one laser is resonant with s-SWCNT species and the other is resonant with m-SWCNT species of essentially the same diameter [26]. This could in principal be any phonon band, but the G band is particularly practical from the point of view of sampling, sensitivity, and because the lineshape is metallicity dependent [26]. Therefore with both lasers we simultaneously obtain, in real time and *in situ*, two distinct sets of Raman spectra that correspond to the two different electronic types. By tracking these spectra during the etching process, we can directly compare differences in how s-SWCNT and m-SWCNT species are being destroyed.

In this work, we assume that the Raman signal is proportional to the abundance of carbon in nanotube form. More specifically, we suppose that the integrated G band intensities for 532 nm and 633 nm accurately represent the abundance of carbon in the form of semiconducting and metallic SWCNTs respectively. (As for metallicity evolution, we effectively make the weaker assumption that the ratio of the two integrated peak intensities represents their relative abundance.) This assumption is reasonable under many situations, but can be compromised by changes in the nature of the nanotubes or their environment. Some effects that could cause deviations from this proportionality include: the changes from air suspension to surface contact [27], changes due to local environment or bundling [28], changes in resonance due to bundling [29], heavy doping [30], or systematic changes in population within each type, which otherwise alter band intensities. As we will see, the data provides some evidence that the assumption remains valid. Such evidence includes the lack of evolution of the lineshape and the lack of evolution in peak ratios for the various SWCNT bands within each color.

In general, *in situ* Raman is well suited to tracking the evolution in SWCNT populations. We previously reported *in situ* Raman evidence for the selective oxidation of metallic SWCNTs in air [31]. However, because this used only a single laser wavelength, diameter and type information were intermixed. *In situ* Raman allows one to directly track the evolution of different electronic properties and defect levels in the sample, while providing kinetic information for specific SWCNT chiralities and different nanocarbons. The use of multiple Raman lines is an improvement over the single line system because it allows for determination of the metallicity at a nearly fixed diameter [32–34]. Here, it is important to highlight that by using two lasers simultaneously, we get an instantaneous measure of the metallicity.

2. Experimental

2.1. Etching gases

SWCNT samples were etched in oxygen gas (i.e., 20.9% O_2, with Ar balance, Air Liquide certified grade) at one atmosphere for process temperatures between 300 and 600 °C. At these temperatures the etching rates are suitable for tracking in real time. Additional experiments were performed with carbon dioxide etchant rather than oxygen at 4.01% CO_2 (with Ar balance, Air Liquide certified grade) also at one atmosphere.

2.2. Sample preparation

We used raw laser ablation soot SWCNTs as source material [35], with tube diameters in the 1.4 nm range. For such nanotubes, semiconducting and metallic types are spectrally well separated with the appropriate choice of laser wavelengths [26]. The raw soot contains not just the SWCNTs, but also graphitic-like "amorphous" carbon deposits.

These SWCNTs were dispersed in anhydrous ethanol, bath sonicated for one hour, and dropcast on to silicon wafers with one micron thermal oxide. The wafers were then cleaved into 3 mm × 3 mm pieces and loaded into a previously described hot-walled reactor (Linkam CCR1100) and gas flow apparatus [31]. The defect density, as determined by the Raman D/G ratio, varied from sample to sample. This proved to be an important factor in etch rates for our material.

2.3. Two-laser Raman spectroscopy

The simultaneous use of two lasers to perform Raman spectroscopy is not standard, but it is straightforward to modify the optical path of a standard micro-Raman setup to do so. The key difference from a standard setup are a dichroic mirror used as a beam combiner and the use of a notch filter for one of the lasers.

A schematic of our two laser Raman system is shown in Fig. 1. A HeNe laser beam (632.8 nm) is sent through a laser line filter (LL), and passed straight through a dichroic filter (DF). Simultaneously, a green diode-pumped solid state (DPSS) laser beam (532 nm) is passed through a laser line filter, reflected off the DF, and joins the same optical path as the red laser. Both lasers pass through a cylindrical lens (CL), are reflected off a beamsplitter (BS1), and are focused by a 20× microscope objective. The light travels through the quartz window of the reactor to illuminate the sample.

The light would be focused were it not for the CL, which defocuses the beam along one axis such that the illumination is an unfocused cylindrical spot (~3000 μm^2), and laser power density across the spot is quite low (i.e., ~1 $\mu W/\mu m^2$ per laser). For reference, the HeNe laser is a fixed 25 mW laser and the Nd:Yag, which was tunable in this range, was set at a power so that the G bands from the two lasers had similar peak intensities. The scattered signals are collected by the objective and pass through BS1 before being filtered by a 532 nm edge filter (EF) and a 633 nm notch filter (NF), thereby removing most of the Rayleigh signal at both laser wavelengths. A

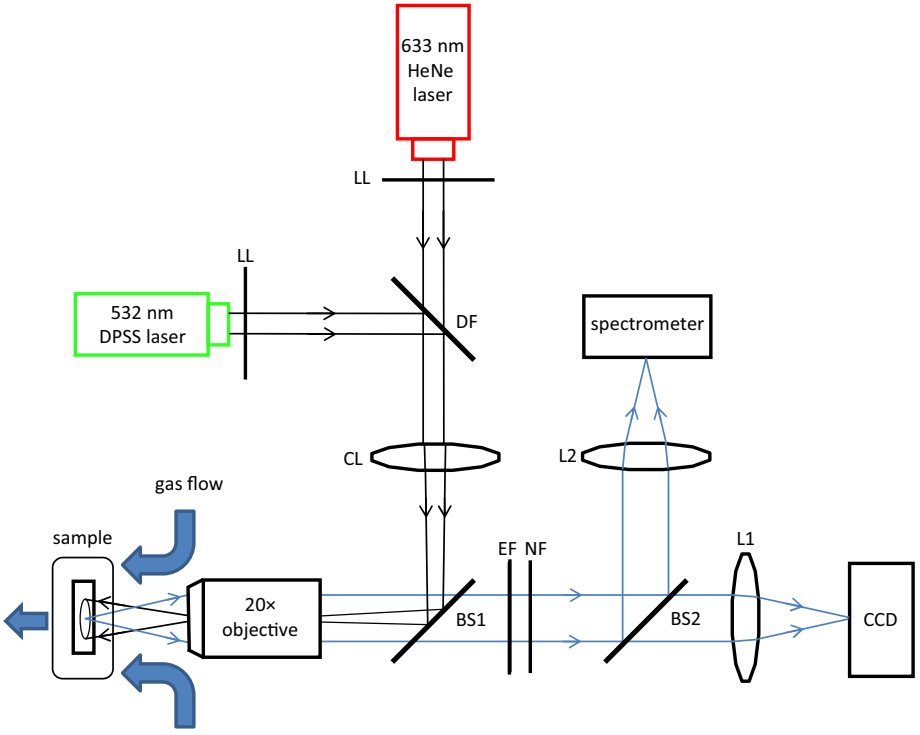

Fig. 1 – Schematic of the optical setup. DPSS laser: diode-pumped solid-state laser, LL: laser line filter, DF: dichroic filter, CL: cylindrical lens, BS: beam splitter, EF: edge filter, NF: notch filter, L1, L2: focusing lenses. The reactor is also illustrated schematically. (A color version of this figure can be viewed online.)

final beamsplitter (BS2) sends part of the scattered signal to be focused through a lens (L1) onto a CCD camera for *in situ* imaging, in order to track sample movement and to ensure that the spot is focused. The other part of the signal is focused through a second lens (L2), onto a 0.25 m spectrometer using a 100 μm slit, a 300 lines/mm grating and a cooled CCD camera so that the spectra could be recorded.

3. Results and discussion

This system was used to obtain real-time *in situ* metallic Raman spectra during the etch process. Fig. 2 shows the evolution of a sample etched at 500 °C under O_2. The entire spectrum from 525 to 850 nm (i.e., Raman shift of −209 to 7074 cm^{-1} for 532 nm line or Raman shift of −3204 to 4097 cm^{-1} for 632.8 nm line) was collected simultaneously. The figures show important peaks originating primarily from the (a) 532 nm and (b) 633 nm laser respectively. All spectra are shown chronologically from top to bottom in 200 s intervals, with each frame having a 10 s exposure, and the top spectrum corresponding to conditions just prior to O_2 flow into reactor. In both spectra, carbonaceous species produce the indicated G bands (comprised of G^+ and G^- peaks), RBM bands, and the D bands. In Fig. 2(a), a window that primarily represents scattering from the 532 nm laser, the low intensity anti-Stokes G band of the 633 nm laser is also visible, falling between the D and G bands of the green laser.

Raman bands of the silicon substrate, namely the transverse acoustic (TA) and transverse optical modes (TO), are also visible. Note that the first order Si (TO) peak is relatively intense and does not overlap with any other Raman band. If the SWCNT sample does not move and is sufficiently transparent, the silicon band intensity is expected to remain constant. However, in practice, the samples experienced a gradual spatial drift during etching that caused a change in the intensities of every Raman band, presumably due to defocusing. We were unable to completely stop this drift, however we found we could largely compensate for it by tracking the changes to the Si (TO) peak intensities for a given laser frequency, and using these to correct for the other Raman bands generated by the same laser. This relies on the assumption that the defocusing affects both bands equally. In addition to the drift, in the first few seconds the sample changed from slightly opaque due to amorphous carbon, to basically transparent. This effect and the use of the Si peak as an internal standard is presented in detail in the Supplementary information (SI) section (see Figs. S1 and S2).

Our particular optical setup had low spectral resolution, largely because we used a low dispersion diffraction grating to capture the widely separated red and green laser Raman lines. Presumably this is due to optical aberrations in our setup. Certain features, including individual RBMs and G^- peaks, were not as well resolved as they could be. Switching to high dispersion gratings for single line Raman spectroscopy restores the resolution. While there is usually some tradeoff between resolution and bandwidth, a more perfect optical setup would not suffer as much from this compromise.

The G band intensity originates from sp^2 hybridized carbon in the sample. Prior to etching, the G bands from both

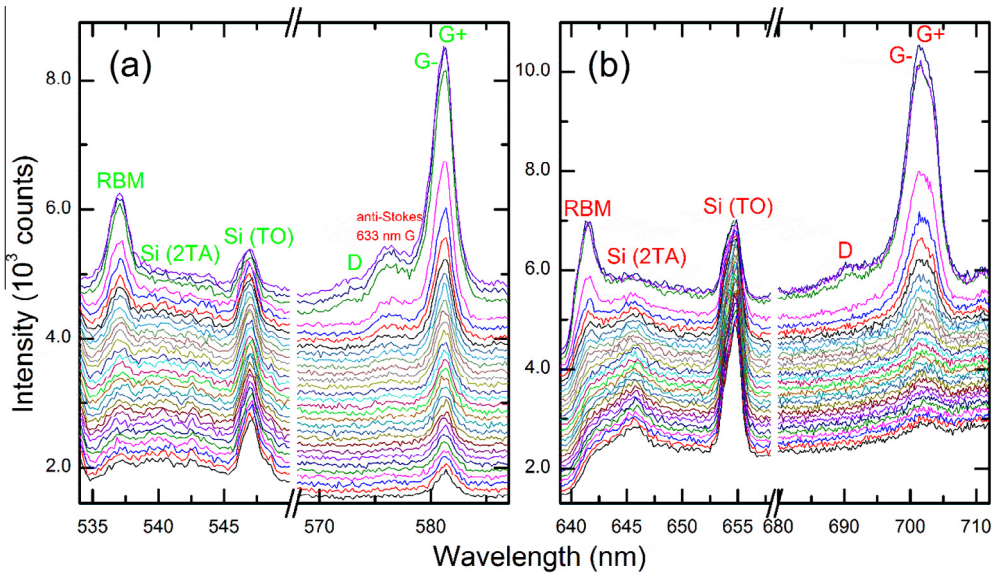

Fig. 2 – *In situ* Raman spectra of a sample etched at 500 °C in O_2. The sample was simultaneously exposed to Raman excitation wavelengths of 532 nm and 633 nm. Spectra have been offset and divided into windows (a) and (b) for clarity. (a) Spectral changes in semiconducting SWCNT RBM, D, G, and silicon substrate peaks due to the 532 nm laser. The anti-Stokes G band peak from the 633 nm laser also falls into this window. (b) Corresponding changes for metallic SWCNT peaks due to the 633 nm laser. Spectra are shown every 200 s, from t = 0 min to t = 96 min 40 s. Each frame is taken with a 10 s exposure. (A color version of this figure can be viewed online.)

lasers are the highest intensity bands. It is important to realize that the resonance effect is very strong in SWCNTs. While the raw SWCNT by mass was almost certainly predominantly non-SWCNT material, the G Raman signal even at the initial time is dominated by SWCNTs. At both room temperature and at the elevated temperatures at which etching occurred at appreciable rates, the structures of the G bands for the green and red lasers are distinct. In Fig. 2(a), the G^- peaks of the green are narrow and Lorentzian and are characteristic of SWCNTs that are mostly semiconducting. The peak width of the semiconducting G band is determined by the optical setup. In contrast, in Fig. 2(b), the G^- peaks of the red laser exhibit the typical non-Lorentzian, Breit–Wigner–Fano lineshape typical of metallic SWCNTs. Even with the low resolution of our setup, this band is clearly metallic. This confirms that the green laser is resonant with mostly semiconducting SWCNTs, while the red laser is resonant with mostly metallic SWCNTs.

When O_2 is supplied, both green and red G band intensities fall rapidly. However, the G band of the red laser drops more rapidly than that of the green laser. For example, given that the relative height between the G and Si bands in both Fig. 2(a) and (b) start off as roughly the same, it takes about 2200 s (11 frames) for the green laser G band height to fall to the height of the of Si (TO) band, whereas it takes only 800 s (4 frames) for the red laser G band to fall by the same amount. This indicates that the metallic SWCNTs are etching faster than their semiconducting counterparts. This difference in G band etching rate was observed for etching runs from 350 to 500 °C. Above 500 °C, the decay rates of both the red and green laser G bands are too rapid to track with our equipment.

The RBM bands are specific to the presence of SWCNTs in the sample. Consistent with the G band data in Fig. 2, the RBM intensities from the red laser Raman spectra decrease faster than those from the green laser. Although the Si Raman background makes it more difficult to track these bands at low intensity, the RBMs roughly track the G band intensities of their respectively lasers. For example in Fig. 2(b), at 96 min 40 s (last frame), both the G and RBM bands fall almost to zero intensity, revealing the characteristic silicon background below the RBMs. In contrast, in Fig. 2(a), the corresponding G and RBM bands are still somewhat intense compared to the silicon peaks.

Since RBMs are known to roughly vary inversely with SWCNT diameter [36], using higher resolution spectra, we can identify the range of diameters of SWCNTs resonant with both the green and red lasers. At room temperature, we identify intense RBMs at 176 ± 2 and 190 ± 2 cm^{-1} for the 532 nm laser, in addition to 190 ± 2 and 198 ± 2 cm^{-1} for the 633 nm laser. Lower intensity RBMs for the red laser are also observed at 165 ± 2, 170 ± 2, and 183 ± 2 cm^{-1}. The diameter (i.e., d_t) range, to a first approximation, is $d_t = (227\ cm^{-1}\ nm)/\omega_{RBM}$, where ω_{RBM} is the RBM frequency, yielding a shared diameter range of roughly 1.4 nm for both RBM populations [37–40]. A more refined relation (see SI, Fig. S3) gives similar results.

From the point of view of evaluating the selectivity of the etching it is important that the diameters are similar here, since it is well established that smaller diameter SWCNTs etch faster than larger diameter SWCNTs due to the greater strain in the nanotube lattice [11,12]. It should be noted that resonance windows do change with large changes in temperature, but since we etch at relatively low temperatures (i.e., ⩽600 °C), the resonance window is essentially the same for all our experiments.

It is difficult to assign definitive chiral indices to these SWCNTs using typical Kataura plot data, since multiple

assignments are possible [41–43]. However, for this diameter range, the red laser matches well with the metallic E_{11}^{M} transition, and the green laser matches well with the semiconducting E_{33}^{S} and E_{44}^{S} transitions (see SI, Fig. S3 for a detailed analysis). The finding that the red laser represents metallic peaks and the green laser represents semiconducting peaks is also consistent with the G band lineshape, which has a broad metallic G^- lineshape at 633 nm versus a narrow lineshape at 532 nm. Since the G band resonance window is larger than those of the RBMs, it follows these SWCNT diameter populations are also resonant within the green and red laser G bands.

The D band is characteristic of disorder in sp^2 carbon networks, meaning it is activated by defects [44]. The source material was raw laser nanotube soot, so part of the D band intensity may originate not from defects in the sp^2 carbon networks of the nanotube themselves but from the defective carbon nanoparticles in which they are embedded. The D band intensity was found to vary significantly from sample to sample. In Fig. 2, the D bands for this sample are relatively low, but appear to etch more rapidly than the G and RBM bands. In fact, regardless of absolute D band intensity, rapid D band etching for both laser lines was typical across all etching temperatures. In other words, defective carbon etching is always far more rapid than pristine SWCNT etching and most defects are etched away as the SWCNTs only begin to etch.

The ratio of D band to G band intensity is a commonly used means of characterizing sample SWCNT quality. The sample D/G ratio had a direct impact on overall SWCNT etching rates, even though the initial D band signal may not be from the SWCNTs themselves. We determined D/G ratio from integrated peak intensities where the background was subtracted using a trapezoidal rule that was applied previously [31,45]. The D/G ratios at room temperature for the green laser Raman signal range from 0.13 to 0.30, while those for the red laser range from 0.10 to 0.19. The D/G ratios for specific samples are tabulated in the SI (see Table S1).

The origin of the D bands for both lasers can be tentatively assigned from their frequencies and widths. At room temperature, the peak frequency and full width at half maximum of the D band of the 532 nm laser are 1333 ± 2 and $103 \pm 5\ cm^{-1}$, while those corresponding to the 633 nm laser are 1319 ± 2 and $91 \pm 5\ cm^{-1}$. An example of a high resolution spectrum including the D band is shown in the SI (see Fig. S4). From Ref.s [46] and [47], we find that these peak frequencies respectively correspond to defective SWCNTs with diameters of $1.25\ nm < d_t < 2\ nm$ and $1.25\ nm < d_t < 1.5\ nm$, which matches well with our RBM assignments. The lineshape and quite broad D band linewidths for both lasers, however, may suggest that part of the D band signal also comes from other non-resonant graphitic sp^2 carbon material, such as amorphous carbon [46].

Scanning electron microscope (SEM) images from samples etched for different durations provide snapshots of the morphological changes caused by etching. Fig. 3 shows SEM micrographs of samples etched at 475 °C at different times. Prior to etching, in Fig. 3(a), the raw laser soot consists of SWCNT networks coated in large amounts of non-nanotube material, which is presumably amorphous carbon. Despite the large non-SWCNT component, the Raman spectra are still dominated by SWCNT features, and this is because of the strong Raman enhancement for SWCNTs. The SWCNTs in the SEM image are tangled in bundles of varying thickness. Assuming that linear features less than ~2 nm in diameter are SWCNTs, isolated SWCNTs are visible on occasion.

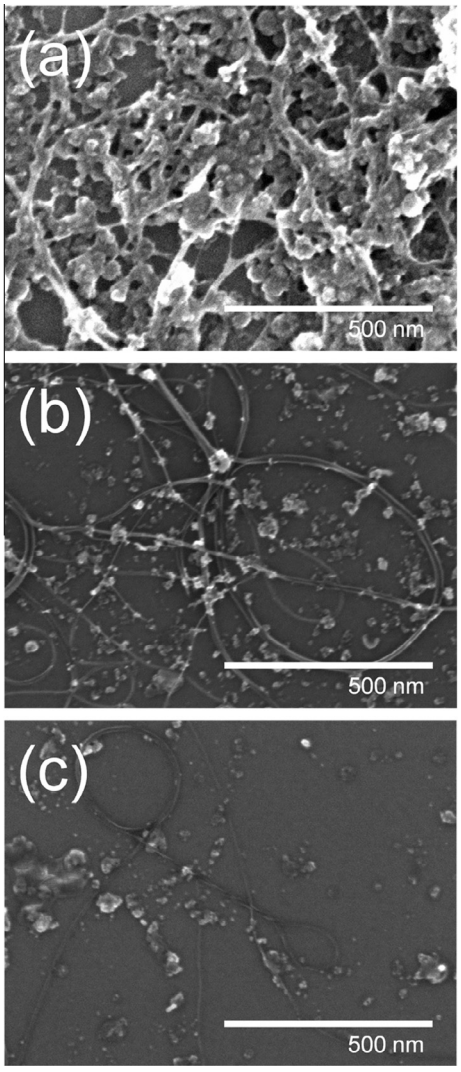

Fig. 3 – Scanning electron micrographs of samples etched in O_2 and stopped at different stages: (a) before etching, (b) after 22 min of etching at 475 °C and (c) after 1 h 30 min of etching at 475 °C.

Fig. 3(b) shows a sample after 22 min of etching. Non-nanotube carbon is still present, but at lower concentrations. Since bundles remain long, etching apparently occurs not only at the bundle ends but also at the sidewalls. Fig. 3(c) shows a sample etched after 90 min. The non-nanotube carbon that remains is probably graphitic and largely free of defects, since by this time the D band is negligible. Even at long etching time, SWCNT length still appears preserved although bundle thickness has continued to decrease. Others have shown by transmission electron microscopy that oxidation of multi-walled carbon nanotubes occurred at the sidewalls, and this data seems consistent with that process [48].

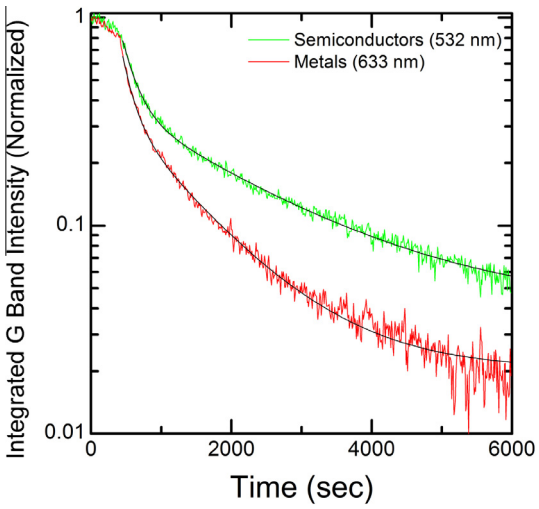

Fig. 4 – Time evolution of the G bands of samples etched using O_2 gas at 500 °C. See text for description of normalization. Each curve is fit with a biexponential function. (A color version of this figure can be viewed online.)

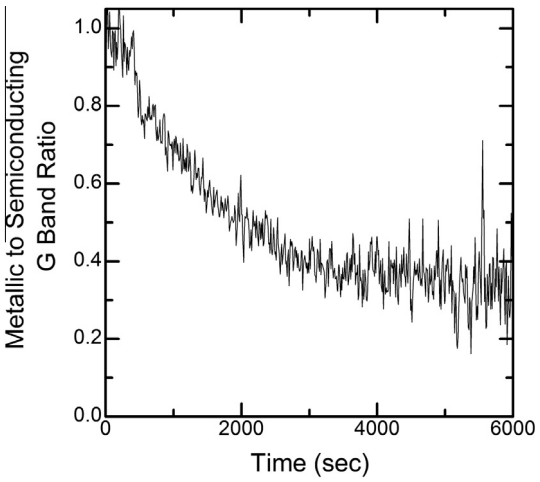

Fig. 5 – Evolution of metallicity (metal-to-semiconductor ratio) for samples etched using O_2 gas at 500 °C. The ratio of the 633 nm to the 532 nm G band from Fig. 2 is plotted over time. Metallicity falls over time and eventually stabilizes.

Fig. 4 shows a direct comparison of the evolution of semiconducting (green) and metallic (red) laser G bands for O_2 gas at 500 °C, after using the Si peak to compensate for drift in focus. The maximum G/Si intensity at $t = 0$ s was scaled to 1. This figure shows the relative difference in etching rates for the different electronic types. Etching of the semiconducting (green) G band proceeds more slowly than the metallic, red laser G band. For example, it takes approximately an additional 2000 s for the semiconducting (green) G peak to reach ~10% of its original intensity compared to the metallic (red) G peak.

The shape of the evolution curve for the G bands could not be fit by a single exponential, however, as in previous work, we found a reasonably good fit to a biexponential function, with separate fast and slow timescales, regardless of etching temperature [31] (see Fig. 4). The D band decays much more quickly and is fit well by a single exponential (see SI, Figs. S5 and S6). In Ref. [11] we speculated that the biexponential might be a result of changes in semi-to-metal ratio, but here this cannot be the case as both types separately show biexponential behavior. It is possible that there are nanotubes within each type which etch rapidly and others that do not. For example they may be in different environments, such as bundled or unbundled. It is also possible that a more resonant sub-population etches faster than a less resonant sub-population.

Fig. 5 shows the ratio of the semiconducting (green) to metallic (red) G band signal, or *metallicity*, derived using the G bands normalized as above. The ratio of metallic to semiconducting populations falls to ~0.4 after 3000 s. After this point the ratio changes little if at all. Note that etching does continue after this point but both populations change at the same rate.

Provided initial D/G ratios are similar prior to etching, etch rates increase systematically with temperature, as would ordinary be expected from any temperature activated

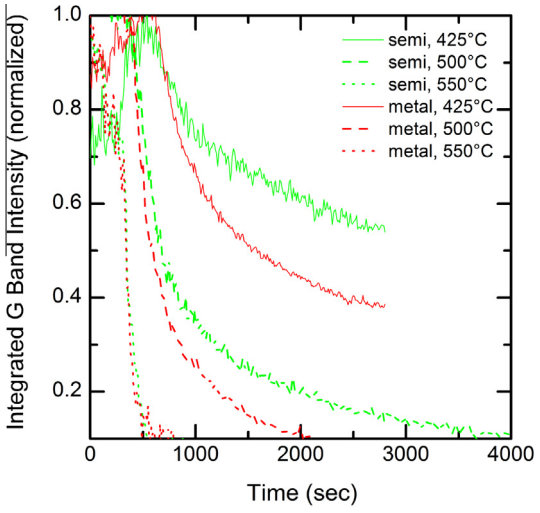

Fig. 6 – The effect of temperature on etching rate. Normalized G band time evolution for (a) 532 nm derived G bands and (b) 633 nm derived G bands. In both cases, etch rate increases with temperature. (A color version of this figure can be viewed online.)

process; see Fig. 6. (These samples were selected to have similar initial D/G ratios of 0.16–0.18 at 532 nm.) The semiconducting signal is shown in green, while the metallic signal is shown in red. It can be seen that the metallic signal falls faster for the entire temperature range. We note that the initial jump in the signal coincides with the early drop in the D band, as defective carbon is removed and the sample becomes transparent (see SI for details; Fig. S1). At these early times our use of the Si peak to normalize the other intensities in not correct because the Si signal is not stable as opaque, defective carbon is removed. The use of the Si signal to normalize is only meaningful if the Si peak is not changing.

This is a good approximation after the opaque material is removed, and the carbon layer becomes nearly transparent.

The initial D/G ratio can have a significant effect on etching rate. However, a sample with high D/G ratio could etch faster than a low D/G sample at a higher temperature. An example of this is shown in the SI (see Fig. S7). This seems reasonable since one might expect that defective samples are more susceptible to oxidative attack, and may show that at least some of these defects are along the sidewalls of the SWCNT bundles. Another possibility is that the presence of defective carbon catalyzes SWCNT etching, regardless of there location on or around the SWCNTs. However, even after the D band has vanished, etching still proceeds more rapidly on defective samples. This may be because once regions on the walls are opened the entire SWCNT etches faster. Also, regardless of initial D/G ratio, metallic SWCNTs always etched faster than semiconductors, indicating that type selectivity was not especially sensitive to D/G ratio.

Activation energies for etching could be extracted from the characteristic times (inverse of the rate) of the biexponential fits, yielding a fast timescale (τ_{fast}) and a slow timescale (τ_{slow}). The G band data was restricted to samples with similar D/G ratios (0.10–0.13 for the red laser). At high temperature the background was too high and the etch rate was too fast to extract meaningful data. Also at 550 °C (1000/$T \sim 1.2$) etching was too fast to obtain a τ_{slow} value.

The slopes of the fitted lines in Fig. 7 are activation energies for each time scale. The fast component of the semiconducting SWCNTs (green laser) has activation energy 0.21 ± 0.03 eV (light green line) and the fast component of the metallic SWCNTs (red laser) has activation energy 0.35 ± 0.09 eV (red line). The slow components are 0.41 ± 0.09 eV (dark green line) and 0.70 ± 0.02 eV (orange line). The uncertainties are rather large, and all that is clear is that the activation energies for the metallic timescale (etching rates) signal are fairly close to the semiconducting timescale, or possibly only slightly higher. The activation energy of the D band component is significantly higher, at 0.96 ± 0.05 eV. This implies that defective carbon etching is more sensitive to temperature change compared to defect-free sp^2 carbon. The D band etches more rapidly than other analyzed Raman bands across all etch temperatures, in line with the expectation that defective carbon should be generally less stable than defect-free sp^2 carbon.

We have focused primarily on the G band here. It is worth pointing out that we can track all other Raman bands similarly. The evolution of RBM, G, D and 2D bands for one sample is shown in the SI (see Fig. S5). In general, the RBM tracks the G band evolution very closely. This is despite the resonance window of the G band being larger, such that it tracks more SWCNT species. The 2D band tracked the G band very closely, and furthermore there were no substantial changes to 2D peak frequency or peak lineshape across all etched samples. It is reasonable that the 2D band tracks the G band rather than the D band, because while the D and 2D bands happen to relate to the same phonons, the 2D band (like the G band) is strong in defect free sp^2 carbon, while the D band requires defects [36,49]. Since in highly crystalline nanotubes the 2D band is strong, and since it is very well separated from the laser line, it may be a good choice for future *in situ* studies of SWCNT population evolution, as well as other nanocarbons.

A critical issue in the interpretation of the data is that G band intensities can change and shift not only if the abundance of nanotubes changes, but also if the degree of doping

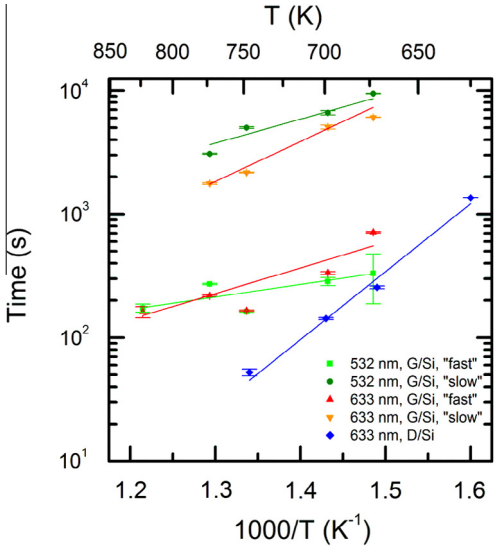

Fig. 7 – Activation plot for oxygen etching. The fast biexponential timescale (τ_{fast}, light green) and slow biexponential timescale (τ_{slow}, dark green) are shown for the 532 nm Raman G band signals. The biexponential timescales τ_{fast} (red) and τ_{slow} (orange) are shown for the 633 nm Raman G band signals, and τ values are shown for the 633 nm Raman D signal. (A color version of this figure can be viewed online.)

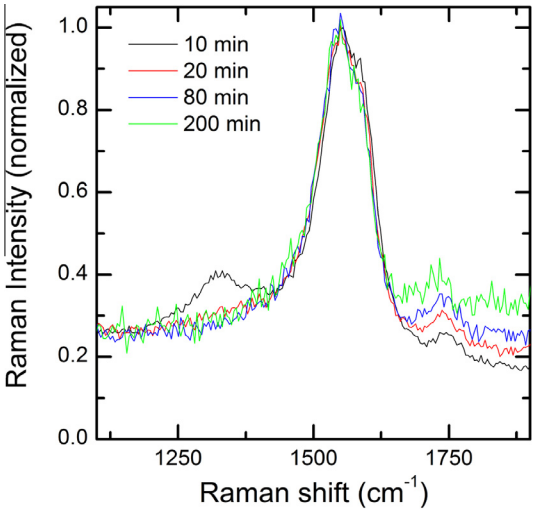

Fig. 8 – The lack of significant G band lineshape evolution. Metallic (633 nm) Raman G bands are shown at different etch times for the sample etched at 400 °C under O_2 gas. Spectra at different times have been normalized to the G band peak height, in order to highlight changes to G band shape over time. (A color version of this figure can be viewed online.)

changes [11,50,51]. If nanotubes become heavily doped, their G band lineshape should change significantly. Fig. 8 shows the typical G band lineshape evolution for the sample etched 400 °C. Only the G band of the red laser is shown since the semiconducting (green) G band is not resolved enough under our current optical system to clearly distinguish its G^- peaks. For the metallic G^-, which is meaningfully resolved, there was no lineshape evolution. This is clear in Fig. 8 where the G bands at different times have been normalized to the same height. If there was a strong doping effect, the G lineshape would have changed significantly, which is not the case. Also, since G^- lineshape is diameter dependent, this indicates that the diameter distribution has not changed widely. We conclude that, at least up to the point that this lineshape seems unchanged, the lack of spectral lineshape evolution shows that doping changes are insignificant.

We performed similar experiments to the above using CO_2 instead of O_2. Some results are shown in the SI (see Fig. S8). We saw a broadly similar evolution when CO_2 is used, with preferential metallic etching occurring across all temperatures, and with sample etching rates scaling with temperature. The type selectivity appears similar to O_2.

The preferential destruction of metallic versus semiconducting SWCNT species is consistent across all temperatures and initial defect ratios. Probably the largest difference in reactivity between different SWCNT chiralities in general is induced by local curvature [11,12], but in our case the metals and semiconductors have the nearly the same, relatively large diameter, and so curvature differences should be negligible.

Many SWCNT reactions may be selective by type, with various possible mechanisms explaining this behavior, as reviewed, for example, in the work of Yuan et al. [52]. Experimentally, metallic SWCNTs have been reported to be more reactive than their semiconducting counterparts for a variety of different reactions [13,31,53–59].

Physically, there are many differences between metals and semiconductors. The difference in reactivity is particularly interesting in SWCNTs because at large diameters the nanotubes are very similar structurally, yet their electronic properties are so different. Metals have electronic states available at the Fermi level and below, while semiconductors have gaps where no electronic states are present. The absence of electrons at an appropriate energy is one class of mechanisms of selectivity. The metallic nanotube would be better able to supply electrons to the reaction because of the presence of occupied states at energies that are in the gap for semiconductors. It is predicted that charge transfer between states in metallic SWCNTs leads to the formation of molecular frontier orbital interactions which facilitate reactions [60]. Delocalized electron states in metallic SWCNTs and the presence of a bandgap in semiconducting is reported to lead to lower formation energies for the reaction of methane plasma with SWCNTs [56]. A related, but distinct mechanism of selectivity is that the intrinsic conductivity of metals is generally higher, so electrons could simply be better supplied for chemical reactions. Separately, metals are more polarizable, and so van der Waals interactions may be stronger, leading to different sticking probabilities and this is a different class of mechanisms for selectivity. For example, the higher polarizability could result in more effective physisorption of reactants.

While there are various explanations for the difference in reaction rates the literature, we could not find detailed quantitative predictions of the etching dynamics that would follow from such models. In the future it will be of interest to test these models against the *in situ* data. Our experiments appear to exclude models for which the rates differ because of a significant difference in activation barrier, since the activation barrier is similar for both types here.

4. Conclusions

To summarize, we have tracked the spectral evolution of m-SWCNT and s-SWCNT of similar diameter undergoing oxidation using a simple, but non-standard two laser, *in situ* Raman spectroscopy technique. Two color Raman was found to be an effective *in situ* analysis technique, allowing us to simultaneously and separately probe and track the evolution of these two distinct populations and so instantaneously get feedback on metallicity. Assuming that the Raman signal is linear with abundance, at all temperatures m-SWCNTs are found to etch more rapidly than the s-SWCNTs. However, the selectivity is partial and ultimately etching becomes essentially non-selective. The initial D/G ratio strongly affects etching rates. Evolution curves were biexponential to a good approximation, and etch rates were activated, with similar activation energies for both m-SWCNTs and s-SWCNTs. In the future, models of the mechanism of selectivity should be strongly constrained by such *in situ* data. This type of two color *in situ* approach could be applied to track metallicity changes in many situations and could be applied to monitor a wide variety of processes.

Acknowledgment

We are grateful to Christopher T. Kingston for supplying the raw laser ablation nanotube material.

Appendix A. Supplementary data

Supplementary data associated with this article can be found, in the online version, at http://dx.doi.org/10.1016/j.carbon.2015.03.023.

REFERENCES

[1] Li Y, Mann D, Rolandi M, Kim W, Ural A, Hung S, et al. Preferential growth of semiconducting single-walled carbon nanotubes by a plasma enhanced CVD method. Nano Lett 2004;4:317–21.

[2] Li Y, Peng S, Mann D, Cao J, Tu R, Cho KJ, et al. On the origin of preferential growth of semiconducting single-walled carbon nanotubes. J Phys Chem B 2005;109:6968–71.

[3] Harutyunyan AR, Chen G, Paronyan TM, Pigos EM, Kuznetsov OA, Hewaparakrama K, et al. Preferential growth of single-walled carbon nanotubes with metallic conductivity. Science 2009;326:116–20.

[4] Kim W, Choi HC, Shim M, Li Y, Wang D, Dai H. Synthesis of ultralong and high percentage of semiconducting single-walled carbon nanotubes. Nano Lett 2002;2:703–8.
[5] Yang F, Wang X, Zhang D, Yang J, LuoDa Xu Z, et al. Chirality-specific growth of single-walled carbon nanotubes on solid alloy catalysts. Nature 2014;510:522–4.
[6] Chiang W, Mohan Sankaran R. Linking catalyst composition to chirality distributions of as-grown single-walled carbon nanotubes by tuning Ni_xFe_{1-x} nanoparticles. Nat Mater 2009;8:882–6.
[7] Li H, Li Q. Chapter 5: selective separation of single-walled carbon nanotubes in solution. In: Marulanda JM, editor. Electronic properties of carbon nanotubes. InTech; 2011. p. 69.
[8] Lukaszczuk P, Mijowska E, Kalenczuk R. Selective oxidation of metallic single-walled carbon nanotubes. Chem Pap 2013;10(2478):1–5.
[9] Khripin CY, Fagan JA, Zheng M. Spontaneous partition of carbon nanotubes in polymer-modified aqueous phases. J Am Chem Soc 2013;135:6822–5.
[10] Miyata Y, Maniwa Y, Kataura H. Selective oxidation of semiconducting single-wall carbon nanotubes by hydrogen peroxide. J Phys Chem B 2006;110:25–9.
[11] Miyata Y, Kawai T, Miyamoto Y, Yanagi K, Maniwa Y, Kataura H. Bond-curvature effect on burning of single-wall carbon nanotubes. Phys Status Solidi B 2007;244:4035–9.
[12] Miyata Y, Kawai T, Miyamoto Y, Yanagi K, Maniwa Y, Kataura H. Chirality-dependent combustion of single-walled carbon nanotubes. J Phys Chem C 2007;111:9671–7.
[13] Osswald S, Havel M, Gogotsi Y. Monitoring oxidation of multiwalled carbon nanotubes by Raman spectroscopy. J Raman Spectrosc 2007;38:728–36.
[14] Liu J, Wang C, Tu X, Liu B, Chen L, Zheng M, et al. Chirality-controlled synthesis of single-wall carbon nanotubes using vapour-phase epitaxy. Nat Commun 2012;3:1199.
[15] Zhou W, Zhan S, Ding L, Liu J. General rules for selective growth of enriched semiconducting single walled carbon nanotubes with water vapor as *in situ* etchant. J Am Chem Soc 2012;134:14019–26.
[16] Osswald S, Flahaut E, Ye H, Gogotsi Y. Elimination of D-band in Raman spectra of double-wall carbon nanotubes by oxidation. Chem Phys Lett 2005;402:422–7.
[17] Osswald S, Flahaut E, Gogotsi Y. *In situ* Raman spectroscopy study of oxidation of double- and single-wall carbon nanotubes. Chem Mater 2006;18:1525–33.
[18] Dementev N, Osswald S, Gogotsi Y, Borguet E. Purification of carbon nanotubes by dynamic oxidation in air. J Mater Chem 2009;19:7904–8.
[19] Dillon AC, Gennett T, Jones KM, Alleman JL, Parilla PA, Heben MJ. A simple and complete purification of single-walled carbon nanotube materials. Adv Mater 1999;11:1354–8.
[20] Morishita K, Takarada T. Scanning electron microscope observation of the purification behaviour of carbon nanotubes. J Mater Sci 1999;34:1169–74.
[21] Hou P, Liu C, Cheng H. Purification of carbon nanotubes. Carbon 2008;46:2003–25.
[22] Desforges A, Mercier G, Hérold C, Gleize J, Normand FL, Vigolo B. Improvement of carbon nanotube stability by high temperature oxygen/chlorine gas treatment. Carbon 2014;76:275–84.
[23] Mercier G, Herold C, Mareche J, Cahen S, Gleize J, Ghanbaja J, et al. Selective removal of metal impurities from single walled carbon nanotube samples. New J Chem 2013;37:790–5.
[24] Kawai T, Miyamoto Y. Chirality-dependent C–C bond breaking of carbon nanotubes by cyclo-addition of oxygen molecule. Chem Phys Lett 2008;453:256–61.
[25] Huang J, Zhang Q, Zhao M, Wei F. The release of free standing vertically-aligned carbon nanotube arrays from a substrate using CO_2 oxidation. Carbon 2010;48:1441–50.
[26] Finnie P, Ding J, Li Z, Kingston CT. Assessment of the metallicity of single-wall carbon nanotube ensembles at high purities. J Phys Chem C 2014;118:30127–38.
[27] Kaminska K, Lefebvre J, Austing DG, Finnie P. Real-time global Raman imaging and optical manipulation of suspended carbon nanotubes. Phys Rev B 2006;73:235410.
[28] Blackburn JL, Engtrakul C, McDonald TJ, Dillon AC, Heben MJ. Effects of surfactant and boron doping on the bwf feature in the Raman spectrum of single-wall carbon nanotube aqueous dispersions. J Phys Chem B 2006;110:25551–8.
[29] Lefebvre J, Finnie P. Photoluminescence and Förster resonance energy transfer in elemental bundles of single-walled carbon nanotubes. J Phys Chem C 2009;113:7536–40.
[30] Strano MS, Huffman CB, Moore VC, O'Connell MJ, Haroz EH, Hubbard J, et al. Reversible, band-gap-selective protonation of single-walled carbon nanotubes in solution. J Phys Chem B 2003;107:6979–85.
[31] Li-Pook-Than A, Lefebvre J, Finnie P. Type- and species-selective air etching of single-walled carbon nanotubes tracked with *in situ* Raman spectroscopy. ACS Nano 2013;7:6507–21.
[32] Kataura H, Kumazawa Y, Maniwa Y, Umezu I, Suzuki S, Ohtsuka Y, et al. Optical properties of single-wall carbon nanotubes. Synth Met 1999;103:2555–8.
[33] Kataura H, Kumazawa Y, Maniwa Y, Ohtsuka Y, Sen R, Suzuki S, et al. Diameter control of single-walled carbon nanotubes. Carbon Fullerenes '99 2000;38:1691–7.
[34] Brar VW, Samsonidze GG, Santos AP, Chou SG, Chattopadhyay D, Kim SN, et al. Resonance Raman spectroscopy characterization of single-wall carbon nanotube separation by their metallicity and diameter. J Nanosci Nanotechnol 2005;5:209–28.
[35] Kingston CT, Jakubek ZJ, Dénommée S, Simard B. Efficient laser synthesis of single-walled carbon nanotubes through laser heating of the condensing vaporization plume. Carbon 2004;42:1657–64.
[36] Dresselhaus MS, Dresselhaus G, Saito R, Jorio A. Raman spectroscopy of carbon nanotubes. Phys Rep 2005;409:47–99.
[37] Araujo PT, Pesce PBC, Dresselhaus MS, Sato K, Saito R, Jorio A. Resonance Raman spectroscopy of the radial breathing modes in carbon nanotubes. Phys E 2010;42:1251–61.
[38] Saito R, Fantini C, Jiang J. Excitonic states and resonance Raman spectroscopy of single-wall carbon nanotubes. In: Jorio A, Dresselhaus G, Dresselhaus MS, editors. Carbon nanotubes: advanced topics in the synthesis, structure, properties and applications (topics in applied physics). Berlin: Springer-Verlag Berlin Heidelberg; 2008. p. 251.
[39] Fantini C, Jorio A, Souza M, Strano MS, Dresselhaus MS, Pimenta MA. Optical transition energies for carbon nanotubes from resonant Raman spectroscopy: environment and temperature effects. Phys Rev Lett 2004;93:147406.
[40] Bachilo SM, Strano MS, Kittrell C, Hauge RH, Smalley RE, Weisman RB. Structure-assigned optical spectra of single-walled carbon nanotubes. Science 2002;298:2361–6.
[41] Nugraha ART, Saito R, Sato K, Araujo PT, Jorio A, Dresselhaus MS. Dielectric constant model for environmental effects on the exciton energies of single wall carbon nanotubes. Appl Phys Lett 2010;97:091905-3.
[42] Sato K, Saito R, Jiang J, Dresselhaus G, Dresselhaus MS. Discontinuity in the family pattern of single-wall carbon nanotubes. Phys Rev B 2007;76:195446.

[43] Liu K, Deslippe J, Xiao F, Capaz RB, Hong X, Aloni S, et al. An atlas of carbon nanotube optical transitions. Nat Nano 2012;7:325–9.
[44] Saito R, Hofmann M, Dresselhaus G, Jorio A, Dresselhaus MS. Raman spectroscopy of graphene and carbon nanotubes. Adv Phys 2011;60:413–550.
[45] Li-Pook-Than A, Lefebvre J, Finnie P. Phases of carbon nanotube growth and population evolution from *in situ* Raman Spectroscopy during chemical vapor deposition. J Phys Chem C 2010;114:11018–25.
[46] Picher M, Navas H, Arenal R, Quesnel E, Anglaret E, Jourdain V. Influence of the growth conditions on the defect density of single-walled carbon nanotubes. Carbon 2012;50:2407–16.
[47] Souza Filho AG, Jorio A, Samsonidze GG, Dresselhaus G, Pimenta MA, Dresselhaus MS, et al. Competing spring constant versus double resonance effects on the properties of dispersive modes in isolated single-wall carbon nanotubes. Phys Rev B 2003;67:035427.
[48] Koh AL, Gidcumb E, Zhou O, Sinclair R. Observations of carbon nanotube oxidation in an aberration-corrected environmental transmission electron microscope. ACS Nano 2013;7:2566–72.
[49] Dresselhaus MS, Jorio A, Hofmann M, Dresselhaus G, Saito R. Perspectives on carbon nanotubes and graphene Raman spectroscopy. Nano Lett 2010;10:751–8.
[50] Kavan L, Rapta P, Dunsch L, Bronikowski MJ, Willis P, Smalley RE. Electrochemical tuning of electronic structure of single-walled carbon nanotubes: *in-situ* Raman and vis-NIR study. J Phys Chem B 2001;105:10764–71.
[51] Kim SM, Kim KK, Jo YW, Park MH, Chae SJ, Duong DL, et al. Role of anions in the $AuCl_3$-doping of carbon nanotubes. ACS Nano 2011;5:1236–42.
[52] Chen Y, Andrew KN, Bai S, Si R, Wei L, Wang Q. Separation of metallic and semiconducting single-wall carbon nanotubes. In: Anonymous. Pan Stanford Publishing; 2012. p. 121–48.
[53] Park H, Zhao J, Lu JP. Distinct properties of single-wall carbon nanotubes with monovalent sidewall additions. Nanotechnology 2005;16:635–8.
[54] Zhang G, Qi P, Wang X, Lu Y, Li X, Tu R, et al. Selective etching of metallic carbon nanotubes by gas-phase reaction. Science 2006;314:974–7.
[55] Yu B, Hou P, Li F, Liu B, Liu C, Cheng H. Selective removal of metallic single-walled carbon nanotubes by combined *in situ* and post-synthesis oxidation. Carbon 2010;48:2941–7.
[56] Yuan D, Liu J. Purification of semiconducting carbon nanotubes. Small 2007;3:366–7.
[57] Otsuka K, Inoue T, Chiashi S, Maruyama S. Selective removal of metallic single-walled carbon nanotubes in full length by organic film-assisted electrical breakdown. Nanoscale 2014.
[58] Yang C, An KH, Park JS, Park KA, Lim SC, Cho S, et al. Preferential etching of metallic single-walled carbon nanotubes with small diameter by fluorine gas. Phys Rev B 2006;73:075419.
[59] Strano MS, Dyke CA, Usrey ML, Barone PW, Allen MJ, Shan H, et al. Electronic structure control of single-walled carbon nanotube functionalization. Science 2003;301:1519–22.
[60] Joselevich E. Electronic structure and chemical reactivity of carbon nanotubes: a chemist's view. ChemPhysChem 2004;5:619–24.

Supplementary Information for

Andrew Li-Pook-Than[1,2] and Paul Finnie[2,1] "Observation of the Metallic-Type Selective Etching of Single Walled Carbon Nanotubes by Real-Time in situ Two-Laser Raman Spectroscopy"

[1]Department of Physics, University of Ottawa, 150 Louis Pasteur, Ottawa, ON, K1N 6N5, Canada

[2]Security and Disruptive Technologies Portfolio, National Research Council Canada, 1200 Montreal Road, Ottawa, ON, K1A 0R6, Canada

Paul.Finnie@nrc-cnrc.gc.ca

1. Changes to nanotube film transparency in the first few seconds of etching

For the first few seconds of O_2 and CO_2 exposure on all nanotube samples, the silicon band intensities for both the 532 nm and 633 nm Raman lines were found to increase rapidly, before stabilizing. SiO_2 peaks undergo a similar change. An example of this evolution is shown in Figure S1 for the 500 °C O_2 etched sample. This change corresponds to changes in carbon nanotube film opacity, due to its thickness. The film became more transparent as defective carbon was removed from the sample surface.

Since the D band is sensitive to the presence of this defective carbon, whenever the D band intensities of either Raman line are strong enough to track, we find that once they fall to zero, the silicon background will begin to level off. In Figure S1, this occurs at around 600 seconds. After this point, the Si (TO) band intensity evolves more slowly. Subsequent evolution comes from the slow etching of graphitic carbon, including nanotubes, but is also affected by gradual drifts in focus, as described below.

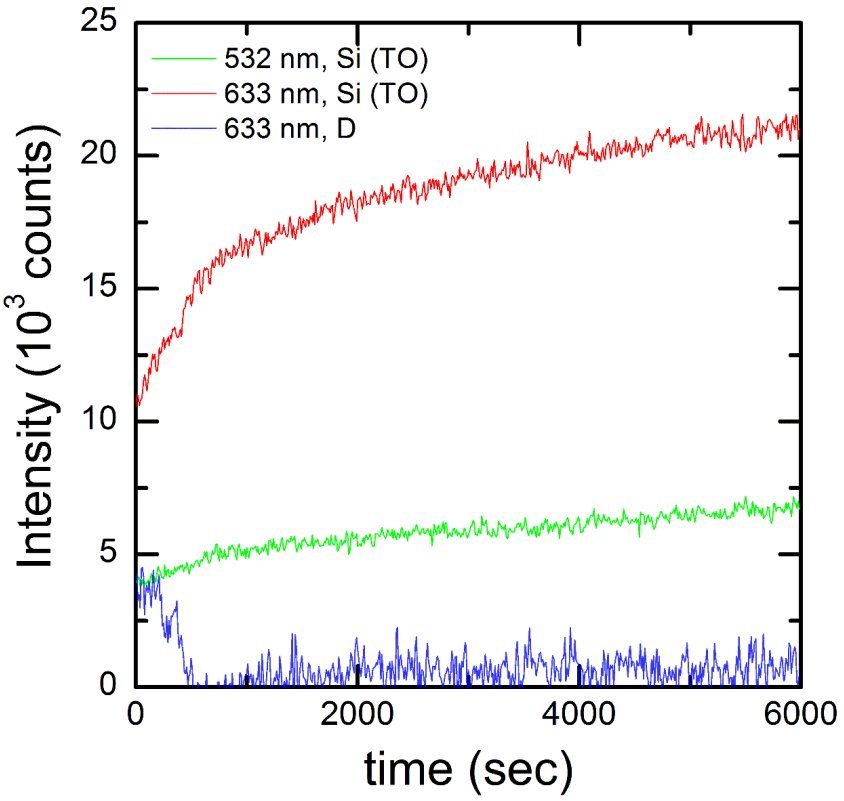

Figure S1. Typical time evolution plots of the background corrected, integrated intensities of both first-order Si (tranverse optical) bands and the D band from the 633 nm spectra for the sample etched at 500 °C in O_2 gas. The sudden change at early times is primarily due to the loss of highly defective carbon.

2. Gradual changes to all bands due to stability of the system

The intensity of the silicon band changed gradually on some samples and sometimes showed fluctuations. We attribute this kind of change to the gradual drift in focus, most likely caused by the thermal expansion of the reactor system. The depth of focus of the microscope objective measured in microns, while the experiments lasted up to hours, so stability on such scales can be challenging. In our case, the optical setup was focused and the signal optimized before the gas was introduced. During the subsequent *in situ* data gathering phase, there was no adjustment to the optical system. (Any adjustments introduced sudden changes in to the intensity evolution). Some defocusing was sometimes quite apparent from the *in situ* Raman imaging leg. We attempted to manually refocus from frame to frame but this was cumbersome and introduced obvious artifacts into the data. Ultimately, the best approach would be to engineer out any such drift, however we were unable to do so. We instead used the following procedure which, while imperfect, proved practical: we used the integrated first order Si band intensity as an internal intensity standard and scaled the G band intensities relative to that standard. Implicit in this is the assumption that all band intensities are equally affected by the change. Also, this approach is only valid when the silicon peak intensity is fixed. This is true if the carbon overlayer is very transparent. It introduces artifacts when the carbon overlayer is opaque and changing in opacity over time. Scaling in this way was found to compensate reasonably well for small instabilities in the optical system.

To illustrate how well Si band scaling corrects for these fluctuations, we recorded the Raman spectra of a nanotube sample and manually translated the sample in and out of focus along its optical axis. This was done at room temperature with the 532 nm laser line. These translations were much larger in magnitude than those occurring due to regular drift during a typical data gathering phase. Specifically, nanotube G band intensity was made to vary between its maximum peak height and roughly half this maximum. The background corrected G band and Si band intensities, as well as the variation in the G/Si ratio, are shown in Figure S2.

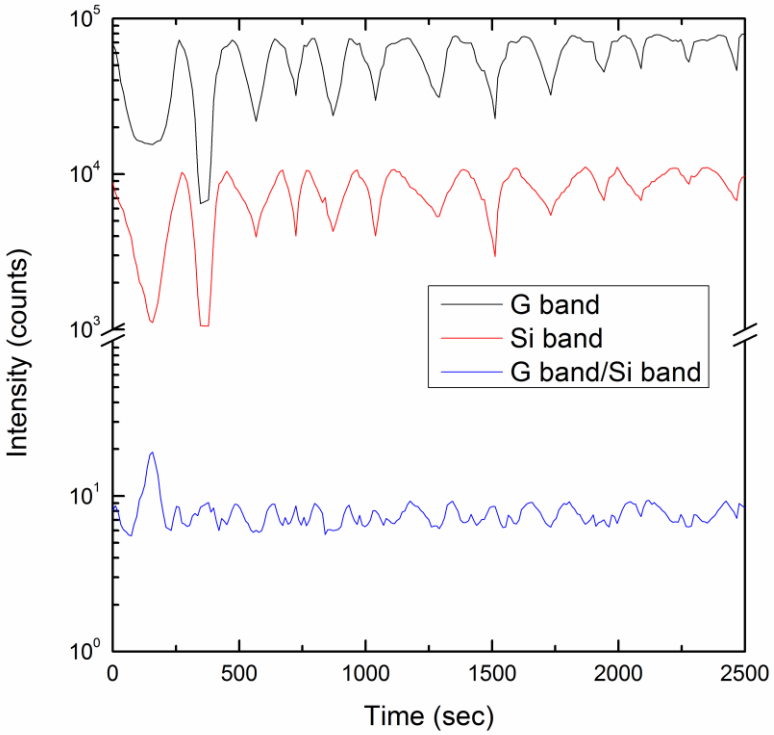

Figure S2. Focus variation test. Changes to the integrated intensities of the G band (grey), Si band (red) and corresponding G/Si ratio (blue) of a nanotube sample being manually translated in and out of focus.

From Figure S2, we notice that although the Si scaling does not completely correct for all the fluctuation in the G band intensity during translation, it does reduce the fluctuations significantly (at least by a factor of 2). Furthermore, when the G band is close to being in focus (i.e. near the G band intensity maxima), the corresponding corrected G/Si remains reasonably constant throughout the test (here with a value of ~9). In the actual etching experiments, the G band did not change as much as this. So the scaling shows that the Si band and G band are being modified in the same ratio when the laser spot is being modestly defocused.

3. Additional RBMs (with 514 nm, 785 nm laser sources) and Kataura plot

As described in the main text, we observe room temperature RBMs at ~176 cm^{-1} and ~190 cm^{-1} for the 532 nm laser, and ~165 cm^{-1}, ~170 cm^{-1}, ~183 cm^{-1}, ~190 cm^{-1} and ~198 cm^{-1} for the 633nm laser. We also checked our source material with a commercial Renishaw InVia Raman instrument at 514 nm, 633 nm and 785 nm. On that system, we

additionally obtained RBMs at ~186 cm^{-1} for the 514 nm laser, and at ~156 cm^{-1}, ~169 cm^{-1}, and ~205 cm^{-1} for the 785 nm laser.

From the optical data of Nugraha et al. and Sato et al. [91], we are therefore able to create a Kataura plot (see Figure S3), and assign these RBMs as either semiconducting or metallic nanotubes. Using the equation $\omega_{RBM} = (227/d_t)(1+C_e*d_t^2)^{1/2}$, where ω_{RBM} is RBM frequency, d_t is nanotube diameter, and using environmental constant $C_e = 0.067$ nm^{-2}, we first calculate d_t values for each RBM [26,85]. Then, for the environmental shift in E_{ii} energies, we apply the equation $E_{ii} = E_{ii}^{SG} - \check{C}_\kappa [A + B(p/d_t) + C(p/d_t)^2]$, where p is the cutting line index, and E_{ii}^{SG} corresponds to the supergrowth environment energy, with chosen constants A = 0.0428 eV, B = 0.04634 eV·nm, C = 0.00747 eV·nm^2, $\check{C}_\kappa = 1.42$ [89].

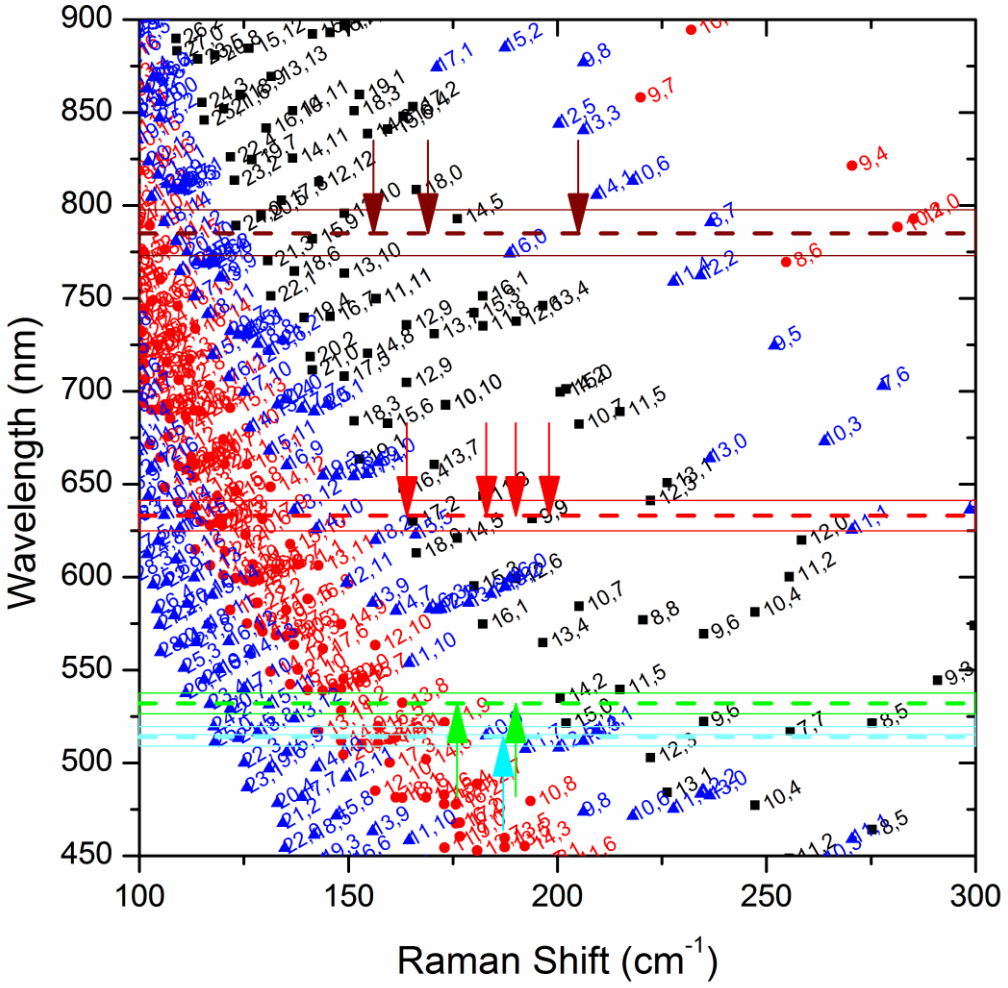

Figure S3. Kataura plot using optical data from Nugraha et al. and Sato et al. [91]. The dotted lines correspond to laser wavelengths at 514 nm, 532 nm, 633 nm, and 785 nm. Arrows indicate RBM frequencies that we observed on our samples using these lasers. The solid line correspond to the ± 25 meV uncertainty range between theoretical and experimental values reported by Nugraga et al. [89]. Black data points correspond to species in the metallic E11M subband, while blue and red data points correspond respectively to the mod-1 and and mod-2 semiconductors.

From Figure S3, we see that the 633 nm RBMs match well with metallic E_{11}^{M} species, while both 532 nm RBMs match well with semiconducting E_{33}^{S} and perhaps E_{44}^{S} species. Note that because of possible variation in our choice of environmental factor constants, and diameter assignment, as well as the large density of species in this region of the plot and the inherent theoretical uncertainty of the energy values, it is difficult to accurately assign a particular chirality to each RBM for our data. However, the

assignment to metallic and semiconducting bands seems fairly robust to reasonable changes in the six parameters of the model. The assignment of 633 nm resonance with the E_{11}^{M} metallic band and 532 nm resonance with higher (E_{33}^{S}, E_{44}^{S}) semiconducting bands is also consistent with the independent Rayleigh scattering derived data of Liu et al. [111]. Furthermore the assignment is consistent with the G- band lineshapes, which have metallic character for the 633 nm laser, and semiconducting character for the 532 nm and 514 nm lasers.

4. Initial D/G values

Our laser arc nanotube source material was in essence raw laser soot, and it proved to be inhomogeneous with respect to D/G ratios. When cast onto silicon substrates we found that different samples had different initial D/G ratios, with the ratio varying by almost a factor of three. Table S1 lists the range of D/G ratios used in O_2 etching experiments.

	Room temperature, pre-etch D/G ratio		
Sample no.	532 nm spectra	633 nm spectra	T (°C)
1	0.13	0.10	450
2	0.16	0.13	550
3	0.17	0.11	500
4	0.18	0.13	425
5	0.22	0.18	600
6	0.23	0.19	400
7	0.25	0.13	475
8	0.30	0.17	350

Table S1: D/G ratios for samples measured *in situ* using both laser colors. For each value, the background corrected, integrated intensity of the D band is divided by that of the G band. These samples were used for O_2 etching experiments.

5. Typical D band spectrum

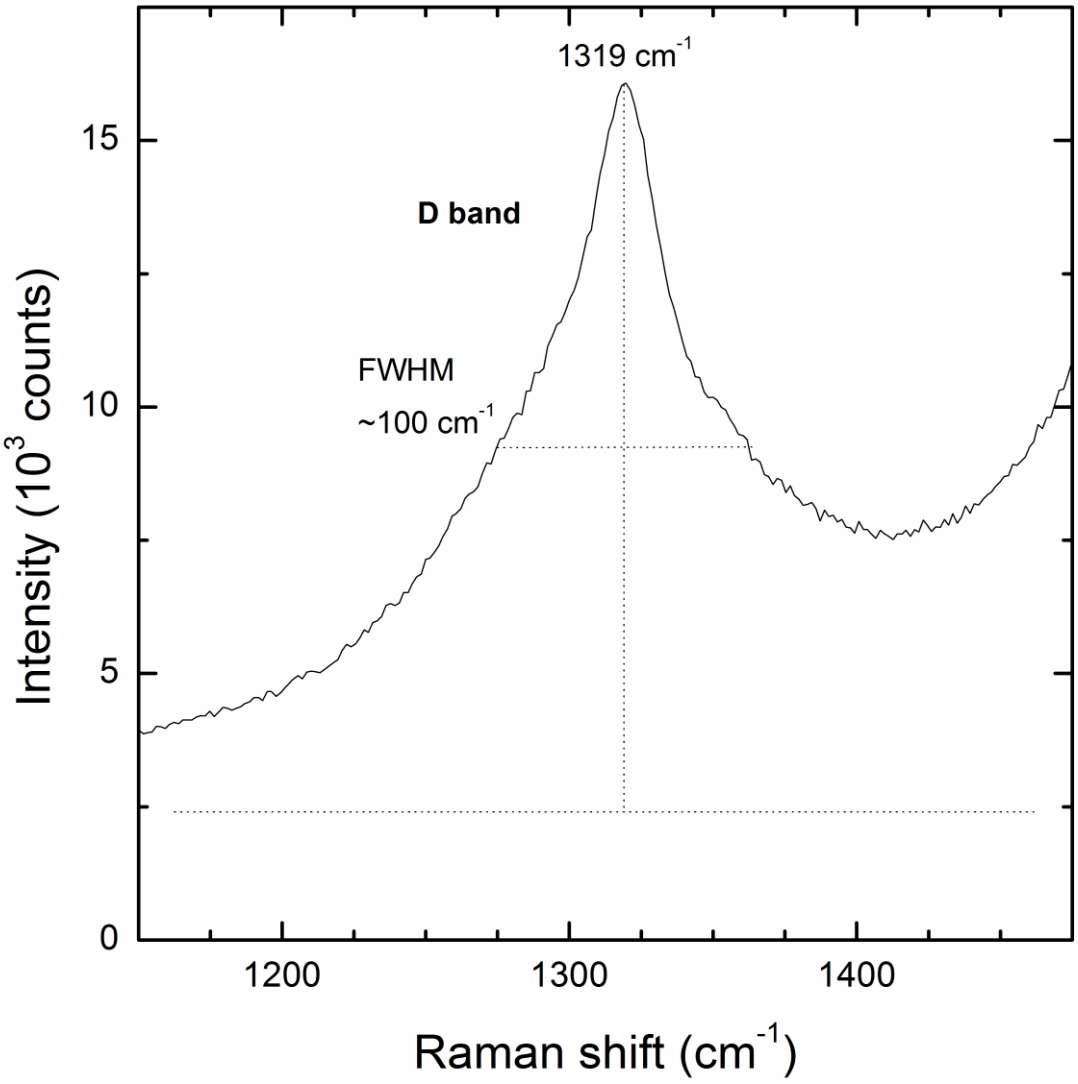

Figure S4: D band Spectrum of the Source Material at Room Temperature for 633 nm Excitation.

The D band position and lineshape is indicative of the nature of the defective carbon in the sample. Here, the D band is centered at 1319 cm^{-1} with a full width at half maximum (FWHM) of roughly 100 cm^{-1}. This spectrum is consistent with resonant 1.4 nm SWCNTs, potentially with some other non-resonant, amorphous carbon presence (see main text).

6. D, 2D and RBM band evolution

Although we focus on the G band spectral evolution in the main text, we were able to extract the evolution of many other bands. The G band intensity evolution across all samples was easier to track than those of the other Raman bands. The D band intensity was sometimes too low to meaningfully extract. Background subtraction for the RBM and 2D bands was somewhat uncertain because they overlapped with a uneven spectral background structures. The RBMs in particular overlap with uneven Si substrate background peaks and are relatively weaker in signal that the G band in our samples. Even so, we were able to extract their evolution, and several trends are apparent. The typical evolution of different Raman bands for both lasers is depicted in Figure S5 for the case of the sample etched at 500 °C in O_2.

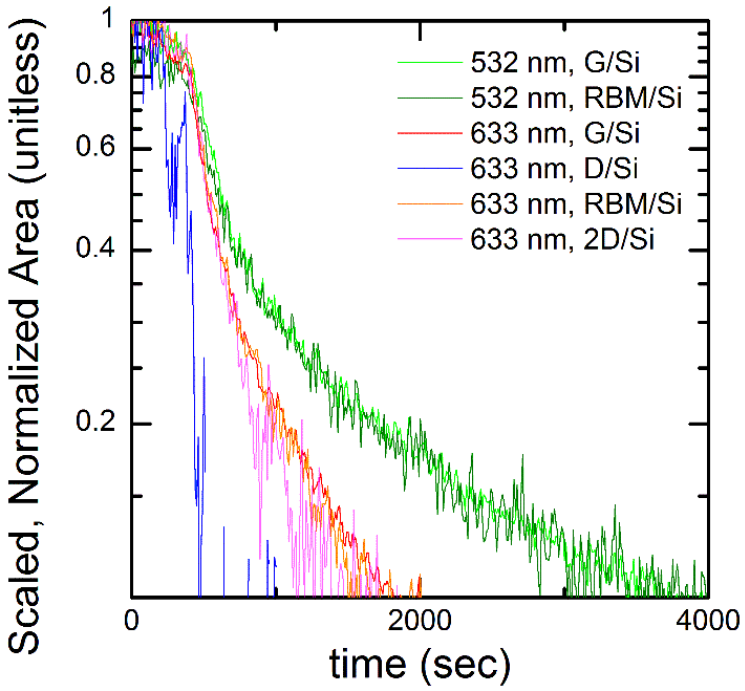

Figure S5. Tracking of other Raman bands. Time evolution plots of different integrated Raman intensities for the samples etched at 500 °C under O_2 gas. The G band (light green) and RBM band (dark green) evolution is shown for the 532 nm spectrum. The G band (red), RBM band (orange), 2D band (pink), and D band (blue) evolution is shown for the 633 nm spectrum. The RBM and 2D band track the G band of the same laser line relatively well. The D band etches faster than all the other bands.

The scaled RBM bands of the green and red lasers (indicated in dark green and orange, respectively) were found to closely track their corresponding G bands (in light green and red). The match was not always perfect, but generally speaking the G band closely represents the average evolution of resonant RBMs within the sample. It is worth noting that the resonance window for RBMs is smaller than for the G band, so species not represented by RBMs may still contribute to the G band.

The 2D band, an overtone mode of the D band also known as the G' band, is sensitive to graphitic carbon concentration and distribution on the sample. It is interesting to verify how well the 2D bands tracks with the G band evolution of SWCNTs. The 2D band tracks closely with the G band of its corresponding laser line, and etches much more slowly than its corresponding D band. Note that 2D bands of the green laser were difficult to extract in our particular experiment due to their overlap with the edge of the red notch filter. The tracking between the 2D and G bands suggests that the 2D band can be used for future *in situ* studies as a proxy for the SWCNT abundance. Its great separation from the laser line makes it very easy to isolate spectrally.

We emphasize here that the D band, corresponding to defective carbon, evolved very differently from the other bands. It etches very rapidly and falls with an exponential profile, compared to the biexponential drop in the other bands. This is very clearly shown for relatively defective samples that were etched more slowly at low temperatures, such as for the 400 °C O_2 etch sample analyzed in Figure S6.

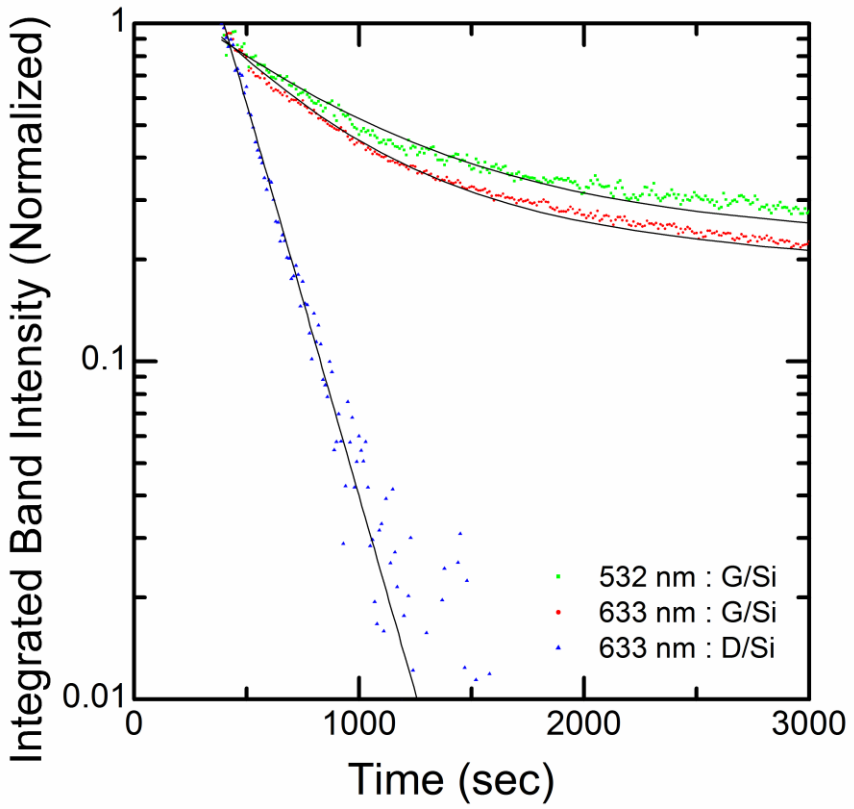

Figure S6. Functional fits to G and D band evolution. G/Si and D/Si time evolution for a typical O_2 sample etched at 400 °C. The G/Si signals are fit to biexponentials with fast and slow time scale components, τ_{fast} and τ_{slow}. The D/Si signal is fit to a single exponential, with a single time scale τ.

7. Etching rate dependence on initial D/G ratio

Our initial tests showed that the etch rates depended on the initial D/G ratio. Therefore, when comparing etch rates, we always selected samples with similar initial D/G ratios. At fixed or similar temperatures, samples with higher D/G ratios were found to etch faster. Figure S7 illustrates these differences in etching rates. Therefore, in the main text, for the Arrhenius plots, we select samples with similar, intially low D/G ratios.

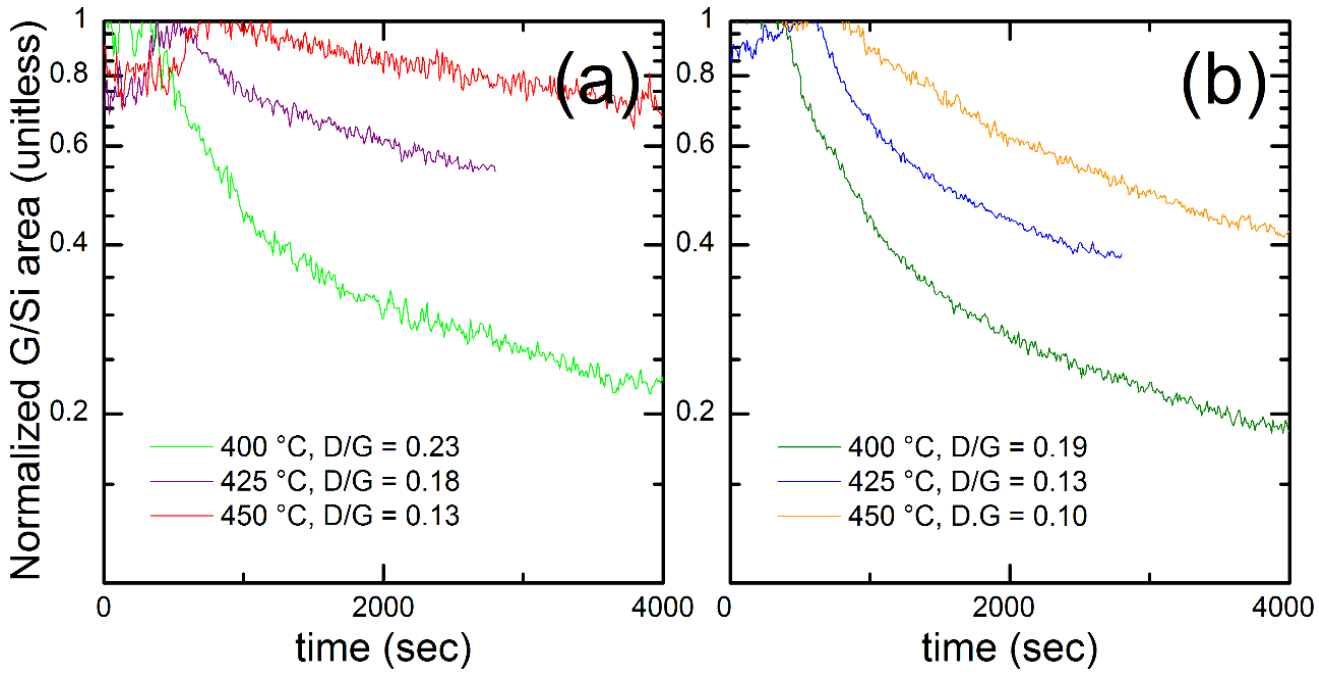

Figure S7. Effect of D/G ratio on etching rate using O_2 gas. Normalized G/Si time evolution for (a) 532 nm Raman spectra and (b) 633 nm Raman spectra. Although temperatures are similar, and even slightly increasing, etch rates are found to decrease substantially as D/G ratios decrease.

More defective samples are expected to be more susceptible to oxidative attack, and this may show that at least some of these defects are along the sidewalls of the SWCNT bundles. Another possibility is that the presence of defective carbon catalyzes SWCNT etching, regardless of there location on or around the SWCNTs. Once the defective regions on the walls are opened, entire SWCNTs become unstable and etch more rapidly, effecting both metallic and semiconducting nanotubes.

8. Examples of Selective Etching in Carbon Dioxide

We conducted entire series of etching experiments using CO_2 instead of O_2 as an etching gas for temperatures between T = 375 - 500 °C. One of the major products of the carbon nanotube combustion with O_2 is CO_2 gas. In addition to being a product of oxygen etching of carbon, CO_2 itself also oxidizes graphitic carbon, so it is interesting to compare the differences in O_2 and CO_2 etching kinetics.

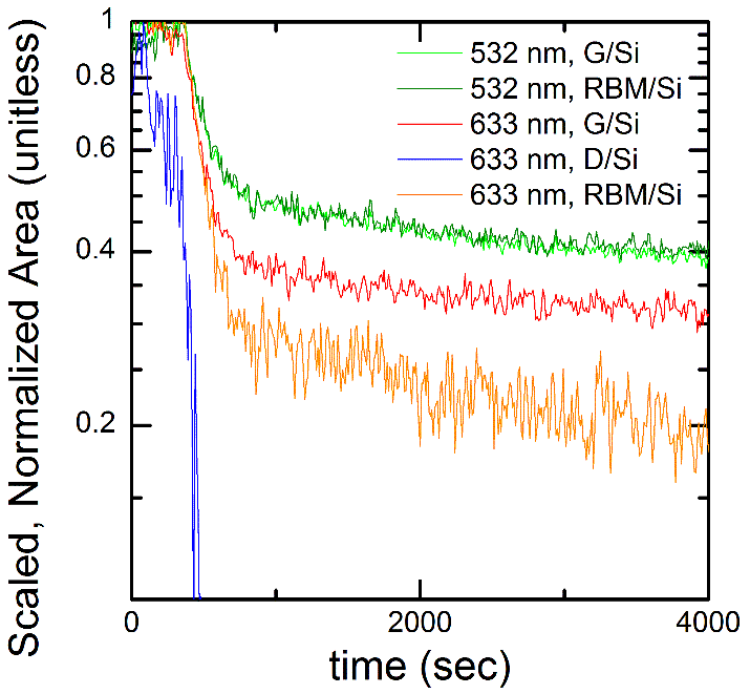

Figure S8. Etching with CO_2 gas. Time evolution plots of different integrated Raman intensities for the samples etched at 500 °C under CO_2 gas. Spectra have been scaled with respect to the first-order Si (TO) intensity of the substrate and normalized to 1 close to t = 0, once the Si background has stabilized. The G band (light green) and RBM band (dark green) evolution is shown for the 532 nm spectrum. The G band (red), RBM band (orange), and D band (blue) evolution is shown for the 633 nm spectrum.

Figure S8 shows a typical sample etched under CO_2 at 500 °C. Carbon dioxide etching experiments were performed and analyzed in exactly the same way as the oxygen experiments in the main text, except that the source gas was 4.01% CO_2 (with Ar balance, Air liquid certified grade) at one atmosphere. (Oxygen etching experiments were with 20.9 % O_2 Air liquid, certified grade also at one atmosphere.) As described above, all bands have been normalized with the Si first order band used as an internal standard. In general terms, the band evolution of samples etched with CO_2 is similar to those etched with O_2 (see Figure S5 for comparison) except that etching rates of the G and RBM bands are slower.

Across all samples, the same characteristic biexponential decrease in G and RBM band intensities for both laser lines is observed, as well as the exponential decrease in D band intensities. Notably, the red laser D band still etches very rapidly. The RBMs again roughly track with their corresponding G bands and similar RBM trends were also seen

on some O_2 samples. It should be noted that background subtraction is much less certain for RBMs than for the G band because of higher background in this spectral region.

CO_2 etching still resulted in a more rapid decrease in the metallic nanotube signal than the semiconducting nanotubes, though there is evidence that it is somewhat less selective than O_2. For example, at 1000 seconds the ratio between the scaled G band intensities of the green and red laser for the 500 °C O_2 etched sample is ~1.5, while the ratio for the corresponding CO_2 etched sample is ~1.2. Similarly, after etching and cooling to room temperature, the RBM intensities for the CO_2 post-etching spectra have comparable intensities, while the RBM intensity for the O_2 sample is visually weaker for the red laser than it is for the green laser. However, we are comparing equal times, not equal doses of gases and a rigorous comparison of the rates versus dose and other process variables was not made.

5. CONCLUSIONS

To summarize, the gas phase oxidation of different nanocarbons was successfully monitored *in situ* using our one- and two-laser Raman setup. In Chapter 2, we used *in situ* Raman spectroscopy to monitor the process of seeded carbon nanotube growth from fullerene seed particles. The yield of nanotubes was very low, making it very difficult to track the actual CVD growth phase. However, we verified that the oxidation stage had a critical effect on the resulting nanocarbon growth. We were able to track this *in situ*, observing significant spectral evolution during the fullerene seed oxidation stage. This motivated our interest in the study of carbon nanotube oxidation dynamics. In Chapters 3 and 4, we presented *in situ* Raman spectroscopy data that illustrated how oxidation resulted in the species selective etching of SWCNT populations. On its own, this phenomenon is important as it is describes a means of directly modifying SWCNT populations. It could also have direct implications for conventional CVD synthesis, because etching (oxidation) processes may be occurring simultaneously with growth, and also for seeding using SWCNT seeds as precursors. As in Chapter 2, subsequent growth using SWCNT seeds could also depend critically on a respective oxidation stage.

In Chapter 3, we performed *in situ* Raman spectroscopy with a single laser line, showing that metallic nanotubes etched more quickly. But the conclusion still had some ambiguity, because it was not possible to analyze nanotubes of different type (semiconductor or metallic) at the same time when they share the same diameter. In other words, type and diameter information were not distinct. Therefore, in Chapter 4, we addressed this issue by developing a novel two-laser Raman technique which allowed us to contrast the evolution of metallic and semiconducting SWCNTs of near-identical diameter. This confirmed that metallic nanotubes etched faster than the semiconductors.

In all our studies, oxidation was found to have a direct effect on nanocarbon structure and population. The gradual decay of the typically intense $A_g(2)$ and G band peaks in C_{60} and carbon nanotubes, respectively, was found to be an effective way of monitoring sample concentration at any given time. Similarly, monitoring the D band decay was consistently useful as a means of determining the rate of sample purification during oxidation, probably via the destruction of sp^3 carbon, although defect healing may

possibly play a role. While we were able to track the etching of C_{60} and regrowth of graphitic carbon by *in situ* Raman spectroscopy, the SWCNT yield was so low that we were not able to generate appreciable quantities of SWCNTs or track SWCNT growth dynamics specifically. Our approach to investigating the process is useful, but the specific procedure we used was not mature enough. As other researchers improve this and related processes, it is certain that *in situ* Raman spectroscopy can provide more important information.

Most importantly, in our carbon nanotube etching work, we consistently found thermal oxidation to be a type selective process, even for nanotube source materials that were very different in terms of origin, population make-up, structure, arrangement, and defect number. The nanotubes used in Chapter 3 were CVD nanotubes, while the nanotubes used in Chapter 4 were laser arc nanotubes of large diameter, and yet the etching appears to be similarly selective.

The method we used to show selectivity was different in each of the papers, with changes to RBM intensity and G band structure analyzed in the one-laser work, whereas differences in resonances were exploited to produce two simultaneously changing spectra in the two-laser work. At a given temperature, the rates of CNT oxidation in air, dilute O_2, and dilute CO_2 were all found to be roughly comparable.

Interestingly, the dynamics were similar. Biexponential decay instead of single-exponential decay was observed for all G bands across all our nanotube studies using air, O_2, and even CO_2 gas. This form is visible in our raw data, both before and after correcting for spectral background and sample movement. This was true for both CVD grown and laser ablation nanotube samples, respectively from Chapter 3 and Chapter 4, which were both comprised of networks of bundled surface nanotubes of comparable surface density. The two sample types were very different. The laser ablation samples were coated with far larger amounts of defective carbon. The laser ablation samples were dropcast on to the silicon wafers instead of being directly grown. The CVD grown nanotubes had a wide range of diameters, while the laser ablation samples were only large in diameter. Despite their differences, temperature dependent G band etching rates for samples etched under air and O_2 were similar. It therefore seems likely that a real biexponential process occurs during etching, which appears to be insensitive to the

presence of catalyst nanoparticles or how sp^3 carbon is distributed across the sample. The presence of water vapor and other low concentration oxidants in atmosphere does not appear to have a major effect on this trend.

We can speculate about the origin of biexponential shape. Assuming that the biexponential form present in Chapters 3 and 4 have the same origin, we can infer from Chapter 4 that the process occurs regardless of whether the SWCNTs are metallic or semiconducting. One possible interpretation is that the form instead relates directly to the debundling process. Conceivably, two different populations of nanotubes within a bundle could be etching at two different rates. For example, outer tubes could etch faster than inner tubes within a given bundle. Because the substantial decay in the D band is found to always occur prior to G band decay in nanotube, it is possible that defects on the exterior of surface bundles cause these exterior nanotubes to etch more rapidly compared to protected inner nanotubes. Because bundle composition is not homogeneous from sample to sample, this could explain why the magntitude of the prefactors for the individual fast and slow exponentials differs significantly from sample to sample. Another speculative possibility might be that the fast and slow components of the biexponentials correspond to differences in the rates of etching of the nanotube ends and sidewalls for each individual nanotube. Regardless, the origins of the biexponential decay is certainly a topic for future investigation.

In broad terms, results presented in Chapter 3 and Chapter 4 lead to similar conclusions regarding the selective etching of metallic SWCNTs versus semiconducting SWCNTs. That is, metallic nanotubes etch faster in both studies. However, because we were able to get very detailed information about the evolution, we did see some differences and these would be interesting to explore in further detail in future work. One difference is that in Chapter 3, the RBMs exhibited single exponential decay and the D bands exhibited biexponential decay, whereas in Chapter 4, it was the RBMs that decayed biexponentially, while the D bands decayed exponentially. Speculatively, this could conceivably be due to differences in the composition of the nanotube bundles. For example, the RBMs of the laser ablation nanotubes in Chapter 4 correspond to a different range of possible chiralities compared to the CVD grown nanotubes in Chapter 3.

The RBMs in Chapter 4 also seemed to match closely with the decay rates of the G band, whereas the RBMs in Chapter 3 visibly etched at different rates. This is a direct result of etch rate being directly relating to differences in nanotube diameter, metallicity, and chiral angle. Since there was a wide range of resonant RBM species in Chapter 3, which were not present Chapter 4, we observed different etch rates only in that Chapter.

The differences in D band kinetics between Chapters 3 and 4 may correspond to the different origins in sp^3 carbon in these studies. In Chapter 4, the probable amorphous carbon likely originates from soot in the laser ablation process, whereas the low D band in Chapter 3 may have a greater contribution from defects embedded within the nanotube bundle sidewalls. Therefore, it follows that the D band evolution in the Chapter 4 is very different from the corresponding G band evolution. This is an important point, as different types of defects may lead to different consequences.

We did not find the same activation energies in Chapter 3 and Chapter 4. It must be recognized that the two source materials were quite different to begin with (CVD nanotubes with a wide range of small diameters in the first case, vs. laser ablation SWCNTS with a smaller range of large diameters in the latter case). It must also be recognized that the activation energies we deduced have significant statistical error and may be subject to larger experimental errors which are difficult to quantify. In future work the activation energies could be determined and compared more rigorously. These activation energies could be extracted from experiments entirely along the lines of what we have already done

The origin of these differences is likely related to whatever structural differences that exist in the composition of the bundles in these studies. The activation barrier for G band etching in the Chapter 4 under oxygen is lower than the average energy obtained in the air etching studies, which might be expected to some extent.

We have established that the *in situ* Raman technique is useful for tracking metallic type and population in real time. We have established that etching is selective, but only partially. So, a very promising direction for future work would be to see to what extent the etching process (procedure, etchants, etc.) could be varied in order to achieve a greater change to metallicity during the nanotube etching process, while quantifying these live changes. In particular, a different range of gas pressures, or different combination of

gases could result in a more purely semiconducting end-product. Another interesting avenue of study would be to track the etching process of a variety of pre-sorted metallic and semiconducting nanotube samples and verify whether the difference in etching rates is identical.

Similarly, in terms of our C_{60} work, it is possible that a more highly active seed particle can be generated under different experimental parameters. Since our early work on the topic, there are more reports of successful cloning.[100,105,112] If the problem of low yield in our work is overcome, the same type of study will be much more valuable, since we will be able to observe what CNT populations are being grown and nucleated from what particular types of seeds.

It would also be interesting to attempt to partially oxidize and then regrow our nanotube samples, in order to produce viable seeds for tailed nanotube population growth. For example, combining a particular gas phase etching process with an established CVD growth technique that is known to already produce a certain range of nanotubes would allow us to test to whether cloning is possible, and to what extent a particular nanotube population can be narrowed by cycling through different growth and etching steps. Here, it is possible that a certain nanotube species could be selected for, by etching away unwanted species of different diameter or chiral angle, while population yield is increased during growth.

Our overall results are also particular relevant in the field of nanotube growth, since the observed etching reactions may unintentionally be taking place during the course of ordinary nanotube CVD synthesis. Actually, the concentrations of gases and the atmospheric pressure of the reactor were in part meant to approximate conditions that are similar to those in typical CVD experiments. Even an unintentional air leak in such an experiment could possibly affect nanotube species distribution in a way that was similar to the air or O_2 studies.

For other domains of nanotube research, two-laser Raman spectroscopy is easily applicable in a variety of gas phase experiments, wherein we would be interested in tracking the difference between two contrasting resonant nanotube populations. This includes studies involving defect healing and nanotube purification, since D and 2D band evolution is well characterized using our method.

So, to summarize, this work shows that *in situ* Raman is a direct and useful method of obtaining detailed data about changes to distinct nanocarbon populations undergoing chemical reactions, and that the technique should be useful in resolving many questions, especially those relating to nanotube growth, cloning, and population-specific destruction and separation reactions.

References

[1] Iijima S. Helical microtubules of graphitic carbon. Nature 1991;354:56-8.

[2] Novoselov KS, Geim AK, Morozov SV, Jiang D, Zhang Y, Dubonos SV et al. Electric Field Effect in Atomically Thin Carbon Films. Science 2004;306:666-9.

[3] Saito R, Dresselhaus G, Dresselhaus MS. Physical properties of carbon nanotubes. : World Scientific, 1998.

[4] Durkop T, Getty SA, Cobas E, Fuhrer MS. Extraordinary Mobility in Semiconducting Carbon Nanotubes. Nano Lett 2004;4:35-9.

[5] Javey A, Qi P, Wang Q, Dai H. Ten- to 50-nm-long quasi-ballistic carbon nanotube devices obtained without complex lithography. Proc Natl Acad Sci U S A 2004;101:13408-10.

[6] Pop E, Mann D, Wang Q, Goodson K, Dai H. Thermal Conductance of an Individual Single-Wall Carbon Nanotube above Room Temperature. Nano Lett 2006;6:96-100.

[7] Yu M, Lourie O, Dyer MJ, Moloni K, Kelly TF, Ruoff RS. Strength and Breaking Mechanism of Multiwalled Carbon Nanotubes Under Tensile Load. Science 2000;287:637-40.

[8] De Volder, Michael F. L., Tawfick SH, Baughman RH, Hart AJ. Carbon Nanotubes: Present and Future Commercial Applications. Science 2013;339:535-9.

[9] Zhang Q, Huang J, Qian W, Zhang Y, Wei F. The Road for Nanomaterials Industry: A Review of Carbon Nanotube Production, Post-Treatment, and Bulk Applications for Composites and Energy Storage. Small 2013;9:1237-65.

[10] Sun D, Liu C, Ren W, Cheng H. A Review of Carbon Nanotube- and Graphene-Based Flexible Thin-Film Transistors. Small 2013;9:1188-205.

[11] Park S, Vosguerichian M, Bao Z. A review of fabrication and applications of carbon nanotube film-based flexible electronics. Nanoscale 2013;5:1727-52.

[12] Yang F, Wang X, Zhang D, Yang J, LuoDa, Xu Z et al. Chirality-specific growth of single-walled carbon nanotubes on solid alloy catalysts. Nature 2014;510:522-4.

[13] Rao R, Liptak D, Cherukuri T, Yakobson BI, Maruyama B. *In situ* evidence for chirality-dependent growth rates of individual carbon nanotubes. Nat Mater 2012;11:213-6.

[14] Liu J, Wang C, Tu X, Liu B, Chen L, Zheng M et al. Chirality-controlled synthesis of single-wall carbon nanotubes using vapour-phase epitaxy. Nat Commun 2012;3:1199.

[15] Arnold MS, Green AA, Hulvat JF, Stupp SI, Hersam MC. Sorting carbon nanotubes by electronic structure using density differentiation. Nat Nano 2006;1:60-5.

[16] Liu H, Nishide D, Tanaka T, Kataura H. Large-scale single-chirality separation of single-wall carbon nanotubes by simple gel chromatography. Nat Commun 2011;2:309.

[17] Zhang L, Zaric S, Tu X, Wang X, Zhao W, Dai H. Assessment of Chemically Separated Carbon Nanotubes for Nanoelectronics. J Am Chem Soc 2008;130:2686-91.

[18] Amama PB, Pint CL, McJilton L, Kim SM, Stach EA, Murray PT et al. Role of Water in Super Growth of Single-Walled Carbon Nanotube Carpets. Nano Lett 2009;9:44-9.

[19] Futaba DN, Goto J, Yasuda S, Yamada T, Yumura M, Hata K. A Background Level of Oxygen-Containing Aromatics for Synthetic Control of Carbon Nanotube Structure. J Am Chem Soc 2009;131:15992-3.

[20] Li X, Zhang X, Ci L, Shah R, Wolfe C, Kar S et al. Air-assisted growth of ultra-long carbon nanotube bundles. Nanotechnology 2008;19:455609.

[21] Futaba DN, Goto J, Yasuda S, Yamada T, Yumura M, Hata K. General Rules Governing the Highly Efficient Growth of Carbon Nanotubes. Adv Mater 2009;21:4811-5.

[22] Collins PG, Arnold MS, Avouris P. Engineering Carbon Nanotubes and Nanotube Circuits Using Electrical Breakdown. Science 2001;292:706-9.

[23] Pop E. The role of electrical and thermal contact resistance for Joule breakdown of single-wall carbon nanotubes. Nanotechnology 2008;19:295202.

[24] Seidel RV, Graham AP, Rajasekharan B, Unger E, Liebau M, Duesberg GS et al. Bias dependence and electrical breakdown of small diameter single-walled carbon nanotubes. J Appl Phys 2004;96:6694-9.

[25] Dresselhaus MS, Jorio A, Hofmann M, Dresselhaus G, Saito R. Perspectives on Carbon Nanotubes and Graphene Raman Spectroscopy. Nano Lett 2010;10:751-8.

[26] Dresselhaus MS, Dresselhaus G, Saito R, Jorio A. Raman Spectroscopy of Carbon Nanotubes. Phys Rep 2005;409:47-99.

[27] Dresselhaus MS, Dresselhaus G, Saito R, Jorio A. Carbon nanotubes : quantum cylinders of graphene, Chapter 4 - Raman Spectroscopy of Carbon Nanotubes. In: Saito S,

Zettl A, editors. Carbon nanotubes : quantum cylinders of graphene, Amsterdam: Elsevier; 2008, p. 83.

[28] Finnie P, Ding J, Li Z, Kingston CT. Assessment of the Metallicity of Single-Wall Carbon Nanotube Ensembles at High Purities. J Phys Chem C 2014;118:30127-38.

[29] Jorio A, Kauppinen E, Hassanien A. Carbon-Nanotube Metrology. In: Jorio A, Dresselhaus MS, Dresselhaus G, editors. Carbon Nanotubes: Advanced Topics in the Synthesis, Structure, Properties and Applications, New York: Springer; 2008, p. 63.

[30] Kaminska K, Lefebvre J, Austing DG, Finnie P. Real-time global Raman imaging and optical manipulation of suspended carbon nanotubes. Phys Rev B 2006;73:235410-7.

[31] Kaminska K, Lefebvre J, Austing DG, Finnie P. Real-Time *in situ* Raman Imaging of Carbon Nanotube Growth. Nanotechnol 2007;18:165707.

[32] Finnie P, Li-Pook-Than A, Lefebvre J. The dynamics of the nucleation, growth and termination of single walled carbon nanotubes from in situ Raman spectroscopy during chemical vapor deposition. Nano Res 2009;2:783.

[33] Li-Pook-Than A, Lefebvre J, Finnie P. Phases of Carbon Nanotube Growth and Population Evolution from *in situ* Raman Spectroscopy during Chemical Vapor Deposition. J Phys Chem C 2010;114:11018-25.

[34] Li-Pook-Than A, Lefebvre J, Finnie P. Type- and Species-Selective Air Etching of Single-Walled Carbon Nanotubes Tracked with in Situ Raman Spectroscopy. ACS Nano 2013;7:6507-21.

[35] Yu X, Zhang J, Choi W, Choi J, Kim JM, Gan L et al. Cap Formation Engineering: From Opened C60 to Single-Walled Carbon Nanotubes. Nano Lett 2010;10:3343-9.

[36] Dresselhaus MS, Dresselhaus G, Eklund PC. Chapter 2 - Carbon Materials. In: Eklund MSDDC, editor. Science of Fullerenes and Carbon Nanotubes, San Diego: Academic Press; 1996, p. 15-59.

[37] Krueger A. Fullerenes - Cages Made from Carbon. In: Carbon Materials and Nanotechnology: Wiley-VCH Verlag GmbH & Co. KGaA; 2010, p. 33-122.

[38] Li C, Wang B, Yao Y, Piao G, Gu L, Wang Y et al. The structural transitions of C60 nanowhiskers under an electric field characterized by in situ transmission electron microscopy and electron energy-loss spectroscopy. Nanoscale 2014;6:6585-9.

[39] Haddon RC. Chemistry of the Fullerenes: The Manifestation of Strain in a Class of Continuous Aromatic Molecules. Science 1993;261:1545-50.

[40] Okada S, Saito S, Oshiyama A. Energetics and Electronic Structures of Encapsulated C60 in a Carbon Nanotube. Phys Rev Lett 2001;86:3835-8.

[41] Rochefort A. Electronic and transport properties of carbon nanotube peapods. Phys.Rev.B 2003;67:115401.

[42] Rümmeli MH, Bachmatiuk A, Börrnert F, Schäffel F, Ibrahim I, Cendrowski K et al. Synthesis of carbon nanotubes with and without catalyst particles. Nano Review 2011;6:1-9.

[43] Ibrahim I, Bachmatiuk A, Grimm D, Popov A, Makharza S, Knupfer M et al. Understanding High-Yield Catalyst-Free Growth of Horizontally Aligned Single-Walled Carbon Nanotubes Nucleated by Activated C60 Species. ACS Nano 2012;6:10825-34.

[44] Krueger A. Carbon Nanotubes. In: Carbon Materials and Nanotechnology: Wiley-VCH Verlag GmbH & Co. KGaA; 2010, p. 123-281.

[45] Strano MS, Dyke CA, Usrey ML, Barone PW, Allen MJ, Shan H et al. Electronic Structure Control of Single-Walled Carbon Nanotube Functionalization. Science 2003;301:1519-22.

[46] Wohlers M, Werner H, Herein D, Schedel-Niedrig T, Bauer A, Schlögl R. Reaction of C60 and C70 with molecular oxygen. Synth Met 1996;77:299-302.

[47] Dresselhaus MS, Dresselhaus G, Jorio A. Unusual Properties and Structure of Carbon Nanotubes. Annu Rev Mater Res 2004;34:247-78.

[48] Dresselhaus MS, Dresselhaus G, Eklund PC, Rao AM. Carbon Nanotubes. In: Andreoni W, editor. Springer Netherlands; 2000, p. 331-379.

[49] Li H, Li Q. Chapter 5: Selective Separation of Single-Walled Carbon Nanotubes in Solution. In: Marulanda JM, editor. Electronic Properties of Carbon Nanotubes: InTech; 2011, p. 69.

[50] Datsyuk V, Kalyva M, Papagelis K, Parthenios J, Tasis D, Siokou A et al. Chemical oxidation of multiwalled carbon nanotubes. Carbon 2008;46:833-40.

[51] Stobinski L, Lesiak B, Kövér L, Tóth J, Biniak S, Trykowski G et al. Multiwall carbon nanotubes purification and oxidation by nitric acid studied by the FTIR and electron spectroscopy methods. J Alloys Compounds 2010;501:77-84.

[52] Chiang IW, Brinson BE, Huang AY, Willis PA, Bronikowski MJ, Margrave JL et al. Purification and Characterization of Single-Wall Carbon Nanotubes (SWNTs) Obtained from the Gas-Phase Decomposition of CO (HiPco Process). J Phys Chem B 2001;105:8297-301.

[53] Zhou W, Ooi YH, Russo R, Papanek P, Luzzi DE, Fischer JE et al. Structural characterization and diameter-dependent oxidative stability of single wall carbon nanotubes synthesized by the catalytic decomposition of CO. Chemical Physics Letters 2001;350:6-14.

[54] Futaba DN, Hata K, Yamada T, Mizuno K, Yumura M, Iijima S. Kinetics of Water-Assisted Single-Walled Carbon Nanotube Synthesis Revealed by a Time-Evolution Analysis. Phys Rev Lett 2005;95:056104.

[55] Futaba D, Goto J, Yasuda S, Yamada T, Yumura M, Hata K. General Rules Governing the Highly Efficient Growth of Carbon Nanotubes. Advanced Materials 2009;21:4811.

[56] Amama PB, Pint CL, Kim SM, McJilton L, Eyink KG, Stach EA et al. Influence of Alumina Type on the Evolution and Activity of Alumina-Supported Fe Catalysts in Single-Walled Carbon Nanotube Carpet Growth. ACS Nano 2010;4:895-904.

[57] Patole SP, Alegaonkar PS, Shin H, Yoo J. Alignment and wall control of ultra long carbon nanotubes in water assisted chemical vapour deposition. J Phys D 2008;41:155311.

[58] Patole SP, Alegaonkar PS, Lee H, Yoo J. Optimization of water assisted chemical vapor deposition parameters for super growth of carbon nanotubes. Carbon 2008;46:1987-93.

[59] Borowiak-Palen E, Pichler T, Liu X, Knupfer M, Graff A, Jost O et al. Reduced Diameter Distribution of Single-Wall Carbon Nanotubes by Selective Oxidation. Chem Phys Lett 2002;363:567-72.

[60] Menna E, Della Negra F, Dalla Fontana M, Meneghetti M. Selectivity of Chemical Oxidation Attack of Single-Wall Carbon Nanotubes in Solution. Phys Rev B 2003;68:193412.

[61] Brukh R, Mitra S. Kinetics of Carbon Nanotube Oxidation. J Mater Chem 2007;17:619-23.

[62] Miyata Y, Kawai T, Miyamoto Y, Yanagi K, Maniwa Y, Kataura H. Chirality-Dependent Combustion of Single-Walled Carbon Nanotubes. J Phys Chem C 2007;111:9671-7.

[63] Miyata Y, Kawai T, Miyamoto Y, Yanagi K, Maniwa Y, Kataura H. Bond-curvature effect on burning of single-wall carbon nanotubes. Phys Stat Sol (b) 2007;244:4035-9.

[64] Lukaszczuk P, Mijowska E, Kalenczuk R. Selective oxidation of metallic single-walled carbon nanotubes. Chem Papers 2013;10, 2478:1-5.

[65] Li S, Liu C, Hou P, Sun D, Cheng H. Enrichment of Semiconducting Single-Walled Carbon Nanotubes by Carbothermic Reaction for Use in All-Nanotube Field Effect Transistors. ACS Nano 2012;6:9657-61.

[66] Yu B, Hou P, Li F, Liu B, Liu C, Cheng H. Selective removal of metallic single-walled carbon nanotubes by combined *in situ* and post-synthesis oxidation. Carbon 2010;48:2941-7.

[67] Yu B, Liu C, Hou P, Tian Y, Li S, Liu B et al. Bulk Synthesis of Large Diameter Semiconducting Single-Walled Carbon Nanotubes by Oxygen-Assisted Floating Catalyst Chemical Vapor Deposition. J Am Chem Soc 2011;133:5232-5.

[68] Zhou W, Zhan S, Ding L, Liu J. General Rules for Selective Growth of Enriched Semiconducting Single Walled Carbon Nanotubes with Water Vapor as *in Situ* Etchant. J Am Chem Soc 2012;134:14019-26.

[69] Li Y, Mann D, Rolandi M, Kim W, Ural A, Hung S et al. Preferential Growth of Semiconducting Single-Walled Carbon Nanotubes by a Plasma Enhanced CVD Method. Nano Lett 2004;4:317-21.

[70] Yudasaka M, Zhang M, Iijima S. Diameter-selective removal of single-wall carbon nanotubes through light-assisted oxidation. Chemical Physics Letters 2003;374:132-6.

[71] Miyata Y, Maniwa Y, Kataura H. Selective Oxidation of Semiconducting Single-Wall Carbon Nanotubes by Hydrogen Peroxide. J Phys Chem B 2006;110:25-9.

[72] Kosynkin DV, Higginbotham AL, Sinitskii A, Lomeda JR, Dimiev A, Price BK et al. Longitudinal unzipping of carbon nanotubes to form graphene nanoribbons. Nature 2009;458:872-6.

[73] Xiao B, Li X, Li X, Wang B, Langford C, Li R et al. Graphene Nanoribbons Derived from the Unzipping of Carbon Nanotubes: Controlled Synthesis and Superior Lithium Storage Performance. J Phys Chem C 2014;118:881-90.

[74] Sinitskii A, Dimiev A, Kosynkin DV, Tour JM. Graphene Nanoribbon Devices Produced by Oxidative Unzipping of Carbon Nanotubes. ACS Nano 2010;4:5405-13.

[75] Bom D, Andrews R, Jacques D, Anthony J, Chen B, Meier MS et al. Thermogravimetric Analysis of the Oxidation of Multiwalled Carbon Nanotubes: Evidence for the Role of Defect Sites in Carbon Nanotube Chemistry. Nano Lett 2002;2:615-9.

[76] Arepalli S, Nikolaev P, Gorelik O, Hadjiev VG, Holmes W, Files B et al. Protocol for the characterization of single-wall carbon nanotube material quality. Carbon 2004;42:1783-91.

[77] Osswald S, Havel M, Gogotsi Y. Monitoring oxidation of multiwalled carbon nanotubes by Raman spectroscopy. J Raman Spectrosc 2007;38:728-36.

[78] Rosca ID, Watari F, Uo M, Akasaka T. Oxidation of multiwalled carbon nanotubes by nitric acid. Carbon 2005;43:3124-31.

[79] Strano MS, Dyke CA, Usrey ML, Barone PW, Allen MJ, Shan H et al. Electronic Structure Control of Single-Walled Carbon Nanotube Functionalization. Science 2003;301:1519-22.

[80] Doyle CD, Rocha JR, Weisman RB, Tour JM. Structure-Dependent Reactivity of Semiconducting Single-Walled Carbon Nanotubes with Benzenediazonium Salts. J Am Chem Soc 2008;130:6795-800.

[81] Ding L, Tselev A, Wang J, Yuan D, Chu H, McNicholas TP et al. Selective Growth of Well-Aligned Semiconducting Single-Walled Carbon Nanotubes. Nano Lett 2009;9:800-5.

[82] Boyd RW. Nonlinear optics, Chapter 10: Stimulated Raman Scattering and Stimulated Rayleigh-Wing Scattering. In: New York: Academic Press; 2003, p. 451.

[83] Kittel C. Introduction to solid state physics. 8th ed. Hoboken, NJ: Wiley, 2005.

[84] Jorio A, Pimenta MA, Filho AGS, Saito R, Dresselhaus G, Dresselhaus MS. Characterizing Carbon Nanotube Samples with Resonance Raman Scattering. New J Phys 2003;5:139.

[85] Saito R, Hofmann M, Dresselhaus G, Jorio A, Dresselhaus MS. Raman spectroscopy of graphene and carbon nanotubes. Adv Phys 2011;60:413-550.

[86] Park JS, Sasaki K, Saito R, Izumida W, Kalbac M, Farhat H et al. Fermi energy dependence of the G-band resonance Raman spectra of single-wall carbon nanotubes. Phys Rev B 2009;80:081402.

[87] Picher M, Navas H, Arenal R, Quesnel E, Anglaret E, Jourdain V. Influence of the growth conditions on the defect density of single-walled carbon nanotubes. Carbon 2012;50:2407-16.

[88] Souza Filho AG, Jorio A, Samsonidze GG, Dresselhaus G, Pimenta MA, Dresselhaus MS et al. Competing spring constant versus double resonance effects on the properties of dispersive modes in isolated single-wall carbon nanotubes. Phys Rev B 2003;67:035427.

[89] Nugraha ART, Saito R, Sato K, Araujo PT, Jorio A, Dresselhaus MS. Dielectric constant model for environmental effects on the exciton energies of single wall carbon nanotubes. Appl Phys Lett 2010;97:091905-3.

[90] Sato K, Saito R, Jiang J, Dresselhaus G, Dresselhaus MS. Discontinuity in the family pattern of single-wall carbon nanotubes. Phys Rev B 2007;76:195446.

[91] Nugraha A, Saito R, Sato K. Exciton Kataura Plot Page. 2014;2014:3,http://flex.phys.tohoku.ac.jp/eii/.

[92] Jorio A, Souza Filho AG, Dresselhaus G, Dresselhaus MS, Swan AK, Unlu MS et al. G-band Resonant Raman Study of 62 Isolated Single-Wall Carbon Nanotubes. Phys Rev B 2002;65:155412.

[93] Matus M, Kuzmany H. Raman spectra of single-crystal C60. Applied Physics A 1993;56:241-8.

[94] Matus M, Kuzmany H, Krätschmer W. Resonance Raman scattering and electronic transitions in C60. Solid State Commun 1991;80:839-42.

[95] van Loosdrecht PHM, van Bentum PJM, Verheijen MA, Meijer G. Raman scattering in single crystal C60. Chemical Physics Letters 1992;198:587-95.

[96] Temple PA, Hathaway CE. Multiphonon Raman Spectrum of Silicon. Phys Rev B 1973;7:3685-97.

[97] Glynn C, Lotty O, McSweeney W, Holmes JD, O'Dwyer C. Raman Scattering Spectroscopy of Metal-Assisted Chemically Etched Rough Si Nanowires. ECS Transactions 2011;35:73-86.

[98] Spizzirri PG, Fang J-, Rubanov S, Gauja E, Prawer S. Nano-Raman Spectroscopy of Silicon Surfaces. Materials and AustCeram Conference 2010;3:26.

[99] Rao F, Li T, Wang Y. Growth of “all-carbon” single-walled carbon nanotubes from diamonds and fullerenes. Carbon 2009;47:3580-4.

[100] Wang H, Yuan Y, Wei L, Goh K, Yu D, Chen Y. Catalysts for chirality selective synthesis of single-walled carbon nanotubes. Carbon 2015;81:1-19.

[101] Takagi D, Kobayashi Y, Homma Y. Carbon Nanotube Growth from Diamond. J Am Chem Soc 2009;131:6922-3.

[102] Omachi H, Nakayama T, Takahashi E, Segawa Y, Itami K. Initiation of carbon nanotube growth by well-defined carbon nanorings. Nat Chem 2013;5:572-6.

[103] Liu B, Liu J, Li H, Bhola R, Jackson EA, Scott LT et al. Nearly Exclusive Growth of Small Diameter Semiconducting Single-Wall Carbon Nanotubes from Organic Chemistry Synthetic End-Cap Molecules. Nano Lett 2015;15:586-95.

[104] Yao Y, Feng C, Zhang J, Liu Z. "Cloning" of Single-Walled Carbon Nanotubes via Open-End Growth Mechanism. Nano Lett 2009;9:1673-7.

[105] Sanchez-Valencia J, Dienel T, Groning O, Shorubalko I, Mueller A, Jansen M et al. Controlled synthesis of single-chirality carbon nanotubes. Nature 2014;512:61-4.

[106] Rao F, Li T, Wang Y. Growth of "all-carbon" single-walled carbon nanotubes from diamonds and fullerenes. Carbon 2009;47:3580-4.

[107] Finnie P, Homma Y, Lefebvre J. Band-Gap Shift Transition in the Photoluminescence of Single-Walled Carbon Nanotubes. Phys Rev Lett 2005;94:247401.

[108] Lefebvre J, Finnie P. Photoluminescence and Förster Resonance Energy Transfer in Elemental Bundles of Single-Walled Carbon Nanotubes. J Phys Chem C 2009;113:7536-40.

[109] Lefebvre J, Finnie P. Polarized Photoluminescence Excitation Spectroscopy of Single-Walled Carbon Nanotubes. Phys Rev Lett 2007;98:167406.

[110] Lefebvre J, Austing DG, Bond J, Finnie P. Photoluminescence Imaging of Suspended Single-Walled Carbon Nanotubes. Nano Lett 2006;6:1603-8.

[111] Liu K, Deslippe J, Xiao F, Capaz RB, Hong X, Aloni S et al. An atlas of carbon nanotube optical transitions. Nat Nano 2012;7:325-9.

[112] Kim M, Kang J, Park M. Chirality-controlled growth of single-walled carbon nanotubes via nanotube cloning. Macromolecular Research 2014;22:917-25.